

Copyright

by

David Andrew Holmes McCleary

2012

**The Thesis Committee for David Andrew Holmes McCleary
Certifies that this is the approved version of the following thesis:**

**Three Dimensional Computational Modeling of Electrochemical
Performance and Heat Generation in Spirally and Prismatically Wound
Configurations**

**APPROVED BY
SUPERVISING COMMITTEE:**

Supervisor:

Jeremy Meyers

Ofodike Ezekoye

**Three Dimensional Computational Modeling of Electrochemical
Performance and Heat Generation in Spirally and Prismatically Wound
Configurations**

by

David Andrew Holmes McCleary, B.S.M.E.

Thesis

Presented to the Faculty of the Graduate School of

The University of Texas at Austin

in Partial Fulfillment

of the Requirements

for the Degree of

Master of Science in Engineering

The University of Texas at Austin

August 2012

Acknowledgements

I would first like to thank my advisor, Dr. Jeremy Meyers, for the opportunity to work on this project. I learned a great deal about electrochemistry and batteries in particular, which was my reason for attending UT.

I would also like to thank Dr. Beomkeun Kim, a visiting professor from South Korea, for providing supplemental guidance over the past eight months. His understanding of modeling helped “connect the dots” between electrochemical and thermal concepts, which saved a great deal of time. Also his experienced approach towards this research helped me produce a thesis that I am proud of.

Lastly, I would like to thank A123 Systems for the opportunity to explore their technology. Also thank you to the University of Texas at Austin College of Engineering, the Booker family, and George J. Heuer, Jr. for the fellowships that provided funding to enable me to accomplish my goals.

Abstract

Three Dimensional Computational Modeling of Electrochemical Performance and Heat Generation in Spirally and Prismatically Wound Configurations

David Andrew Holmes McCleary, M.S.E.

The University of Texas at Austin, 2012

Supervisor: Jeremy Meyers

This thesis details a three dimensional model for simulating the operation of two particular configurations of a lithium iron phosphate (LiFePO_4) battery. Large-scale lithium iron phosphate batteries are becoming increasingly important in a world that demands portable energy that is high in both power and energy density, particularly for hybrid and electric vehicles. Understanding how batteries of this type operate is important for the design, optimization, and control of their performance, safety and durability. While 1D approximations may be sufficient for small scale or single cell batteries, these approximations are limited when scaled up to larger batteries, where significant three dimensional gradients might develop including lithium ion concentration, temperature, current density and voltage gradients. This model is able to account for all of these gradients in three dimensions by coupling an electrochemical model with a thermal model. This coupling shows how electrochemical performance affects temperature distribution and to a lesser extent how temperature affects electrochemical performance. This model is applicable to two battery configurations — spirally wound and prismatically wound. Results generated include temperature influences on current distribution and vice versa, an exploration of various cooling environments' effects on performance, design optimization of current collector thickness and current collector tab placement, and an analysis of lithium plating risk.

Table of Contents

CHAPTER 1: BACKGROUND.....	1
1.1 Introduction.....	1
1.2 Battery Structure.....	2
1.2.1 Single Electrochemical Cell.....	2
1.2.2 Electrochemical Cells within a Real Battery.....	3
1.2.3 Spirally Wound and Prismatically Wound Batteries.....	4
1.2.4 Specific Materials.....	6
1.3 Prior 3D Modeling of Batteries.....	6
CHAPTER 2: MATHEMATICAL MODEL OF WOUND BATTERY	
CONFIGURATIONS.....	10
2.1 Modeling the Battery as a 3D Network of Resistors.....	10
2.1.1 Current Collector and Electrochemical Reaction Resistors.....	10
2.1.2 Alignment of Nodes in Wound Configurations.....	14
2.1.3 Archimedes' Spiral Theory and Application.....	15
2.1.4 Prismatically Wound Battery as Concentric Layers.....	19
2.2 Models.....	19
2.2.1 Electrochemical Model.....	20
2.2.2 Thermal Model and Coupling with Electrochemical Model.....	21
2.3 Numerical Methods.....	22
2.3.1 Finite Difference Method.....	22
2.3.2 Solution Phase Concentration Control Volume Method.....	23
2.3.3 Solid Phase Duhamel's Superposition Integral.....	24
2.3.4 Newton Raphson Method.....	24

CHAPTER 3: NUMERICAL RESULTS	27
3.1 Design Optimization	27
3.1.1 Single Tab versus Multiple Tab Comparison	27
3.1.1.1 Spiral Configuration - Tabs	28
3.1.1.2 Prismatically Wound Configuration - Tabs	33
3.1.2 Cooling Method Comparison.....	39
3.1.2.1 Spiral Configuration - Cooling Method.....	39
3.1.2.2 Prismatically Wound Configuration - Cooling Method.....	44
3.1.3 Current Collector Thickness Comparison.....	48
3.1.3.1 Spiral Configuration - Collector Thickness	48
3.1.3.2 Prismatically Wound Configuration - Collector Thickness.....	52
3.1.4 Lithium Plating	57
3.1.4.1 Spiral Configuration - Li Plating	57
3.1.4.2 Prismatically Wound Configuration - Li Plating	63
3.2 Configuration Comparison.....	67
3.2.1 Voltage versus Capacity Comparison.....	67
3.2.2 Energy Density Comparison.....	68
3.2.3 Temperature and Current Density Distribution Comparison.....	72
3.3 Model Limitations.....	76
Appendix A Model Input Data	77
Appendix B Electrochemical and Thermal Model Theory.....	85
Appendix C Discretization Error Check	91
References.....	95
Vita	98

CHAPTER 1: BACKGROUND

1.1 Introduction

Over the past two decades lithium ion batteries have revolutionized the tech industry. Through high power and energy densities, lithium ion batteries have become the primary battery chemistry for cellular phones and portable laptops. As the auto industry evolves it will rely more heavily upon batteries for hybrid and pure electric applications. Lithium ion batteries are a likely candidate to change how vehicles are powered.

Unlike small-scale batteries for personal devices, which only need to last for a few years, large-scale lithium ion batteries for vehicles will ultimately need to last for the life of the car, around 100,000 miles or 10 years. Therefore, durability, performance and safety are critical characteristics of the batteries placed in these vehicles. Temperature and risk of lithium plating are related directly to safety, while design factors such as current extraction tab locations and current collector thickness are key to performance; all are coupled to one another and affect durability.

Several factors are explored in this study. Non-uniform temperature across a battery cell can cause the materials to break down quicker and potentially lead to thermal runaway. Whenever the potential of the electrolyte exceeds that of the adjacent negative electrode during a charging event, there is potential for lithium to plate out onto the electrode. Once this occurs it is probable that dendrites will form, and unless the plating is stopped they will grow and pierce the membrane to cause a short circuit, permanently damaging the cell. Tab size and location dictates current flow through a cell and can cause non-uniformities of current density and consequently temperature. As current collector thickness is increased, it will improve current density uniformity but sacrifice specific energy density. Side reactions may also occur in the battery when in a highly charged state. All of these factors must be considered to reach the objectives of large scale lithium ion batteries.

In this thesis various design parameters and operating procedures are explored for two different configurations of a lithium iron phosphate battery. For two configurations, temperature, current density and gradients, as well as ionic concentration across the cell

will be monitored and analyzed. For this thesis, a computational model that predicts the performance of the battery in three dimensions was developed. The model is used to make recommendations for design optimization and operation.

1.2 Battery Structure

Electrochemical energy storage devices are commonly referred to as batteries. These devices store energy chemically. When connected to an external circuit the chemical energy is converted into useful electrical energy. To accomplish this, the battery must have five different layers: the negative current collector, negative electrode, separator, positive electrode, and positive current collector.

1.2.1 SINGLE ELECTROCHEMICAL CELL

In a single electrochemical cell, lithium ions (Li^+) are shuttled from one electrode to the other through the separator; the direction the ions flow depends on whether the battery is charging or discharging. No matter which direction a lithium ion travels, when it leaves one electrode the electron that was paired with it travels through an external circuit and meets up with the lithium ion on the other electrode. When attempting to draw electricity from a battery, the negative electrode is called the anode and the positive electrode is the cathode. See Figure 1 for a basic diagram of a battery being discharged.

Each electrode is a porous material that conducts electricity, and filling the pores is an electrolyte that is able to conduct lithium ions well, as depicted in Figure 2. The electrochemical reaction, where Li^+ and the electron separate, occurs at the electrode-electrolyte interface. Upon reaction, the electrons flow through the electrode to the current collector and on to the external circuit, while the lithium ions travel through the electrolyte and separator to the opposite electrode where they will be met by electrons at that electrode's interface with the electrolyte. Meanwhile the electrons have gone through an external circuit and produced work.

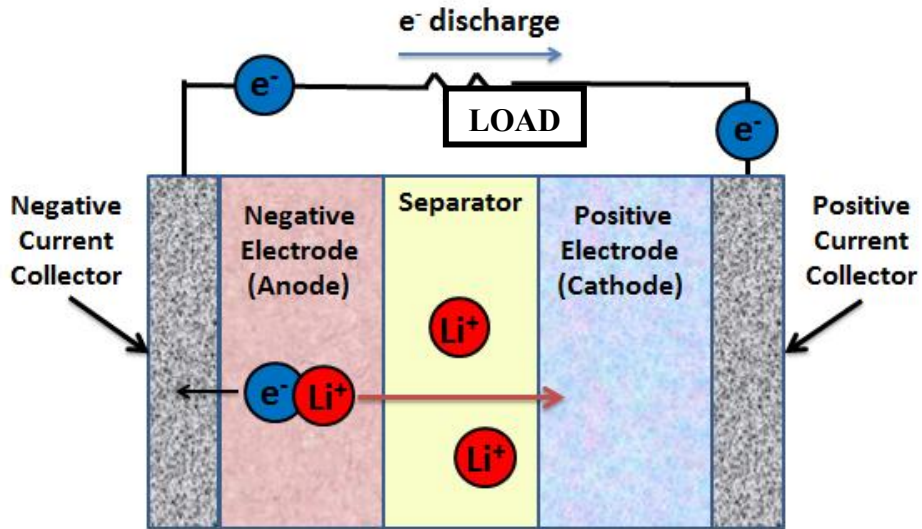


Figure 1: Diagram of a lithium-ion battery being discharged.

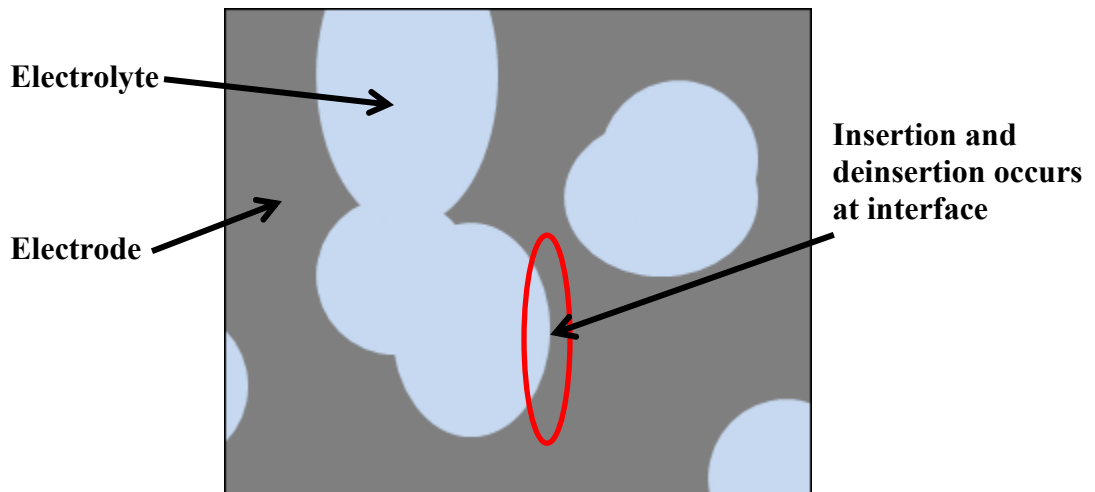


Figure 2: Representation of a porous electrode under microscope. The electrochemical reaction occurs at the electrolyte – electrode interface.

1.2.2 ELECTROCHEMICAL CELLS WITHIN A REAL BATTERY

In theory, an electrochemical cell is simply 5 layers of material, but to have a device that can provide useful power for a reasonable amount of time, more than one electrochemical cell is needed. Typically, multiple cells are connected in parallel within a single battery. To minimize materials and simplify manufacturing, each current collector will have an electrode on either side of it (Figure 3).

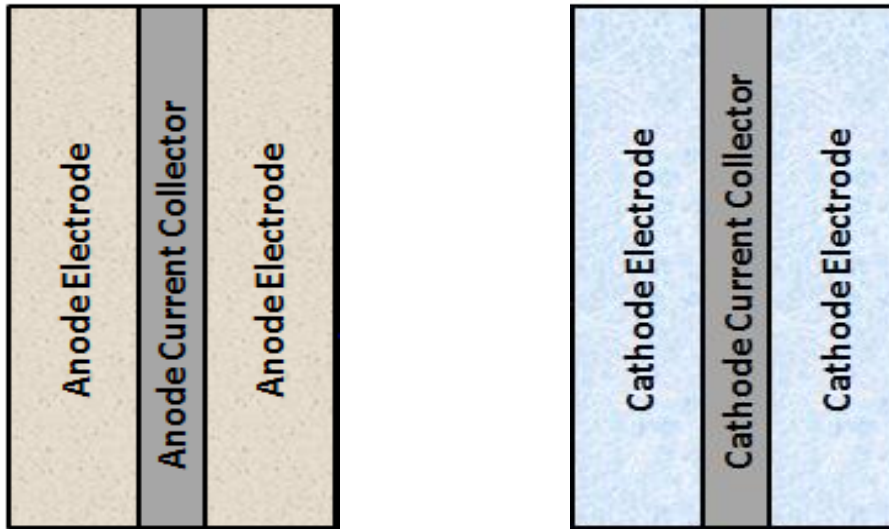


Figure 3: Each current collector has two electrodes.

Therefore, for a given location within a current collector, current is flowing into (or out of) it from two different directions. Figure 4 shows four layers of current collectors (three electrochemical cells) as they would appear in a commercial battery during discharge.

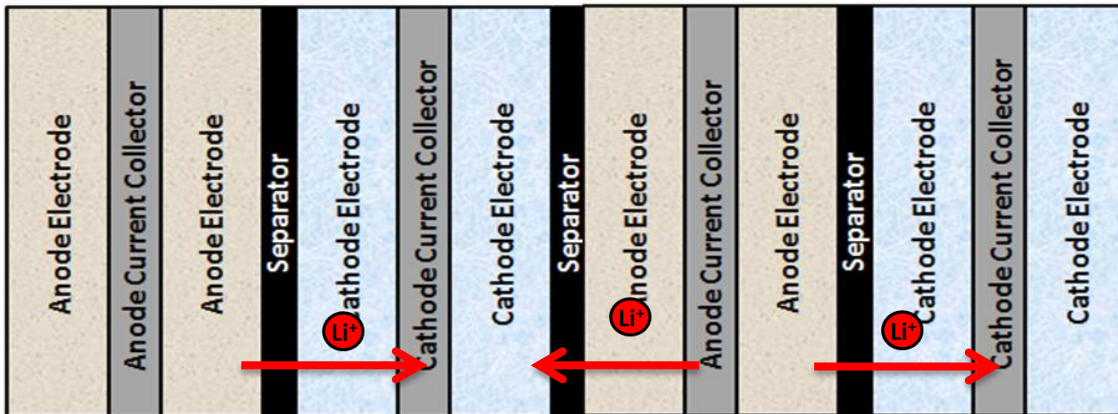


Figure 4: Layers of electrochemical cells as they would appear in a commercial battery.

1.2.3 SPIRALLY WOUND AND PRISMATICALLY WOUND GEOMETRIES

There are various lithium-ion geometries that exist, common ones being planar, spirally wound, and prismatically wound batteries. As will be explained in the following section, planar batteries have been explored extensively; therefore this thesis focuses on spirally wound and prismatically wound batteries.

Planar cells can be geometrically simplified to look like sheets of paper stacked upon one another, where each sheet can be viewed as a single electrochemical cell. Spirally wound (or cylindrical) batteries consist of only one negative current collector, one positive current collector, and other components that are all wrapped around a center post. Prismatically wound batteries are a hybrid of planar and spirally wound batteries; this battery configuration is wound around a rectangular center “post” and has both flat and rounded portions. For both spirally wound and prismatically wound batteries, the inner-most winding and outer-most winding are commonly the negative electrodes (anodes). Drawings of the spirally wound and prismatically wound battery can be found in Figure 5.

Planar cells offer the best use of volumetric space but they are time consuming and costly to assemble. Spirally wound batteries are easier to assemble and therefore less costly than planar cells, but there is unused space when placing multiple spirally wound batteries next to one another. A prismatically wound battery can be manufactured with similar ease as the spirally wound battery but utilizes volumetric space better.

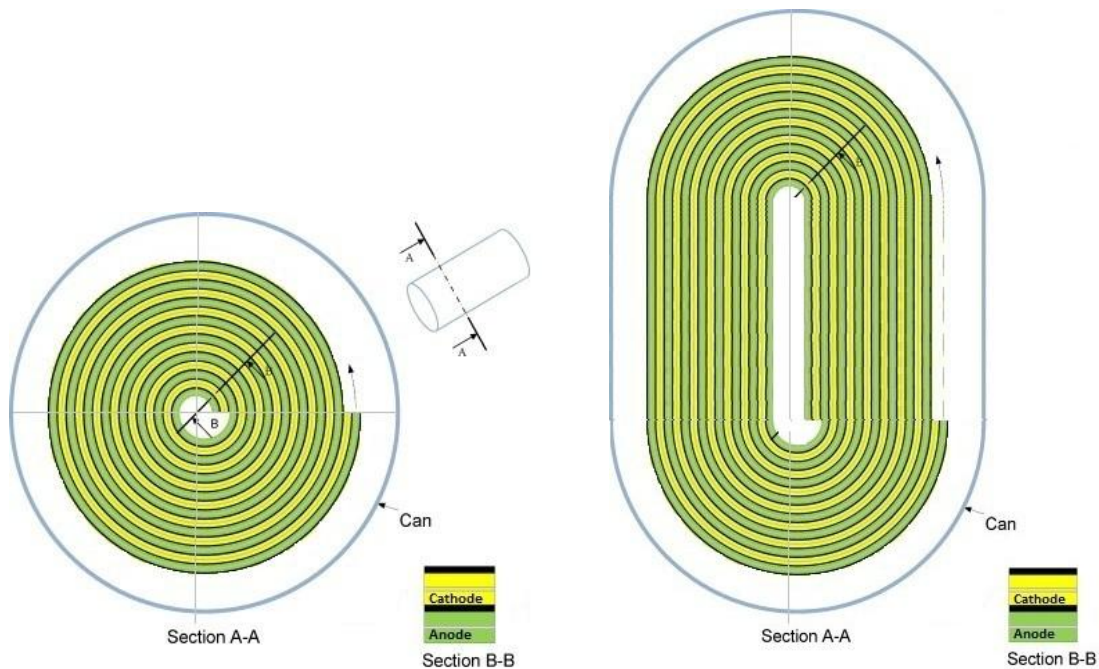


Figure 5: Top views of spirally wound (left) and prismatically wound (right) batteries [1].

1.2.4 SPECIFIC MATERIALS

Though other anode materials are being explored currently, graphite (C_6) is commonly used as the negative electrode and is the negative electrode explored in this thesis. Upon insertion of Li^+ into the graphite, the chemical composition is written as Li_xC_6 .

In recent years there have been many breakthroughs on positive electrode materials. The discovery of layered oxide electrodes by UT's Dr. John Goodenough enabled the first widespread use of lithium ion batteries in portable applications worldwide, with Li_xCoO_2 being the most common electrode material used. Spinel materials such as $LiMn_2O_4$ have been commercialized as well, but recently the olivine structure has garnered interest. More specifically the olivine structure $LiFePO_4$ (lithium iron phosphate) has received attention because it is less expensive than most other electrodes and also allows quicker charging/discharging. It is the positive electrode of a $LiC_6/LiPF_6/LiFePO_4$ cell that is studied in this thesis.

1.3 Prior 3D Modeling of Batteries

Prior work has explored various battery chemistries and geometries and what current and temperature distributions may look like under different conditions. Early models focused on only the electrochemical behavior of lithium insertion batteries utilizing a methodology that was the basis for the electrochemical model used in this thesis [2][3][4]. Bernardi et al in 1993 modeled the electrochemical reaction of a 2D lead acid battery isothermally and determined that higher current density will occur at the tabs of the battery [5].

Soon after, thermal modeling of lithium insertion batteries was conducted by Lee et al who conducted 3D thermal modeling for large scale electric vehicle batteries, and by Evans and White who studied 3D heat generation in spirally wound batteries. In both cases, local variation of heat generation was determined in 3D, but they required pre-determined inputs for local current density and local potential [6][7]. Verbrugge used a 3D thermal and electrochemical model for a lithium metal vanadium oxide battery that was accurate under low power conditions. The model was limited because it ignored

lithium ion concentration gradients and the current-voltage relationship in the electrochemical model was treated as being linear [8]. In another study, Baker and Verbrugge created a perturbation analysis for temperature and current distribution in thin film batteries but it was only valid for short times [9].

In two studies that utilized finite-element analysis, resistance was specified for each element in the model and then current distribution and resistive heating were calculated [10][11]. Bharathan et al treated resistance as constant throughout [10], while Inui et al allowed resistance to be variable. In Inui's study of both prismatic and spirally wound configurations, state of charge and temperature values were derived from experimental data, and the electrochemical reaction was treated as homogeneous whereas the thermal model was treated as anisotropic [11].

There is a multitude of electrochemical and thermal models involving the spirally wound battery configuration. Reimers treated battery impedance as constant in time and space and solved for current distribution using current collector resistance and electrochemical cell impedance values; the battery was modeled as if it were unwound [12]. Harb and LaFollette used porous electrode theory to create a 1D electrochemical model which was paired with a 2D network of resistors to represent the current collectors; their study predicted the current distribution within a lead acid battery [13]. In another study, Harb modeled lithium ion batteries [14], but the methodology in both studies was different than what is utilized in this thesis. In Harb's studies, the overall current or voltage at the tabs was chosen using an educated guess, and the network of nodes was solved to see if the sum of local current densities (or voltages) equaled the guessed value; if it was not equal then a new guess was generated [13][14]. In a study by Heon et al, the effects of current distribution on the temperature field were investigated in 3D, but potential drop across the length of the cell was neglected [15].

Jeon and Baek provided a thermal analysis of cylindrical lithium cobalt oxide and lithium nickel cobalt manganese batteries during discharge cycles. They used a finite-element method to determine battery temperatures at various discharge rates but did not investigate the effects of temperature on local current distribution. Also, the study

neglects the existence of tabs [16]. Zhang explored the local thermal properties of a lithium manganese spinel cylindrical battery during discharge cycles and how they relate to Li^+ concentration across the cell. To determine node spacing, a derivation of Archimedes' Spiral Equations was utilized. The study did not look into local current densities or the effect of tab placement or current collector thickness [17].

There are far fewer studies conducted on prismatic wound batteries. Chen et al explored the potential for thermal runaway due to overcharge in a prismatically wound lithium cobalt oxide battery, but it was mostly experimental and did not attempt to map the temperature or current distribution throughout the cell [18]. Cousseau et al had a similar experimental exploration of the benefits using a prismatic wound "jellyroll" configuration. Similar to Chen et al, there was little modeling present and no attempt to determine localized current and temperature values [19].

Several models demonstrated the importance of coupling good electrochemical model and thermal models to predict battery performance [20][21][22]. Gerver et al showed that this coupling is useful in understanding battery safety, optimizing cooling design and optimization of tab placement and current collector thickness for a prismatic lithium iron phosphate battery. It explored high power, large scale batteries that can be utilized in portable applications such as in a hybrid vehicle. As in this thesis, Gerver utilized a 2D network of resistors paired with a non-linear 1D electrochemical model that simulated the transient response of a single cell prismatic configuration during charge and discharge [22]. Gerver's approach to planar lithium ion batteries is the foundation for the treatment this thesis takes towards two other battery configurations of the same chemistry.

This thesis has a 2D network of resistors to model heat generation and current flow through the current collectors and a 1D non-linear model that represents the electrochemical reaction occurring in two different configurations of lithium iron phosphate battery – spirally wound and prismatically wound. The purpose is to show how temperature and current distribution affect one another in various thermal environments, tab locations, current collector thicknesses, and C-rates for use in optimizing this

particular battery chemistry for use in large scale portable applications such as in an electric vehicle.

CHAPTER 2: MATHEMATICAL MODEL OF WOUND BATTERY CONFIGURATIONS

2.1 Modeling the Battery as a 3D Network of Resistors:

When operating a battery, only the total current or total voltage across the terminals is known. Consequently, current density and voltage values for each cell and for any specific location within that cell are unknown. Locations in which current density or potential differences are larger in magnitude than the rest of the cell can potentially fail sooner than the rest of the cell, thereby damaging the entire cell. When trying to optimize a battery's performance and durability, it is ideal to have uniform current density and voltage across each cell; as such, it is necessary to develop a model to determine the local values. Then one is able to alter properties during cell design to obtain optimal results.

If one wanted to model each location within an electrochemical cell in three dimensions and then solve for the system of locations, it would be prohibitively time- and computer- intensive. Instead, by modeling each current collector as a two-dimensional network of foils connected by resistors, coupled with one dimensional electrochemical model, the local current and voltage values can be determined accurately and in a reasonable amount of time. The following treatment follows directly from the work of Rachel Gerver's master's thesis, which developed this solution technique for a planar cell arrangement. The interested reader should visit her thesis for the full description; Section 2.11 provides an overview of the development to provide context for the current work.

It should be noted that many of the methods used in the following sections are based on the work Gerver et al implemented for planar lithium iron phosphate batteries, which in turn is based on the work developed by Doyle, Fuller, and Newman. Both sources serve as the basis for which the following wound battery models were developed in the Sections 2.11, 2.2, 2.2.1, 2.2.2, 2.3, 2.3.1, 2.3.2, 2.3.3, 2.3.4, and all three Appendices.

2.1.1 CURRENT COLLECTOR AND ELECTROCHEMICAL REACTION RESISTORS

Depending on desired model accuracy, the user determines the number of nodes in two directions, x and y, within each current collector. The current collector is then

modeled as an array of foils (also referred to as nodes) connected by resistors (see Figure 6). To illustrate the concept clearly, the current collectors for the spirally and prismatically wound batteries are shown as planar collectors, as if the layers of the battery have been unrolled and laid flat.

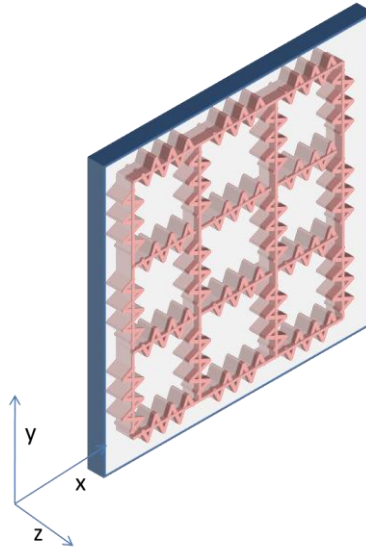


Figure 6: Representation of the 2D network of nodes and resistors in a current collector. Illustration provided by Gerver [22].

Resistors are perpendicular to one another and resistance values vary with temperature across each cell. The current collectors are allowed to be defined this way because heat generated from resistance within the current collector is a factor of magnitude less than the heat generated from each electrochemical reaction. Modeling the current collectors as an array of nodes connected by resistors is a simplification that sacrifices little accuracy.

In the z -direction is the electrochemical reaction that exists between adjoining anode and cathode nodes (see Figure 7). As described in Section 2.1.2, in a wound configuration it is important to keep track of which anode nodes line up with which cathode nodes. Each electrochemical reaction is represented by a one dimensional electrochemical model, represented as a non-linear resistor. This is described in further detail in Section 2.2.

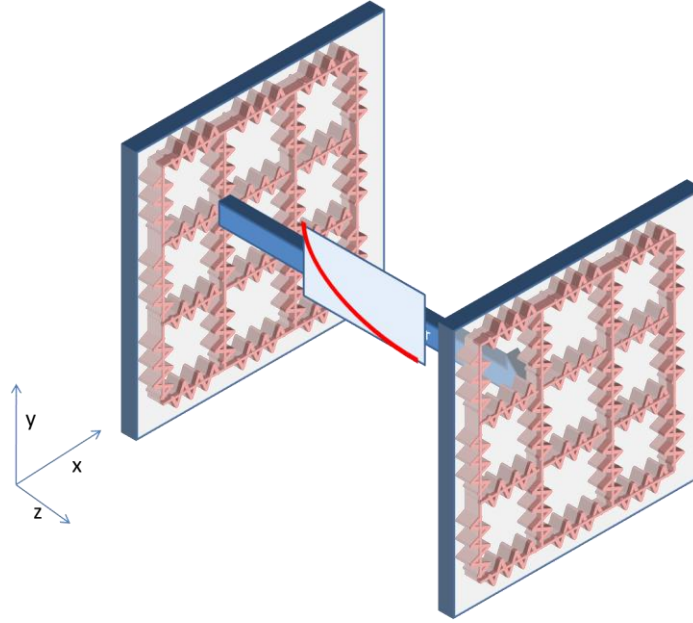


Figure 7: Adjoining anode and cathode current collectors with a non-linear resistor representing the electrochemical reaction between corresponding nodes [22].

Modeling the current collector and electrochemical reaction in this manner allows us to conduct a current balance for each node (Equation 2.1). At each node the current balance will equal zero by rules of conservation of current (Figure 8).

$$I_{y-1} + I_{x-1} = I_{y+1} + I_{x+1} + I_{electrochemical, x,y} \quad [2.1]$$

where

$$I_{y-1} = \frac{V_{y-1} - V_{x,y}}{Resistance} \quad I_{x-1} = \frac{V_{x-1} - V_{x,y}}{Resistance} \quad I_{x+1} = \frac{V_{x,y} - V_{x+1}}{Resistance} \quad I_{y+1} = \frac{V_{x,y} - V_{y+1}}{Resistance} \quad [2.2]$$

where

$$Resistance = \frac{1}{Conductivity}$$

and

$$I_{electrochemical, x,y} = A(V_{x,y anode} - V_{x,y cathode})^3 + B(V_{x,y anode} - V_{x,y cathode})^2 + C(V_{x,y anode} - V_{x,y cathode})^1 + D \quad [2.3]$$

A , B , C , and D are all cubic fit coefficients.

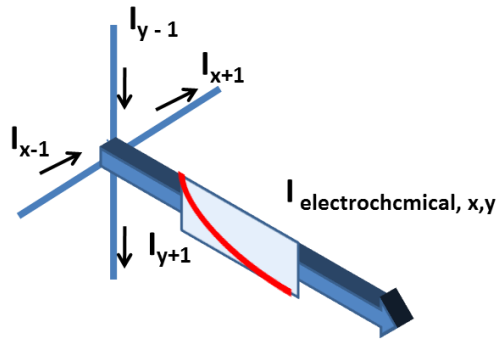


Figure 8: Current balance at a single at node location (x, y) [22].

By modeling the current collector as an array of nodes connected by resistors and the electrochemical reactions as non-linear resistors, one is able to solve for current density and voltage at any location within the cell. See Figure 9 for a depiction of a unit cell (anode – cathode – anode) modeled this way.

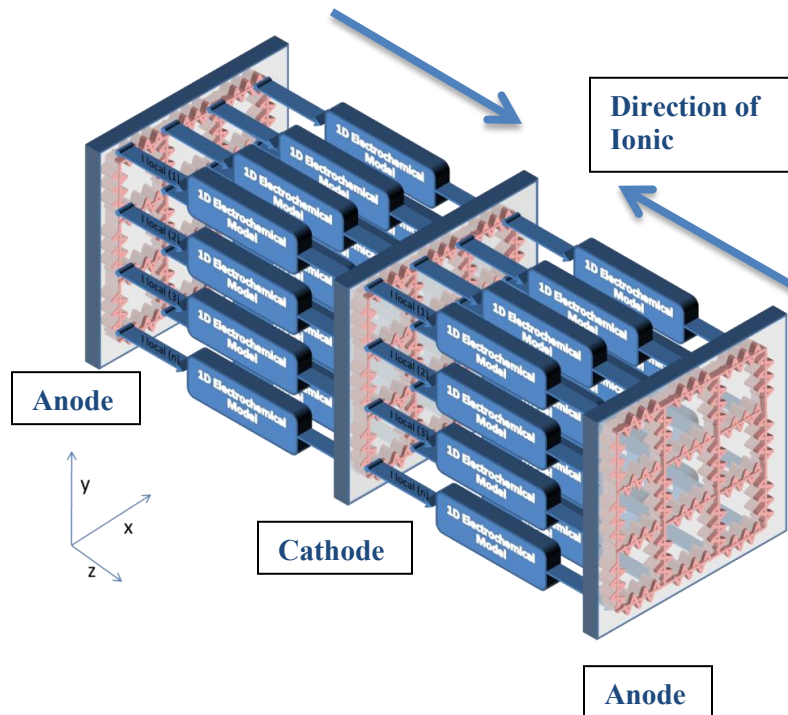


Figure 9: 3D network of resistors for a unit cell in the wound configuration. The center current collector is a cathode and outer current collectors are anodes. Illustration altered from [22].

2.1.2 ALIGNMENT OF NODES IN WOUND CONFIGURATIONS

Thus far, each of the previous four figures displayed a simplified view of the 3D network of resistors; this is how they would appear in a planar cell. In a battery that is wound, there is a slight difference in alignment of nodes due to the curvature and winding of the components.

First, the user can choose the number of nodes per winding for a given battery. The nodes will be a consistent radial angle distance from one another. For example if one wants four nodes per winding in a spirally wound battery, each node for each layer will be $\pi/2$ radians away from one another. Consequently, for each successive layer the distance between each node within the current collector will increase. For a top view of the spirally wound battery configuration and how nodes line up, see Figure 10.

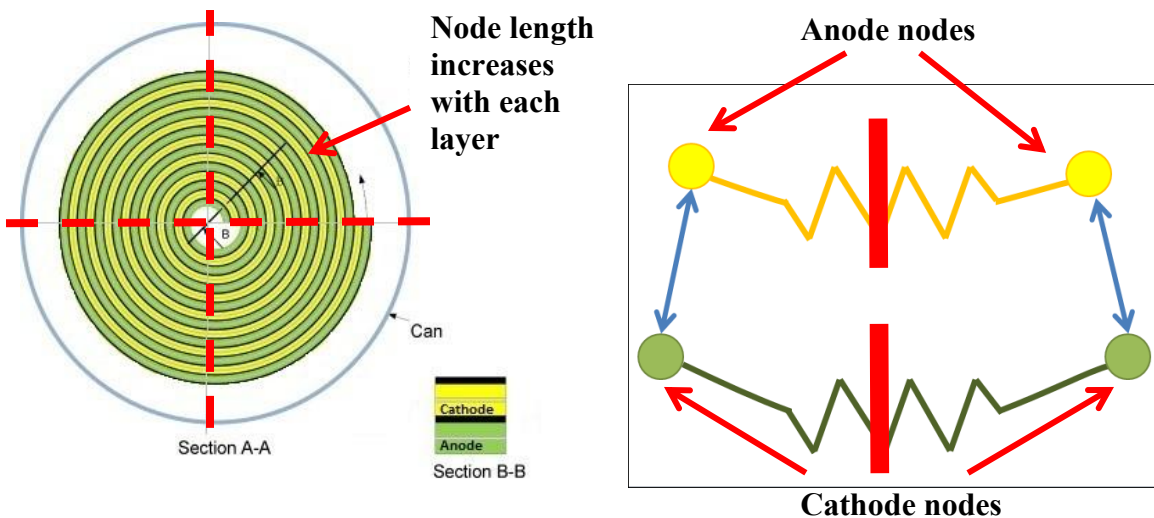


Figure 10: On the left, a spirally wound battery that has four nodes per winding. Illustration courtesy of [1]. On the right, it shows how the 3D resistor network looks from above between two nodes. The dark green resistor runs within the anode current collector, dark yellow through the cathode current collector, and the light blue double arrow is the electrochemical reaction resistor between each electrode. The red dash designates where the windings are divided into nodes.

For a prismatically wound battery, one needs to choose the number of nodes per turn and the number of nodes per plane. For example, if one wants to have two nodes per turn and two nodes per plane it will total eight nodes per winding; see Figure 11 for a diagram of how it would look from a top view. Notice that each node in the planar

section of the battery has the same length, whereas the nodes in the turns increase in distance with each successive layer.

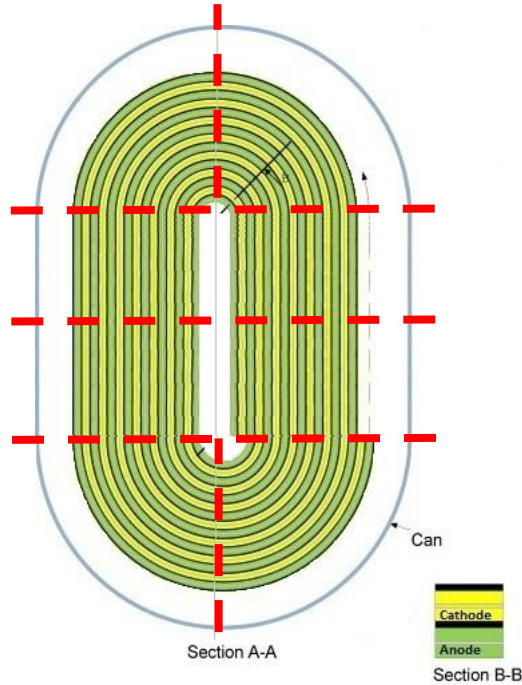


Figure 11: Top view of a prismatically wound battery divided into two nodes per plane and two nodes per turn (total of eight nodes per winding) [1].

While modeling these two configurations, the length of each node and distance between each node is calculated to determine resistance values between each node in the direction of the current collector. Note, the distance between each node is measured from the center point of each node to the center point of an adjacent node. Also it is necessary to keep track of which anode nodes are reacting with which cathode nodes in order to properly model the battery as a 3D network or resistors.

2.1.3 ARCHIMEDES' SPIRAL THEORY AND APPLICATION

As detailed in section 1.2.3, the spirally wound battery consists of a continuous electrochemical cell that is wrapped upon itself. A spiral is defined as a continuous curve originating at an origin that gets progressively farther away from that origin with each revolution [23]. An Archimedes Spiral is unique, in that each successive winding is a

constant distance δ from the previous winding. The spiral is named after the Greek mathematician, Archimedes, who discussed this type of spiral in his 225BC publication titled *On Spirals* [25].

Upon closer inspection, one will notice from top view that each layer of the spirally wound battery can simply be viewed as its own Archimedes' Spiral.

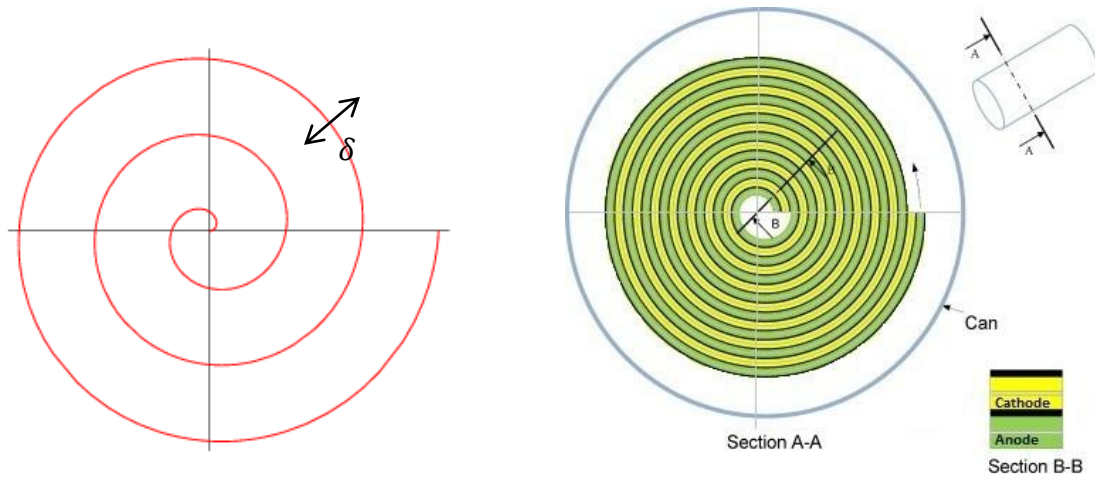


Figure 12: Left, Archimedes' Spiral. Right, top view of spirally wound battery [1].

The equations for arc length associated with an Archimedes' Spiral are used in this model to determine each node's length and also the distance between each node. The length of each node refers to the length along the spiral (red line in the left illustration of Figure 12) from one black sectioning line to the next, while the distance between each node refers to the distance from the center point of one node to an adjacent node. Archimedes' Spiral has two key equations, the first being the polar equation:

$$r = B\theta \quad [2.4]$$

where r is the radius from the origin, θ is the polar angle to a point on the spiral of interest, and B is related to the constant separation distance between successive windings [24]. Specifically B is related to the spirally wound battery by:

$$t = 2\pi B \quad [2.5]$$

where t is the thickness of a unit electrochemical cell:

$$t = A_{cc} + 2 * A + 2 * S + 2 * C + C_{cc} \quad [2.6]$$

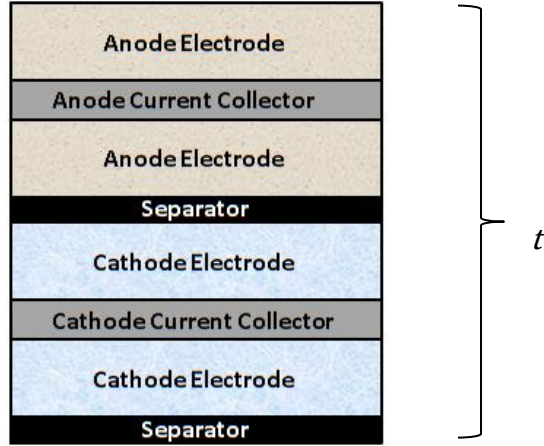


Figure 13: Unit electrochemical cell.

The second Archimedes' Spiral Equation of interest produces the arc length S from the origin along the length of the spiral to the point of interest k with polar coordinates of (r_k, Θ_k) [24].

$$S(\Theta_k) = \frac{1}{2}B \left[\theta_k \sqrt{1 + \theta_k^2} + \ln(\theta_k + \sqrt{1 + \theta_k^2}) \right] \quad [2.7]$$

Since there are two electrodes about which we desire distance information, Archimedes' Spiral Equations must be applied to each electrode's current collector separately. Note that the distance from anode current collector to anode current collector on successive winding layers is the same as that from one cathode current collector to successive cathode current collector; this distance is t .

For each current collector there are several distances in the x-direction that need to be calculated and recorded for each node: the length L from where the current collector begins (at the center post) to the node of interest, the length of that node ndx , and the distance from that node to the adjacent nodes $ndxm1$ or $ndxp1$. Once L is calculated, the other distances are easily calculated. L is simply the node's Archimedes' Spiral arc length $S(\theta_k)$ subtracted by the arc length $S(\theta_{cp})$ of the spiral that does not physically exist because the center post is in its place.

$$L(k) = S(\theta_k) - S(\theta_{cp}) \quad [2.8]$$

where

$$\theta_{cp} = 2\pi r_{cp}/t$$

$$\text{Anode: } r_{cp} = r_c + A$$

$$\text{Cathode: } r_{cp} = r_c + 2 * A + A_{cc} + S + C$$

Since we want to find the Archimedes' Spiral arc length to the *center* of a particular node, we must subtract ½ of a nodal rotation to determine θ_k .

$$\text{Anode: } \theta_k = (2\pi/npw) * [k - (ny - 1) * nx_{anode}] - \pi/npw$$

$$\text{Cathode: } \theta_k = (2\pi/npw) * [k - npa - (ny - 1) * nx_{cathode}] - \pi/npw \quad [2.9]$$

Once $L(k)$ is obtained, each node's length and distance between adjacent nodes is calculated:

$$ndxm1 = L(k) - L(k - 1)$$

$$ndxp1 = L(k + 1) - L(k)$$

$$ndx = (ndxm1 + ndxp1)/2 \quad [2.10]$$

With these distances, one can easily calculate the area per node and volume per node. All values are useful in calculating conductivity, current density, and heat generation.

List of Symbols

A_{cc}	Anode current collector thickness
C_{cc}	Cathode current collector thickness
A	Anode electrode thickness
C	Cathode electrode thickness
S	Separator thickness
t	Unit electrochemical cell thickness
k	Cell node
npw	Nodes per winding
ny	Position in the y direction
nx_{anode}	Position in the x direction on the anode
$nx_{cathode}$	Position in the x direction on the cathode

2.1.4 PRISMATICALLY WOUND BATTERY AS CONCENTRIC LAYERS

While the size of each node in the spirally wound configuration can easily be modeled using Archimedes' Spiral Equations, the prismatically wound configuration does not have a similar theory to employ for model construction. Though the layers of the prismatically wound configuration are continuous in reality (Figure 14, left), for this thesis they are modeled as concentric layers (Figure 14, right). By making this simplification, there is only a slight sacrifice in accuracy of node area, where each layer starts and ends. This only affects conductivity terms within the model. The minor amount of error created through this simplification has been assumed to be negligible to the overall model and the results it produces.

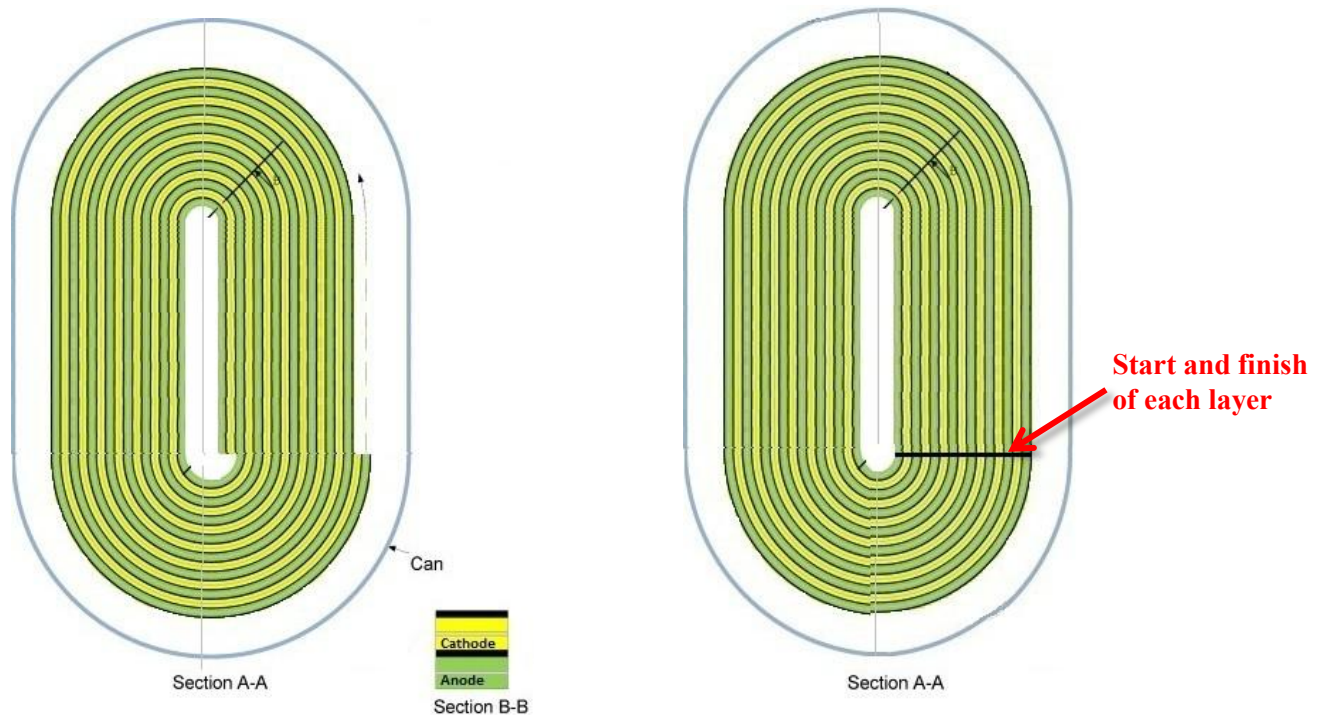


Figure 14: Pictured on the left is the actual manner in which a prismatically wound battery is layered. On the right is the way each layer is modeled in this thesis [1].

2.2 Models

In this thesis, the overall model is a collection of submodels and methods that work with one another to generate useful system level results. The electrochemical model

is coupled with a thermal model and solved using numerical methods. Sections 2.2.1 and 2.2.2 detail each model and their coupling in greater detail.

2.2.1 ELECTROCHEMICAL MODEL

For each anode-cathode node pairing within a cell, the current-voltage profile is needed in order to have a functional model. Rather than sweeping through a range of voltages and currents for each node at every time step (which is both time consuming and computationally intensive), the goal is to create polynomial fit (cubic) current-voltage curves for each node that can be assumed for subsequent time steps. This is done by running each node at several different current densities over the same time step using initial conditions dictated by the user. This will provide the voltage across the cell (between anode and cathode) at each current density. Then, a cubic fit curve is applied to the results to obtain an equation that represents each node's electrochemical reaction. The equation, first mentioned in section 2.1.1, generates electrochemical current as a function of voltage (equation [2.3]).

When operating a battery, the current-voltage cubic curve will shift based upon the state of charge. With each successive time step, the curve will shift downward or upward by ΔI depending on if the battery is charging or discharging. The value for ΔI is approximated from user inputs and is constant throughout the simulation. For a given time step, the equation to generate $I_{electrochemical}$ at each node comes from the previous time step, with the only difference between time steps being that it has been shifted by ΔI . Next, these $I_{electrochemical}$ values are compared to a select few $I_{electrochemical}$ values that have been generated directly from the electrochemical model. If the comparison is within a preset tolerance, then the shift is accepted and that cubic curve is used. If not, then the sweeping process using the full electrochemical model (running each node at several current densities) is performed again for that time step.

The electrochemical model is based on porous electrode theory for lithium ion batteries developed by Doyle, Fuller and Newman. It is described in further detail in Appendix B. Simply stated, it makes use of six electrochemical theory equations to solve for six unknown variables. The unknown variables needed to generate the current-voltage

curve are potential in the solid (ϕ_1), potential in the solution (ϕ_2), current in the solid (i_2), rate of reaction (in), concentration of Li^+ in solution (c), and concentration of Li^+ at the electrode surface (cs). The six equations, derived and proven in electrochemical theory, are the Butler-Volmer equation, from concentrated solution theory, from porous electrode theory, a solid potential equation, a solution potential equation, and a solution current equation. The six unknowns in the six equations are solved numerically by the Newton Raphson method (described in Section 2.3.4). For each time step the thermal model is coupled with the electrochemical model to determine the impact of temperature on electrochemical performance and vice versa.

2.2.2 THERMAL MODEL AND COUPLING WITH ELECTROCHEMICAL MODEL

Under both charge and discharge, a battery will generate heat in two ways. One, there is irreversible heat generation due to cell resistance, both across the electrochemical cell and within the current collectors; it is associated with heat capacity, heat transfer and heat generation all in relation to the structure of the battery and the materials used. Two, there is reversible heat generation due to entropy of the electrochemical reaction itself, which can be exothermic or endothermic depending on whether the battery is charging or discharging; this is associated with ionization on one electrode, transfer of ions across the cell, and joining of ions with electrons at the opposite electrode. This thermal model accounts for both of these sources of heat.

This is described in further detail in Appendix B, but simply put heat generation due to cell resistance is calculated at each node and heat generation by the electrochemical reaction is calculated for each anode-cathode node pairing. Using these two heat generation values, temperature is then calculated for each node pairing. These temperature values for each node pairing are then used as inputs to the electrochemical model on the following time step.

This model assumes a quasi-steady state temperature for each time step. The model user decides the length of each time step, but the time steps selected to generate results for this thesis are one second long. This means that the temperature is considered constant, but it acknowledges that the electrochemical response is on a different time

scale than the thermal response. Also it is assumed in the electrochemical model that the input temperature is constant across the five layers of the cell (anode current collector, anode electrode, separator, cathode electrode, and cathode current collector).

2.3 Numerical Methods

As mentioned in 2.2.1, the six unknown electrochemical variables are solved for using six electrochemical reaction equations and the Newton-Raphson method. For this thesis, the Newton-Raphson method is also used in the thermal model and in the three dimensional current balance analysis, and the method is described in full detail in *Electrochemical Systems* [26].

Specifically, four of the electrochemical reaction equations are converted from partial differential equations to finite difference approximations (described in Section 2.3.1) before being solved using the Newton-Raphson method. The other two equations, which have to do with concentration of lithium in solution and solid, are handled in a different manner as detailed in Sections 2.3.2 and 2.3.3.

2.3.1 FINITE DIFFERENCE METHOD

The four partial differential equations are converted using the finite difference method. Examples are as follows:

$$\left. \frac{dc}{dx} \right|_{j-1/2} = \frac{c(j) - c(j-1)}{2h} + O(h^2) \quad [2.11]$$

$$\left. \frac{d^2c}{dx^2} \right|_j = \frac{c(j+1) + c(j-1) - 2c(j)}{h^2} + O(h^2) \quad [2.12]$$

Here c is the variable being solved, j is the mesh point, and h is the mesh spacing [22].

The Crank-Nicolson method is used for differential equations that are time dependent. This method is implicit and unconditionally stable with respect to time. An example is as follows:

$$\frac{\partial c}{\partial t} = D \frac{\partial^2 c}{\partial x^2} \quad [2.13]$$

$$\frac{c_j^{n+1}-c_j^n}{\Delta t} = \frac{1}{2} \left(D_j^{n+1} * \frac{c_{j+1}^{n+1}+c_{j-1}^{n+1}-2c_j^{n+1}}{h^2} + D_j^n * \frac{c_{j+1}^n+c_{j-1}^n-2c_j^n}{h^2} \right) \quad [2.14]$$

Here, n is the time step number, Δt is the time step size, D is a coefficient that can vary with time, and the other variables are as described for equations 2.11 and 2.12 [22].

2.3.2 SOLUTION PHASE CONCENTRATION CONTROL VOLUME METHOD

The solution phase concentration equation is solved using the control volume method as described in [22] and derived from [27].

$$\frac{\Delta c}{\Delta t} = \text{reaction rate} + \text{flux in} - \text{flux out} \quad [2.15]$$

The expression used for the control volume, shown in Figure 15, in this method is:

$$\begin{aligned} \varepsilon_{sep} * h_{sep} \left(\frac{3c_j^{t+1} + c_{j-1}^{t+1} - 3c_j^t + c_{j-1}^t}{4\Delta t} \right) + \varepsilon_{cath} * h_{cath} \left(\frac{3c_j^{t+1} + c_{j-1}^{t+1} - 3c_j^t + c_{j-1}^t}{4\Delta t} \right) \\ = \\ \left(N_{j-\frac{1}{2}}^{t+1} - N_{j+\frac{1}{2}}^{t+1} \right) + \left(N_{j-\frac{1}{2}}^t - N_{j+\frac{1}{2}}^t \right) + R_{j+\frac{1}{4}}^{t+1} + R_{j+\frac{1}{4}}^t \end{aligned} \quad [2.16]$$

where

$$R_{j+\frac{1}{4}} = \frac{a}{8} * (3i_{n,j} + i_{n,j+1}) * h_{cath} \quad [2.17]$$

$$N_{j+\frac{1}{2}} = \varepsilon_{cath} * D_{j+\frac{1}{2}} * \left(1 - \frac{d \ln c_o}{d \ln c} \right) * \left(\frac{c_{j+1} - c_j}{h_{cath}} \right) + \frac{t_{+,j+1/2}^0}{F} * \left(\frac{i_{2,j+1} + i_{2,j}}{2} \right) \quad [2.18]$$

Here t_{+}^0 is the cation transference number, ε_{cath} is porosity, N is flux of lithium ions, i_2 is current in solution, and the other variables are as described in section 2.3.1 and also as described in Gerber et al [22].

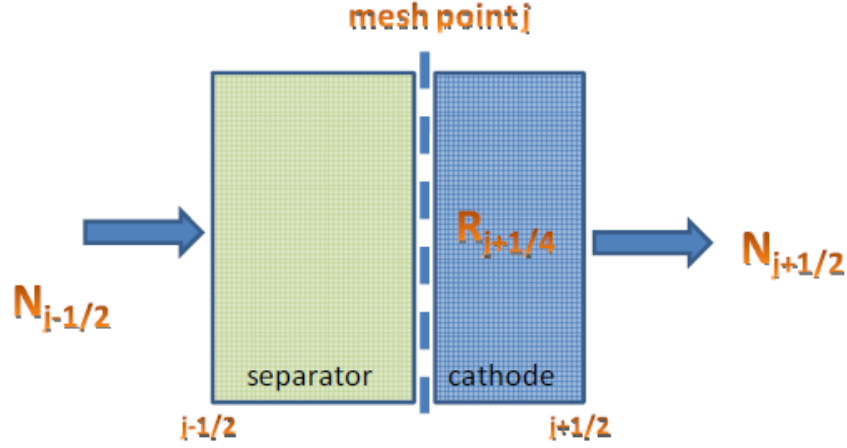


Figure 15: Control volume, courtesy of [22].

2.3.3 SOLID PHASE DUHAMEL'S SUPERPOSITION INTEGRAL

Duhamel's Superposition Integral approximation is used to derive the equation for solid phase concentration of lithium, described in [22] and fully explained in [28], which shows up in this thesis as follows:

$$\left. \frac{\delta c_s}{\delta r} \right|_{R, t_n} = \frac{c_{s,n} - c_{s,n-1}}{\Delta t} * A_1 + \sum_{j=0}^{n-2} \frac{c_{s,j+1} - c_{s,j}}{\Delta t} * A_{n-j} \quad [2.19]$$

where

$$A_n = \frac{a(t_n) - a(t_{n-1})}{D_s} * R \quad [2.20]$$

$$a(\tau) = \frac{2}{\pi^2} \sum_{n=1}^{\infty} \frac{1}{n^2} * [1 - \exp(-n^2 \pi^2 \tau)] \quad [2.21]$$

$$\tau = \frac{t D_s}{R} \quad [2.22]$$

Here, c_s is the lithium concentration at the surface of the solid, R is the electrode particle radius, D_s is the diffusion coefficient of lithium in the electrode, t is time, and n is the time step number [22].

2.3.4 NEWTON-RAPHSON METHOD

As mentioned before, after all electrochemical equations have been converted to non-linear equations via the methods mentioned in sections 2.3.1, 2.3.2, and 2.3.3, the

Newton-Raphson method is applied. It is also applied to the thermal model and the three dimensional current balance conducted at each node.

In this paragraph, a single unknown and single equation is explained to show the Newton-Raphson method at its simplest state. In this method, the term $g(c)$ is created to solve for c ; c will be an accurate solution when $g(c) = 0$. First, $g(c)$ is expanded as a Taylor series:

$$g(c) = g(c^0) + \left. \frac{dg}{dc} \right| (c - c^0) + \dots \quad [2.23]$$

For this method to converge and produce desired results, a good initial guess for c^0 is necessary. Neglecting higher order terms and setting $g(c) = 0$, equation 2.23 becomes:

$$c - c_0 = \Delta c = - \left. \frac{g(c_0)}{dg/dc} \right| \quad [2.24]$$

The new term, c , provides a more accurate approximation for the solution, and as one repeats this exercise it will converge to an accurate solution [26].

With several unknowns, a multidimensional Taylor series is used. The function of which we are seeking a solution will have more than one variable:

$$g_i(C_{k,j}, C_{k,n+1}, C_{k,n-1})$$

where n is the number of unknown variables, j is the number of mesh points, and k is the designation for a particular unknown variable. Expanded into a Taylor series and the non-linear terms neglected:

$$0 = g_{i,j}^0 + \sum_k \left. \frac{\delta g_{i,j}}{\delta c_{k,j-1}} \right| * \Delta C_{k,j-1} + \sum_k \left. \frac{\delta g_{i,j}}{\delta c_{k,j}} \right| * \Delta C_{k,j} + \sum_k \left. \frac{\delta g_{i,j}}{\delta c_{k,j+1}} \right| * \Delta C_{k,j+1} \quad [2.25]$$

Equation 15 can be written:

$$g_{i,j}^0 = \sum_k (A_{i,k}^0 * \Delta C_{k,j-1} + B_{i,k}^0 * \Delta C_{k,j} + D_{i,k}^0 * \Delta C_{k,j+1}) \quad [2.26]$$

Equation 16 can then be written as a tridiagonal matrix (with respect to j):

$$\begin{bmatrix} B(1) & D(1) & & & & \\ A(2) & B(2) & D(2) & & & 0 \\ & A(3) & B(3) & & & \\ & & & \ddots & & \\ & & & & A(nj-1) & B(nj-1) & D(nj-1) \\ & 0 & & & & A(nj) & B(nj) \end{bmatrix} \Delta C = G \quad [2.27]$$

In the matrix A, B and D are six by six submatrices containing the six electrochemical equations mentioned in detail in Appendix B. It is a square matrix with its size depending on the number of mesh spaces in the one dimensional electrochemical model (aka the number of mesh spaces across a cell, from anode to cathode) [26]. In MATLAB, this is solved using the following equations:

$$\Delta C = M \backslash G \quad [2.28]$$

$$C = C_0 + \Delta C \quad [2.29]$$

where M is the matrix in equation 2.27 and “ \backslash ” is the operator used to invert matrix M in order to divide it by G . ΔC is the same as ΔC in equation 2.24 and it will change with each iteration of the method. The method is applied until $G = 0$. At this point the value for the particular unknown being solved for is accurate.

CHAPTER 3: NUMERICAL RESULTS

3.1 Design Optimization

For each configuration, there are various design considerations that will affect battery performance, durability, and safety. In this thesis tab location, cooling environment, current collector thickness, and risk of lithium plating are all explored in depth using the models described in Chapter 2.

In all of Chapter 3, a “base case” configuration is referred to multiple times. This refers to the specifications detailed in Appendix A for both the spirally wound and prismatically wound configurations. Unless otherwise noted, these specifications are used for the study.

Also it should be noted that many results are represented visually using color mapping. In all of the figures that display results, the minima and maxima used for the scale are the same for all cases that have been explored. This is done to make it easy for the reader to compare each different case (i.e. the temperature scale used for adiabatic, isothermal, air cooled and liquid cooled is that of the adiabatic case since it has the largest temperature range. All other cases use the same range so one can see how much better liquid cools down the battery versus adiabatic).

Lastly, the design considerations explored in this thesis are the same as those explored in Gerver et al. This was done so as to compare all three configurations (and how the design considerations affect each) easily.

3.1.1: SINGLE TAB VERSUS MULTIPLE TAB COMPARISON

Within a battery, all current that is generated flows to the aptly named current collectors. To extract the current from the battery, current collector tabs are utilized to connect the current collectors to the external circuit. As will be seen in this section, tab location(s) affects the current density and temperature distribution throughout the cell, which in turn affects the overall performance and durability of the battery.

It is desirable to have as close to uniform current density and temperature as possible (achieved by tabs spanning the entire length of each current collector), but it is also desirable to limit the amount of non-active material in portable batteries (achieved by as little tab material as possible). Therefore there is an opportunity for optimization by seeking to have uniform current density and temperature while limiting amount of tab material. Tab placement and number of tabs is an important design parameter for every battery and will be explored in this section.

3.1.1.1 Spiral Configuration – Tabs

In the following simulations five tab locations are explored (Figure 16) for the spiral configuration. In the figure each current collector is displayed as if the battery has been unwound and placed flat. The current collectors are shown as large blue or green rectangles and the tabs are represented by the small rectangles bordered by red and jutting out from various locations. Each illustration shows approximate size and location of the tabs on each current collector.

Case A is expected to be the worst case scenario for current density and temperature uniformity as it has small tabs located at the center post of the battery, while Case B is expected to be the best case scenario where the tabs span the entire length of each electrode. Cases C, D and E explore different options with location and number of tabs.

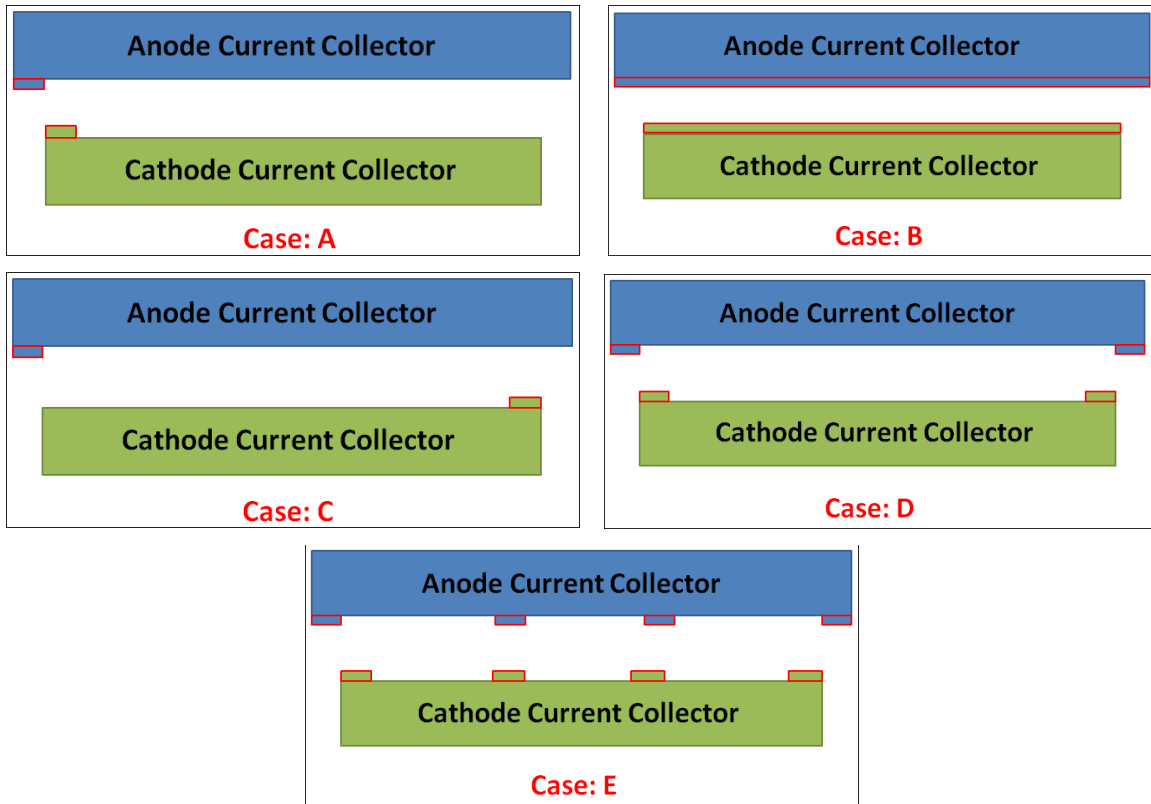


Figure 16: Five cases explored for tab location under discharge.

First, temperature gradients within a cell can cause issues with cell durability. Regions that are hotter than the rest of the cell usually degrade quicker than cooler regions. In the following simulations, temperature is shown in the plane of the separator after 30 seconds at a

discharge rate of 5C. All cases are adiabatic. These temperature values factor in heat generation from both the electrochemical reaction and heat from resistance within the current collectors. The results are nearly identical for the “inner electrode pair” (the cell where the anode is inside of the cathode) and the “outer electrode pair” (the cell where the anode is outside of the cathode), so for brevity only results for the former case are shown in Figure 16. Also the temperature range used for comparison is that of Case A since it has the largest (worst) temperature gradient across the cell.

Case A has both the smallest width tabs and least number of tabs, and they are located on both electrodes adjacent to the center post. This case has the greatest temperature difference across it, a delta value of 6.0 Kelvin. This is because the current generated at the nodes farthest away from the tabs has to travel the entire length of the current collector to exit the cell. Case B has tabs across the entire length of each electrode and has a temperature delta value of only 0.7 Kelvin across the cell. With such a small temperature delta value, this case has a relatively uniform temperature distribution. Current generated within this cell has little distance to travel to exit the cell. Case C’s anode tab is adjacent to the center post and cathode tab is at the edge of the outer-most cathode winding, and it has a temperature delta value of 1.1 Kelvin, but what is different than the first two cases is that the coolest part of the cell is in the bulk windings, away from either tab. This illustrates that the warmest part of the cell occurs around the tabs. Case D has tabs at the center post and at the edge of each electrode’s outer-most winding and has a temperature delta value of 2.1 Kelvin. Lastly Case E has four tabs on each electrode that are equidistant and it has a temperature delta value of 0.8 Kelvin.

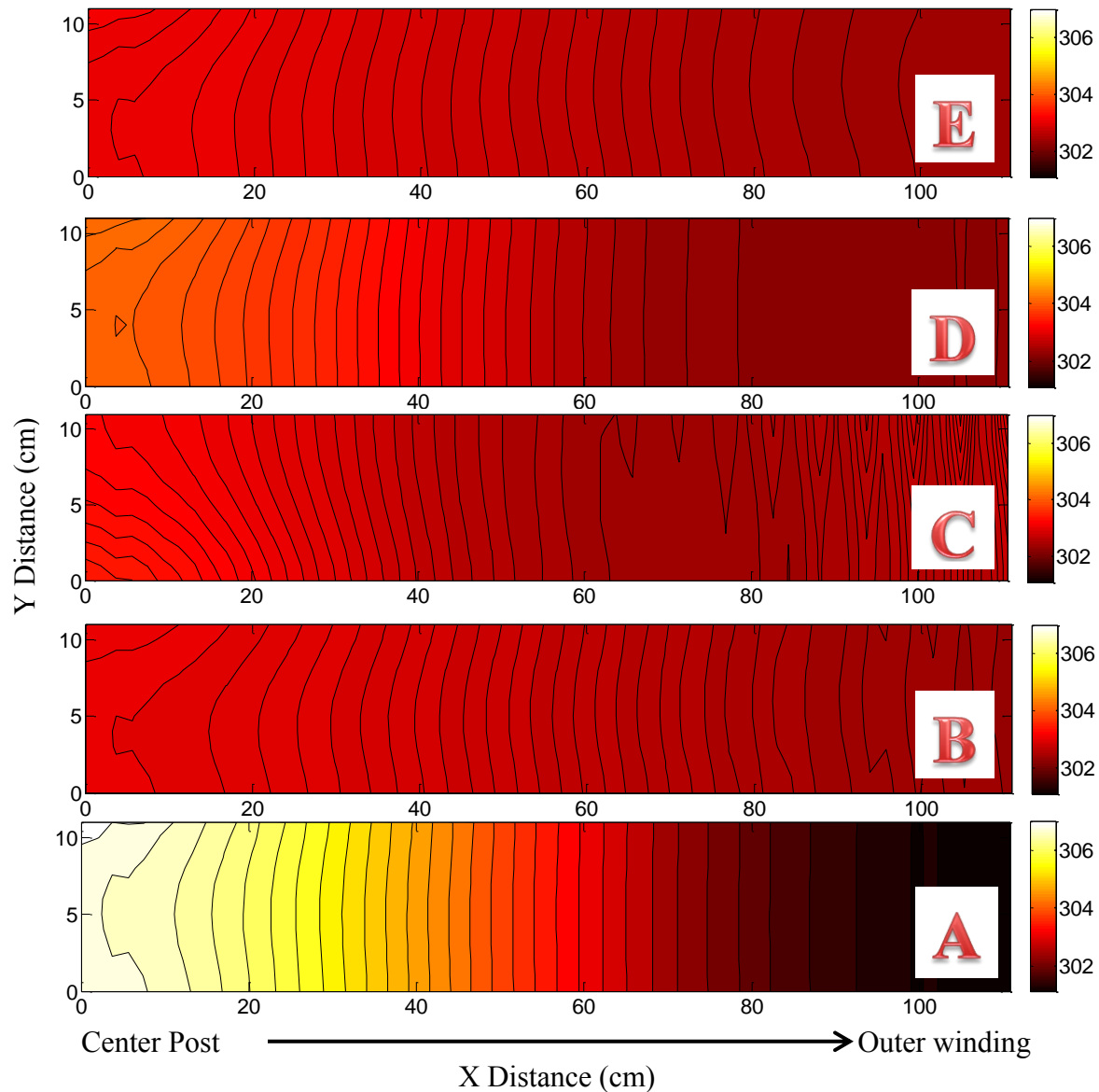


Figure 17: Temperature versus position for 5 different tab locations at a discharge rate of 5C.

From a current density perspective, uniformity is also important for durability of the battery as it is coupled with temperature distribution (in fact in the section that explores thermal environment around the battery, the degree to which temperature affects current density is explored further). Again the data is taken from a spirally wound battery after 30 seconds of running at a discharge rate of 5C. See Figure 18 for a comparison of the five cases. Using Case A’s scale as the range for which all other cases are compared, each display shows the difference between each node’s current density and the overall average

current density in the cell ($\Delta I = I_{x,y} - I_{avg}$). This difference, ΔI , is used to show how far each node strays from average; ideally the entire current collector would have the same current density across it, so these displays show how far from average (uniformity) each node is throughout the current collector.

It is clearly evident that Case A is the least uniform and that any of the four other cases provides more uniform current density across the cell, with Case B being the most uniform followed by Case E. Specific values for the difference in current density range can be found in Table 1.

Case	Delta Current Density Range (A/cm²)
A	-0.0073 – 0.0094
B	-0.0011 – 0.00096
C	-0.0017 - 0.0039
D	-0.0025 - 0.0050
E	-0.0010 - 0.0019

Table 1: Range of delta current density values for each tab location case.

Having multiple tabs or wide tabs allows for more uniform current density across the cell and therefore more uniform temperature distribution. This can be attributed to the fact that the current being drawn from the cell is spread out over more tab material which has less resistance and creates less heat. In a multiple tab configuration, the current has less distance to travel across a current collector to reach a tab and therefore generates less heat through ohmic resistance.

From a temperature uniformity standpoint, while the electrodes that have tabs running the entire edge (Case B) provide the best temperature distribution, there is only a minor increase in temperature difference across the cell for Case E. From a current density uniformity standpoint, having any configuration other than both tabs along the center post is an improvement. Having tabs stretch the entire length of the current collector is best but Case E is a close second place. Therefore, having four tabs spaced equidistantly along the length of each current collector (as in Case E) is a good

compromise between amount of tab material and current density / temperature uniformity.

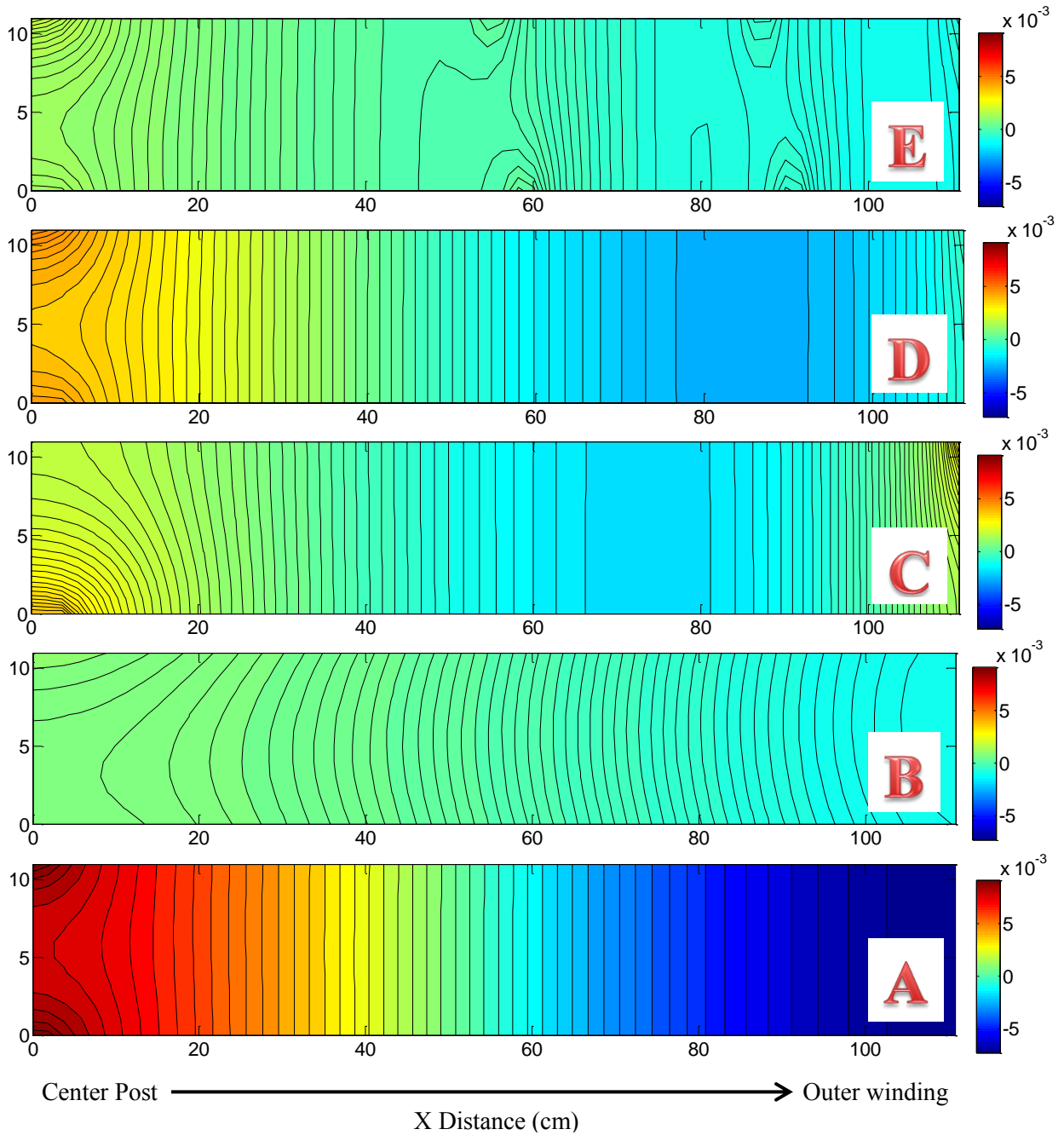


Figure 18: Delta current density versus position for 5 different tab locations at a discharge rate of 5C. Delta current density = current density – average current density.

One last point is that this tab location exploration drives where the current will exit/enter the cell. By comparing the results in Figure 18 to Figure 17, it is evident that regions in which there is higher current density will in fact have an increased local temperature and vice versa. This makes sense since the electrochemical and thermal models are coupled, but it is important to determine if one parameter causes the other or if they are perfectly coupled. Since these simulations control the current density flowing through the tabs, one is able to conclude that increased current density will lead to increased temperatures. In a later section that explores the thermal environment around the battery, the degree to which temperature change affects current density is explored.

3.1.1.2 Prismatically Wound Configuration – Tabs

In the following simulations six tab locations are explored. See Figure 19 for illustrations of tab placement, where each current collector is displayed as if the battery has been unwound and placed flat. The current collectors are shown as large rectangles and the tabs are represented by the short rectangles bordered by red and jutting out from various locations. Each illustration shows approximate size and location of the tabs on each current collector.

Similar to the spirally wound configuration simulations, Case A is expected to be the worst case scenario as it has small tabs located at the center post of the battery, while Case B is expected to be the best case scenario where the tabs span the entire length of each electrode. Cases C, D, E, and F explore different options with location and number of tabs.

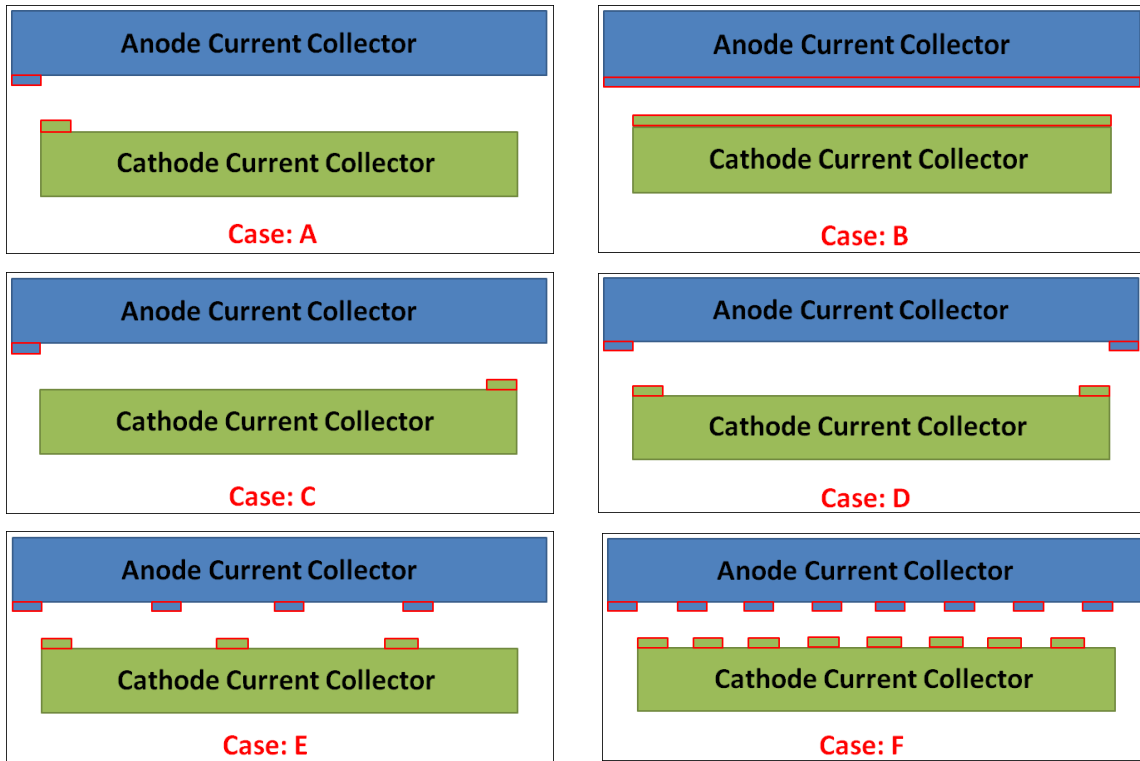


Figure 19: Six cases explored for tab location under discharge.

In the following prismatic wound configuration simulations, temperature is shown in the plane of the separator after 30 seconds of a discharge rate of 5C. The temperature values include heat generation from both the electrochemical reaction and heat from resistance within the current collectors. All cases are adiabatic. As with the spirally wound section, only the inner electrode pair is displayed due to similar results for both cells. Also the temperature range used for comparison is that of Case A since it has the largest (worst) temperature gradient across the cell.

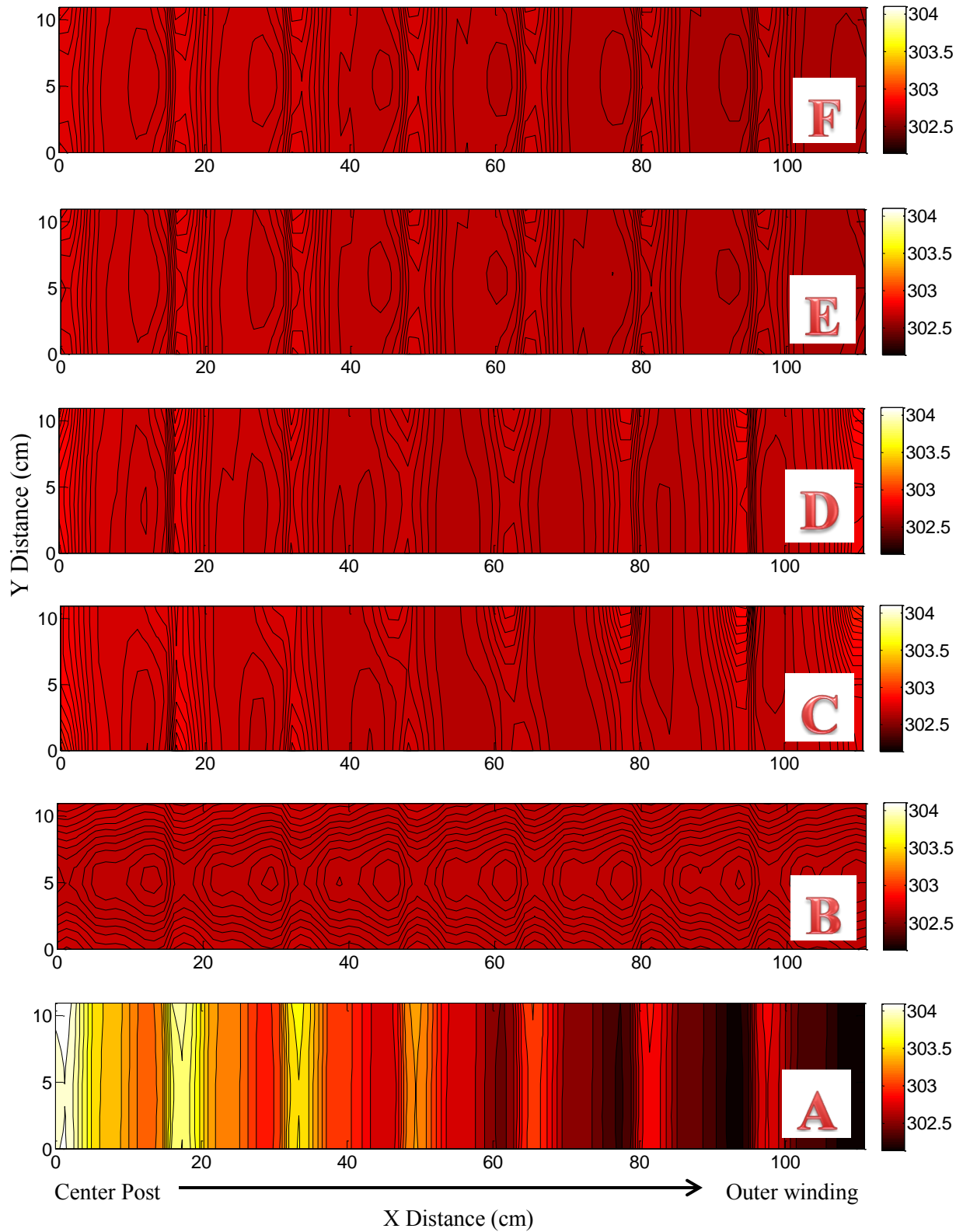


Figure 20: Temperature vs. position. Periodic nature of results explained in this section.

Results from these simulations can be found in Table 2, which gives minimum and maximum temperatures. Figure 20 shows absolute temperatures across the cell. Case A has the least number of tabs, and they are located on both electrodes adjacent to the center post and running along the planar edge of the cell. This case has the greatest temperature difference, a delta value of 2.0 Kelvin, across the cell. Case B has tabs across the entire length of each electrode and has a temperature delta value of only 0.03 Kelvin across the cell. As expected this case has a relatively uniform temperature distribution and is coolest on the outer winding. Cases C – F each have different number of tabs but have similar results to one another with a delta temperature across the cell of 0.2 – 0.3 Kelvin. From a temperature uniformity standpoint, any of these four cases would be a reasonable solution.

It should be noted that in the prismatically wound configuration, each winding of the battery is evident thermally. One can see in Figure 20 each of the seven layers for that particular configuration and number of windings. Whether current density shows the same results or not will be explored next.

Case	Temperature Range (K)
A	302.1567 - 304.2460
B	302.6683 - 302.6988
C	302.6534 - 302.9751
D	302.6435 - 302.9065
E	302.6230 - 302.8147
F	302.6058 - 302.8055

Table 2: Temperature range for each tab case.

For current density, the data is taken from a base case prismatically wound battery after 30 seconds of running at a discharge rate of 5C. See Figure 21 for a comparison of the six cases. Using Case A's delta current density scale as the range for comparison, each display shows the difference between each node's current density and the overall average current density in the cell ($\Delta I = I_{x,y} - I_{avg}$). Specific values for the difference in current density range can be found in Table 3.

Case	Delta Current Density Range (A/cm²)
A	-0.0055 - 0.0108
B	-8.743e-05 - 1.247e-04
C	-0.0014 - 0.0046
D	-0.0014 - 0.0037
E	-4.573e-04 - 0.0013
F	-6.625e-04 - 9.167e-04

Table 3: Range of delta current density values for each tab location case.

Case A has the least current density uniformity but still the current density range is not very large. As expected, the more tabs there are the more uniform the current density. Simply placing each electrode's single tab at opposite ends of the cell (Case C) improves the uniformity by an order of magnitude. Adding an additional node to each electrode (Case D) does not offer much improvement over Case C. Cases E and F provide more uniformity than C and D but there is not much difference between E and F.

In conclusion from a temperature and current density perspective, any of the different tab numbers and locations from Cases B – F would offer an improvement over Case A. Case E, which has tabs evenly spaced and located on every other tab, is recommended to provide sufficient current and temperature uniformity across the battery while limiting amount of non-active tab material.

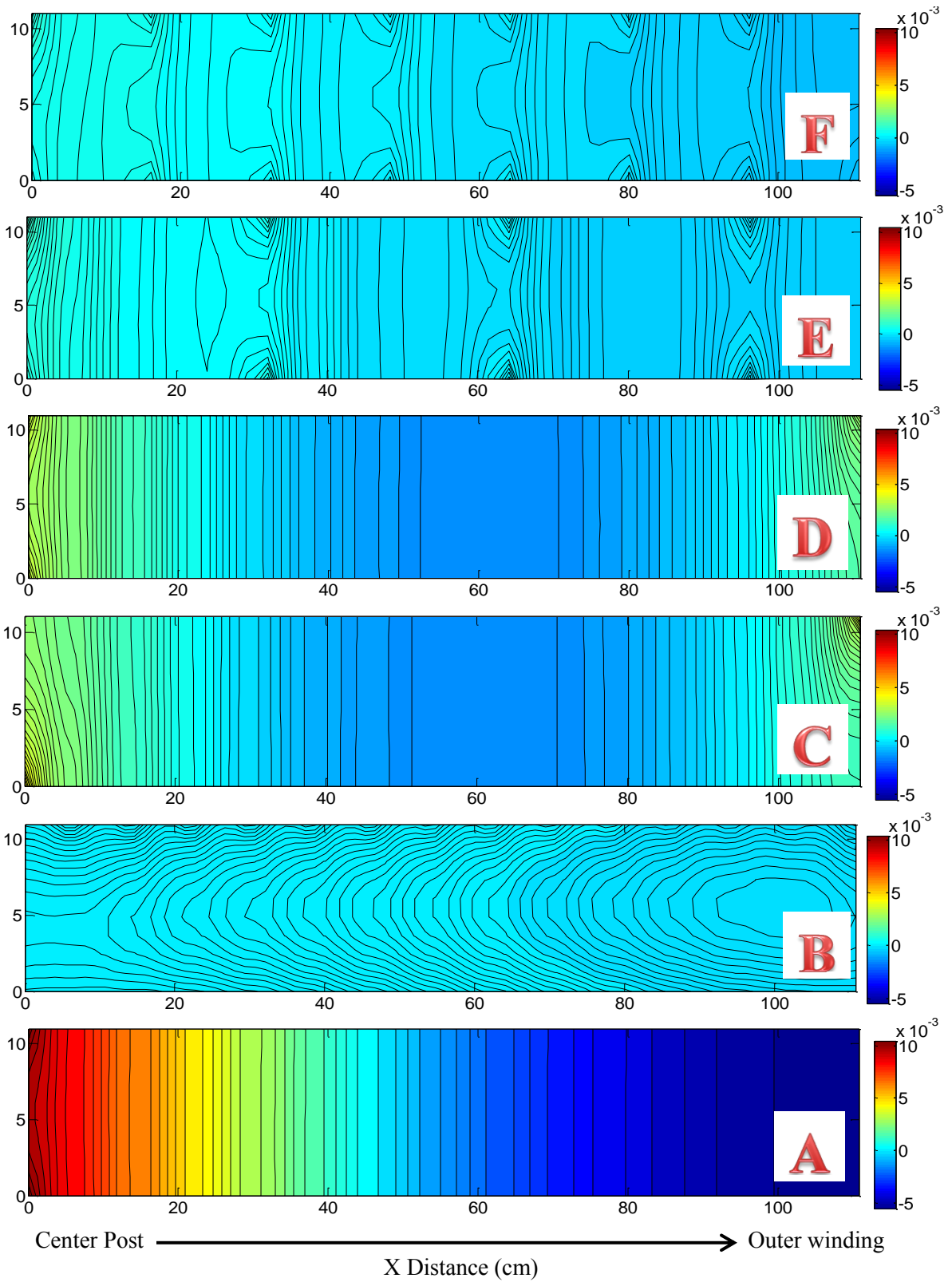


Figure 21: Delta current density vs. position.

What may be most interesting is the comparison of results in Figures 20 and 21. In section 3.1.1.1, the spirally wound battery showed that regions of increased current density were also regions of increased temperature. Here, that is not the case. Specifically looking at Case A, one can see in Figure 20 that there is a temperature gradient across each of the seven layers of the cell, but in Figure 21 there is nothing to indicate the different layers of the cell; there is merely a single current density gradient across the entire cell. This leads one to conclude that a heightened local temperature will not cause a higher local current density. This supports the findings found in the thermal environment section for the spirally wound battery. When one looks closer at Figure 20, it can be seen that there is an overall temperature gradient from the center post to the outer winding. This supports the claim that increased current density will lead to increased temperatures. While a small portion of these results may be related to limitations of the model, overall it shows that current density will have a greater effect on temperature than vice versa. Therefore to increase durability of the battery, it is imperative to have as close to uniform current density as possible.

3.1.2: COOLING METHOD COMPARISON

When designing a battery system, heat is constantly generated within the cell and therefore heat management must be considered. If not, there may be a risk of thermal runaway or localized high temperatures resulting in material degradation and cell failure. Proper heat management can increase safety and durability for a battery.

3.1.2.1 Spiral Configuration – Cooling Method

For the spirally wound battery, four different cases are compared: adiabatic, air cooled, liquid cooled and isothermal. The results in Figure 22 show a map of the temperature within the plane of the separator between the anode – cathode electrodes after 30 seconds of discharging at a rate of 5C. For each case the image of the inner electrode pair is above that of the outer electrode pair. Case A is adiabatic and since it will have the largest temperature gradient, its scale will be used for all other cases for comparison. Case B is air cooled along the top edge, bottom edge and outer-most

winding with a heat transfer coefficient for convection set to 0.0005 W/cm² K. Case C is liquid cooled along the top edge, bottom edge and outer-most winding with a heat transfer coefficient for convection set to 0.01 W/cm² K. Case D is isothermal with a constant temperature of 298K.

Table 4 provides the minimum and maximum temperatures across the cell. As can be seen in Figure 22 and Table 4, the adiabatic case (A) provides the largest temperature gradient across the cell. Cooling the battery with air (B) provides lower temperatures overall and has a similar *looking* gradient in temperature across the cell with the area around the center post having the highest temperature. Liquid cooling (C) also provides lower temperatures overall but the hottest part of the cell shifts to the “bulk windings” which consists of the layers of the battery that are barely exposed to the cooling liquid (only top and bottom edges) and are insulated by the many other layers around it. The liquid cooling case has a heat transfer coefficient several orders of magnitude larger than air cooled which explains why it is so much more effective at cooling the outer windings and even top and bottom regions of the cell. The isothermal case (D) is obviously uniform across the cell and is not shown.

Case	Min. Temp Kelvin (Inner Electrode Pair)	Max. Temp Kelvin (Inner Electrode Pair)	Min. Temp Kelvin (Outer Electrode Pair)	Max. Temp Kelvin (Outer Electrode Pair)
A	301.0912	307.1659	301.0810	307.1001
B	301.4050	304.8275	301.3909	304.8222
C	300.7089	303.6919	300.6265	303.6900
D	298	298	298	298

Table 4: Range of temperatures in Kelvin values for four different thermal environments – adiabatic (A), air cooling (B), liquid cooling (C), and isothermal (D) after 30 seconds of 5C discharge.

It is clear that both air and liquid cooling methods reduce the peak temperature within the battery but more importantly, they have more uniform temperature

distributions. If one is looking for maximum heat management then liquid cooling is recommended. Next it will be interesting to explore how cooling method affects current density throughout the cell.

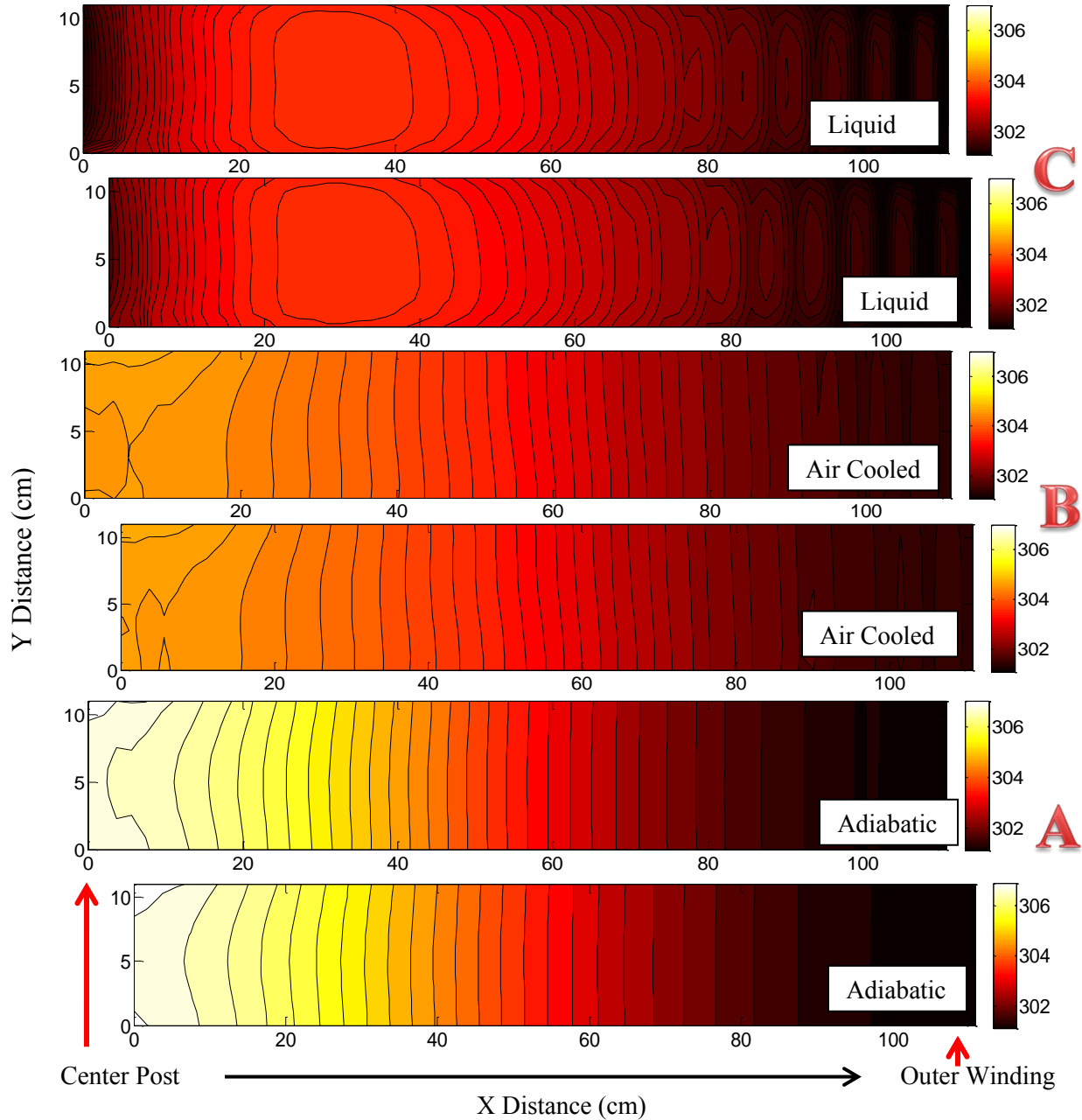


Figure 22: Temperature distribution (in Kelvin) of the both electrode pairs for three cooling methods after 30 seconds of 5C discharge. The inner electrode pair is on top of the outer electrode pair for each case.

Table 5 displays the delta current density range for each cell of the spirally wound configuration. From the data, cooling the battery with air or liquid will improve current density uniformity but not by a significant amount. Also the isothermal case is very similar to the adiabatic case. These findings show that for this particular base case spirally wound battery the temperature distribution will not make a major impact on current density uniformity.

Case	Inner Electrode Pair		Outer Electrode Pair	
	Min. Delta Current Density (A/cm ²)	Max. Delta Current Density (A/cm ²)	Min. Delta Current Density (A/cm ²)	Max. Delta Current Density (A/cm ²)
A	-0.0073	0.0094	-0.0069	0.0097
B	-0.0054	0.0048	-0.0053	0.0050
C	-0.0054	0.0043	-0.0053	0.0046
D	-0.0067	0.0083	-0.0063	0.0086

Table 5: Range of current densities values for four different thermal environments – adiabatic (A), air cooling (B), liquid cooling (C), and isothermal (D) after 30 seconds of 5C discharge.

Figure 23 shows diagrams of the four thermal environments for the battery. The delta current density range of -0.0073 to 0.0097 A/cm² in each case is that of the most non-uniform case, the adiabatic environment. Note that even though Case D is isothermal, there is still a clear gradient in current density and it is quite similar to Case A (adiabatic). Also in Case C, the hottest part of the cell is about 1/3 of the total distance from the center post yet looking at Figure 23, Case C does not show signs of elevated current density. These examples show that for this model of a spirally wound battery, the thermal environment will not affect the current density distribution greatly.

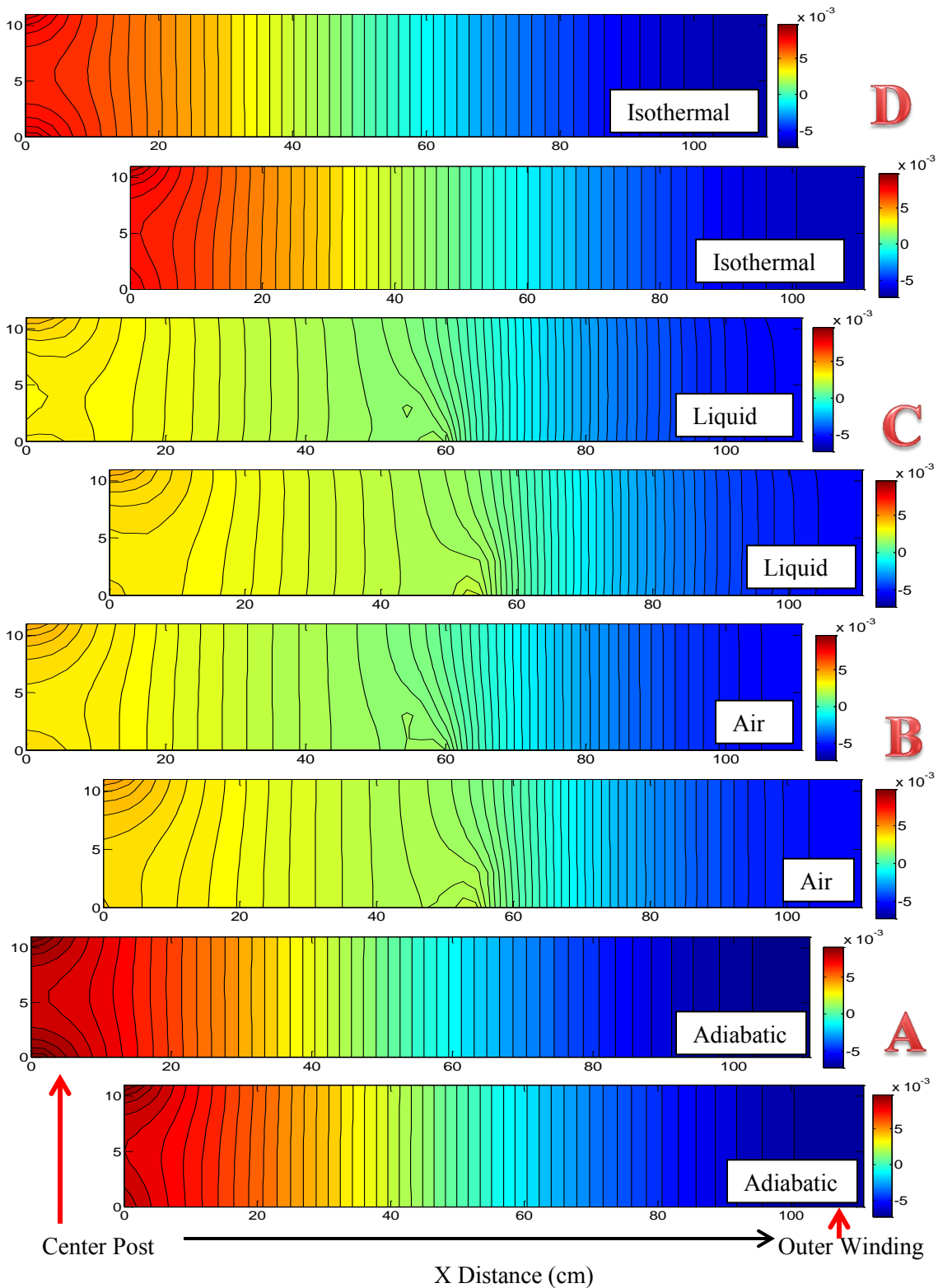


Figure 23: Delta current density for all four thermal environments after 30 seconds of 5C discharge. Inner electrode pair is above the outer electrode pair for each case.

3.1.2.2 Prismatic Configuration – Cooling Method

For the prismatically wound battery, four different cases are compared: adiabatic, air cooled, liquid cooled and isothermal. The diagrams in Figure 24 show the absolute temperatures across each cell after 30 seconds of discharging at a rate of 5C. For each case the image of the inner electrode pair is above that of the outer electrode pair. Case A is adiabatic and since it will have the largest temperature gradient across the cell, its temperature scale will be used for all cases for comparison. Case B is air cooled with a heat transfer coefficient for convection set to 0.0005 W/cm² K, case C is liquid cooled with a heat transfer coefficient for convection set to 0.01 W/cm² K, and case D is isothermal with a constant temperature of 298K.

As can be seen in Figure 24, each successive layer in the prismatically wound battery has its own temperature gradient. One can pick out where each layer begins and ends. Each layer is hottest in the region where the tabs are located. Table 6 provides the minimum and maximum temperatures across the cell. From the figure and table, one can see that the adiabatic and air cooled thermal environments are nearly identical. For this particular geometry and these particular dimensions, air cooling clearly does not provide a large improvement in neither absolute temperature nor uniformity. This may be because only the outer winding, top edge and bottom edge of the battery are exposed to the air, which itself has a low heat transfer coefficient. However, using liquid to cool the battery does lower the absolute temperature and improves the uniformity slightly.

Case	Min. Temp Kelvin (Inner Electrode Pair)	Max. Temp Kelvin (Inner Electrode Pair)	Min. Temp Kelvin (Outer Electrode Pair)	Max. Temp Kelvin (Outer Electrode Pair)
A	302.1567	304.2460	302.1398	304.1907
B	302.1043	304.1763	302.0823	304.1274
C	301.1984	303.1746	301.1035	303.1571
D	298	298	298	298

Table 6: Range of temperatures in Kelvin values for four different thermal environments – adiabatic (A), air cooling (B), liquid cooling (C), and isothermal (D) after 30 seconds of 5C discharge.

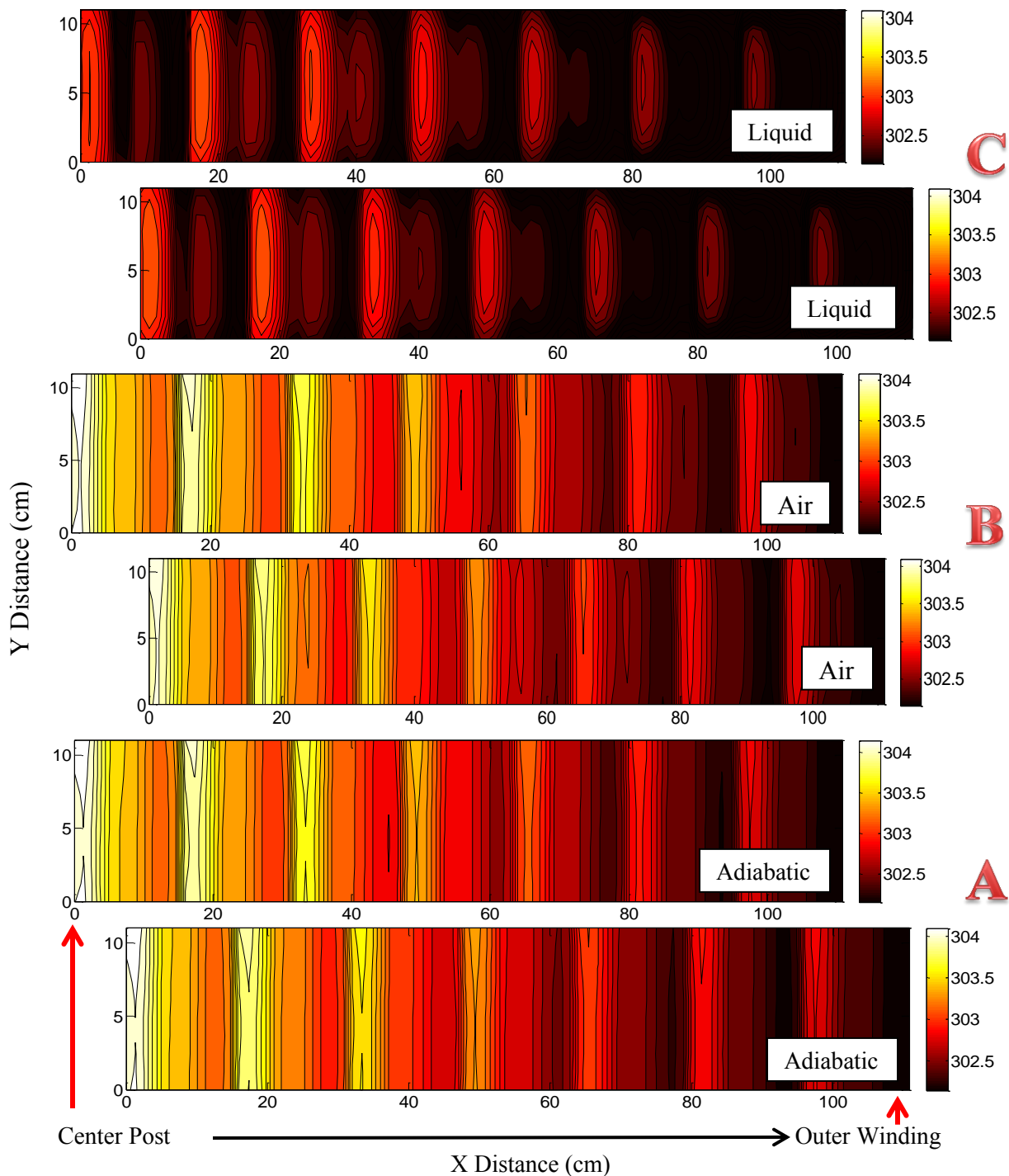


Figure 24: Temperature distribution (in Kelvin) of the both electrode pairs. The inner electrode pair is on top of the outer electrode pair for each case. The periodic nature of these results is explained in this section.

Table 7 displays the delta current density range for each cell of the prismatically wound configuration. From the data, cooling the battery with air or liquid will not improve current density uniformity by a significant amount versus the adiabatic case. The isothermal case looks to provide the best uniformity, again not by a significant amount.

Case	Inner Electrode Pair		Outer Electrode Pair	
	Min. Delta Current Density (A/cm ²)	Max. Delta Current Density (A/cm ²)	Min. Delta Current Density (A/cm ²)	Max. Delta Current Density (A/cm ²)
A	-0.0055	0.0108	-0.0046	0.0105
B	-0.0055	0.0107	-0.0046	0.0105
C	-0.0055	0.0105	-0.0046	0.0103
D	-0.0052	0.0099	-0.0043	0.0097

Table 7: Range of current densities values for four different thermal environments – adiabatic (A), air cooling (B), liquid cooling (C), and isothermal (D) after 30 seconds of 5C discharge.

Figure 25 shows diagrams of the four thermal environments for the battery. The delta current density range of -0.0055 to 0.0108 A/cm² in each case is that of the most non-uniform case, the adiabatic environment. For all cases, regions that are warmest and coolest with respect to the rest of the cell do not seem to affect current density. From these diagrams one is not able to determine where the tabs or successive layers are. Similar to the spirally wound battery, the thermal environment surrounding the battery in this model does not greatly affect current density.

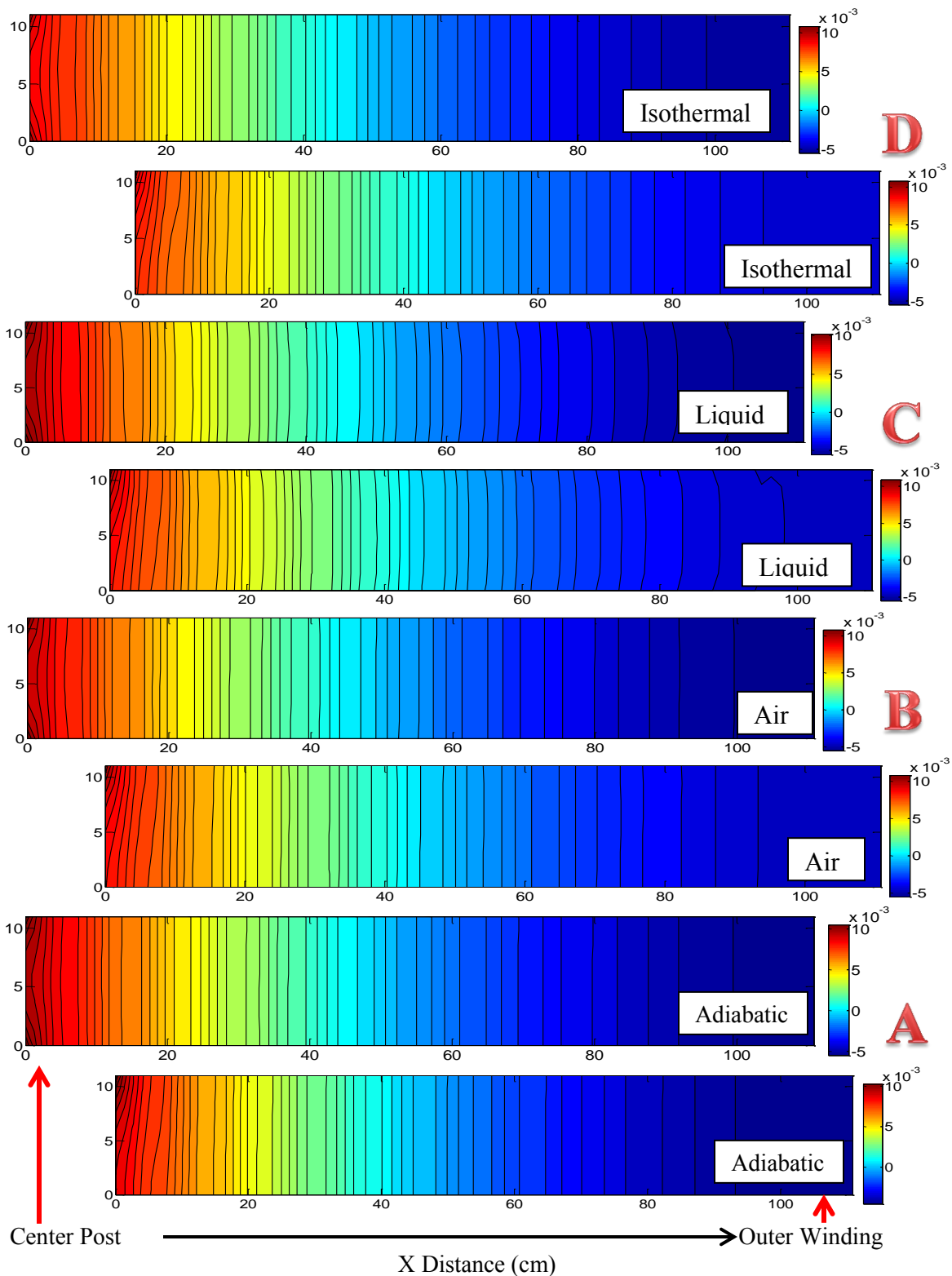


Figure 25: Delta current density of both electrode pairs for all four thermal environments. Inner electrode pair is on top of the outer electrode pair for each case.

3.1.3: CURRENT COLLECTOR THICKNESS COMPARISON

When designing a battery system, current collector thickness is another important variable. It can have an effect on temperature distribution, current density uniformity, power, power density and efficiency. Typically as the thickness of a current collector increases, conductance within the cell should increase:

$$\text{Conductance} = \frac{\text{Conductivity} * \text{Cross Sectional Area}}{\text{Length}} \quad [1]$$

where the *Cross Sectional Area* is the term in equation [1] that will increase with increasing collector thickness, *Conductivity* is inherent to the material properties, and *Length* is the distance between two points in which the conductance between them is desired. A higher conductance means lower resistance which in turn means lower ohmic losses (I^2R). The downside is that thicker current collectors results in more non-active material being added to the battery. This is an area in which current collector thickness can be optimized to find the maximum conductance while limiting non-active material; a study of power and power density will provide a solution to this optimization analysis.

3.1.3.1 Spiral Configuration – Collector Thickness

In the following study, the base case spirally wound battery (Appendix A) is used with only the current collector thickness varying from case to case. Power is calculated from the values measured for total current and total cell voltage at the tabs. This is taken 5 seconds into a discharge at a rate of 5C and is an instantaneous reading so temperature and concentration gradients are ignored. Power density is calculated by dividing power by volume of the battery, neglecting volume from casing and tabs. The six current collector thicknesses are 0.0005, 0.001, 0.002, 0.003, 0.004, and 0.005 (cm). The values listed are that of the aluminum current collector (cathode under discharge). Similar to Rachel Gerver's work [22], the copper current collector (anode) is slightly thinner so that it has the same conductivity as the aluminum collector. As can be found in Table 8, the volume increase of the battery is significant with increasing current collector thickness. The 0.005cm thick current collector increases the overall volume 22.88% versus the 0.0005cm thick current collector.

Thickness (cm)	Battery Volume (cm ³)	Volume Change (%)
0.0005	68.46	0.00
0.001	70.13	2.43
0.002	73.51	7.37
0.003	76.27	11.41
0.004	80.51	17.60
0.005	84.13	22.88

Table 8: Battery volume increase is significant with increasing current collector thickness.

In Figure 26, power is displayed and as expected it increases with increasing current collector thickness. In Figure 27, power density is displayed. Power density for this particular spirally wound battery configuration and c-rate appears to peak for an aluminum current collector thickness between 0.002 and 0.003 cm. It should be noted that power density will vary depending on size and discharge rate [22].

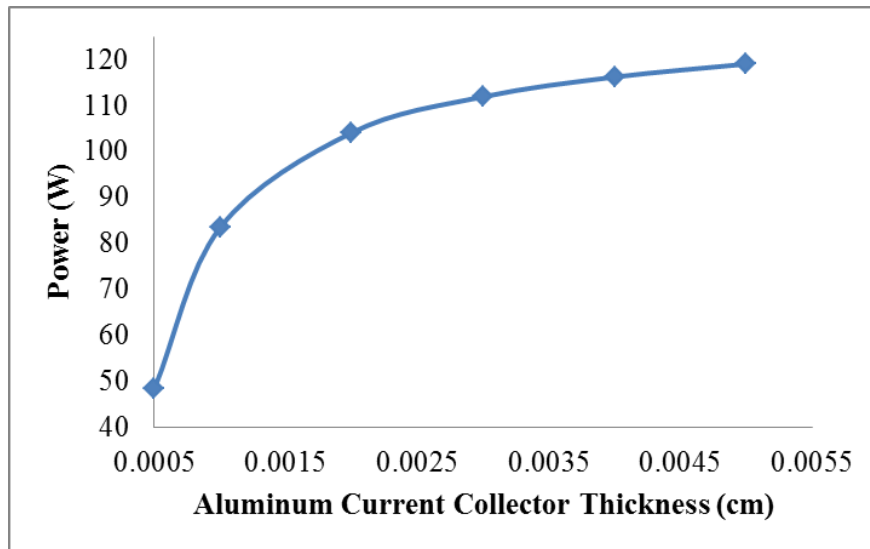


Figure 26: Power increases as current collector thickness increases.

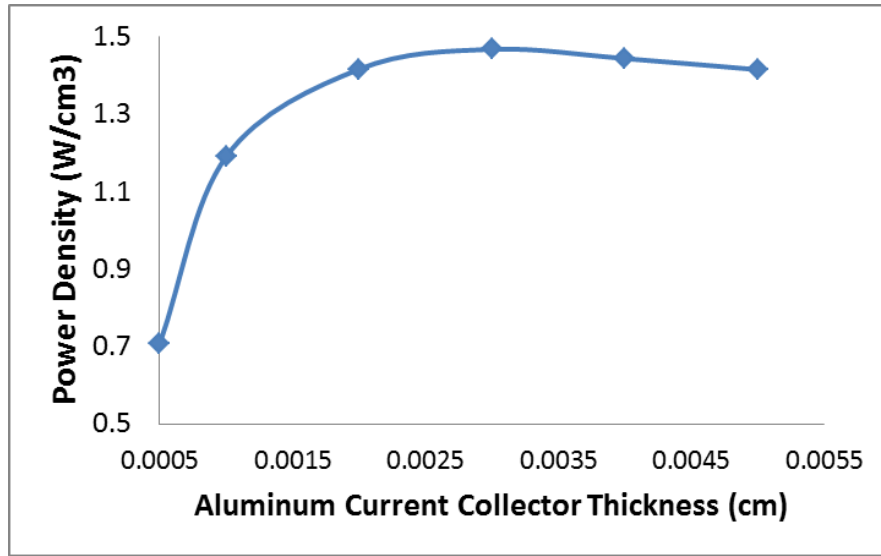


Figure 27: Power density versus aluminum current collector thickness (cathode under discharge).

Current collector thickness also affects current density uniformity since conductance increases with increasing current collector thickness. Results for the six current collector thicknesses can be found in Figure 28 and Table 9. Figure 28 shows the difference between current density for each location within the cell and average current density ($\Delta I = I_{x,y} - I_{avg}$). Since tab locations and cooling method are the same for all cases, only the inner electrode pair current densities are displayed. Table 9 shows the delta current density range of each case.

As one might expect, the current density across the cell becomes more uniform as the current collector thickness increases. When looking at all three figures, particularly Figure 28, and the values from Table 9, an aluminum current collector thickness from 0.002 – 0.003cm may be best for optimizing power, power density, and current density uniformity for this particular spirally wound configuration discharging at a 5C rate.

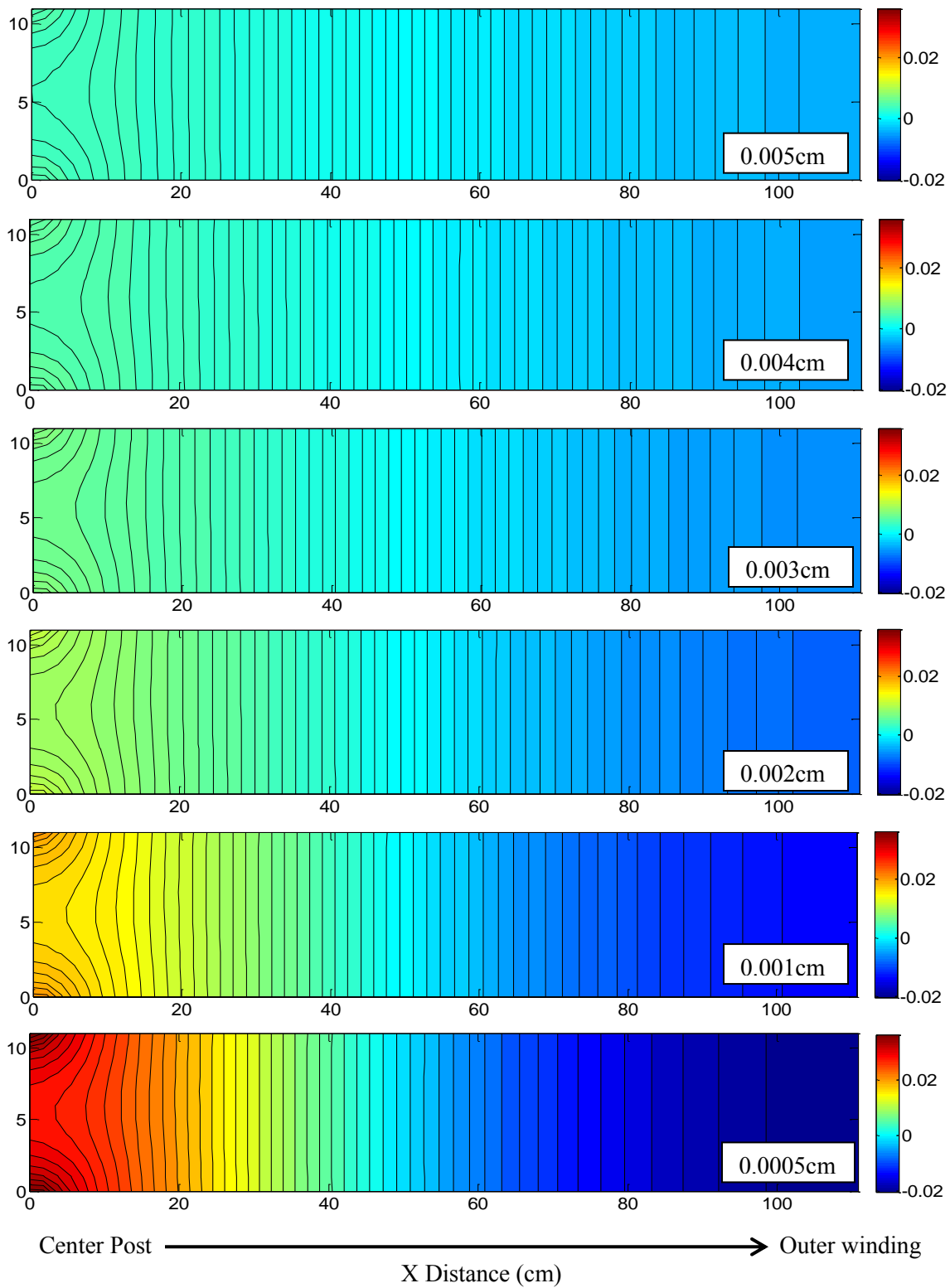


Figure 28: Delta current density versus position for different current collector thicknesses

Thickness	Delta Current Density Range (A/cm²)
0.0005	-0.0203 to 0.0371
0.001	-0.0135 to 0.0210
0.002	-0.0081 to 0.0114
0.003	-0.0059 to 0.0079
0.004	-0.0046 to 0.0061
0.005	-0.0038 to 0.0050

Table 9: Range of delta current density values for each current collector thickness.

3.1.3.2 Prismatically Wound Configuration – Collector Thickness

In the following simulations, the inputs from the base case prismatically wound battery are used with only the current collector thickness varying from case to case. Power is calculated from the values measured for total current and total cell voltage at the tabs. This is taken 5 seconds into a discharge at a rate of 5C. Since it is an instantaneous reading and power is of primary interest, temperature and concentration gradients are ignored. Power Density is calculated by dividing power by volume of the battery, neglecting volume from casing and tabs. The six current collector thicknesses are 0.0005, 0.001, 0.002, 0.003, 0.004, and 0.005 (cm). The values listed are that of the aluminum current collector (cathode under discharge). Similar the spirally wound battery simulations, the copper current collector (anode) is slightly thinner so that it has the same conductivity as the aluminum collector. As can be found in Table 10, the volume increase of the battery is significant with increasing current collector thickness. The 0.005cm thick current collector increases the overall volume 14.01% versus the 0.0005cm thick current collector.

Thickness (cm)	Battery Volume (cm ³)	Volume Change (%)
0.0005	68.46	0.00
0.001	70.13	1.54
0.002	73.51	4.64
0.003	76.27	7.75
0.004	80.51	10.88
0.005	84.13	14.01

Table 10: Battery volume increase is significant with increasing current collector thickness.

In Figure 29, power is displayed and as expected it increases with increasing current collector thickness. In Figure 30, power density is displayed. Power density for this particular C-rate peaks and levels out at thicknesses of 0.003, 0.004 and 0.005 cm. Upon examination of the numbers in Table 11, the power density for the 0.003cm thick collector is the highest.

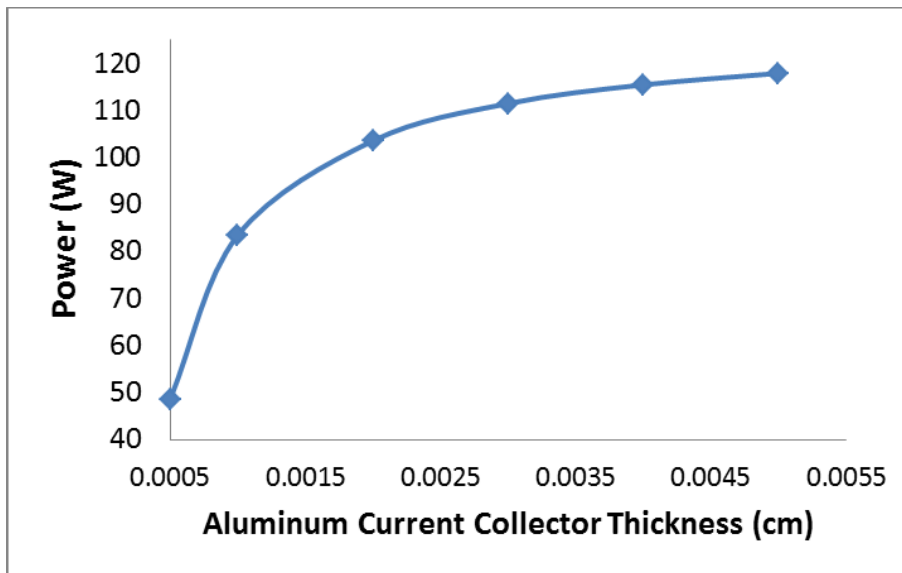


Figure 29: Power increases as current collector thickness increases.

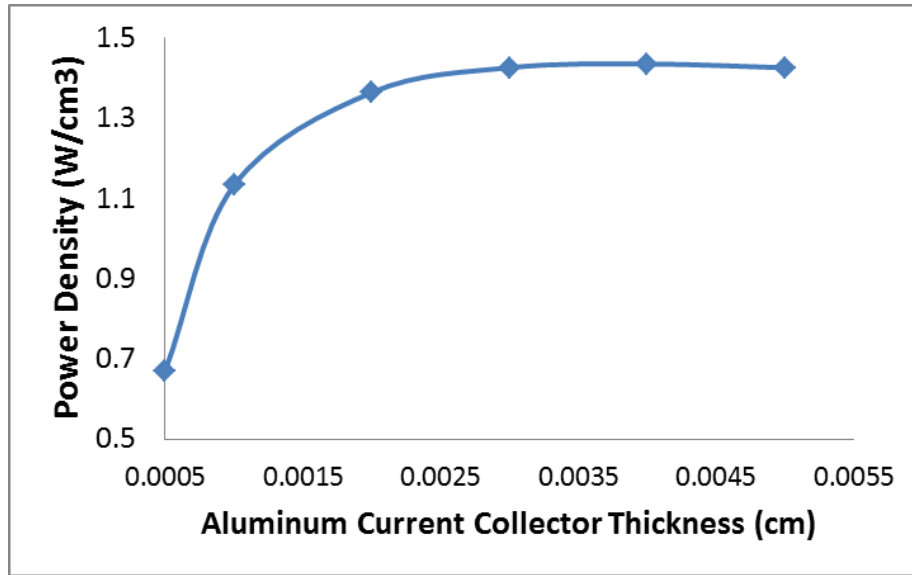


Figure 30: Power density versus aluminum current collector thickness (cathode under discharge).

Current Collector Thickness (cm)	Power (W)	Power Density (W/cm3)
0.002	111.4522	1.425954808
0.003	115.4278	1.435167483
0.004	117.8947	1.425579548

Table 11: Power and power density of the three highest current collector thicknesses.

Results with respect to current density for the six current collector thicknesses can be found in Figure 31 and Table 12. Figure 3 shows the difference between current density for each location within the cell and average current density ($\Delta I = I_{x,y} - I_{avg}$). Only the inner electrode pair current densities are displayed since the results are similar for both cells and showing both would be redundant. Table 12 shows the difference in current density range of each case.

Thickness (cm)	Delta Current Density Range (A/cm²)
0.0005	-0.0155 - 0.0454
0.001	-0.0106 - 0.0258
0.002	-0.0064 - 0.0141
0.003	-0.0046 - 0.0096
0.004	-0.0036 - 0.0073
0.005	-0.0029 - 0.0059

Table 12: Range of delta current density values for each current collector thickness.

The thinnest current collector has the worst current density uniformity and it improves as the thickness is increased. The region around the tabs provides the largest deviation from the average current density for all thicknesses. Glancing at the values in Table 12 and the plots in Figure 31, the improvement in current density uniformity becomes smaller with each increase in current collector thickness, meaning the improvement in uniformity from 0.0005cm to 0.001cm is much greater than the improvement from 0.004cm to 0.005cm.

Power density and current density uniformity is virtually the same for 0.003, 0.004 and 0.005cm thick aluminum current collectors. One may value the slight increase of power with the thicker current collectors and choose 0.005cm thick material. Since weight is also important for portable battery applications, one may elect to choose the 0.003cm thick material to reduce overall weight.

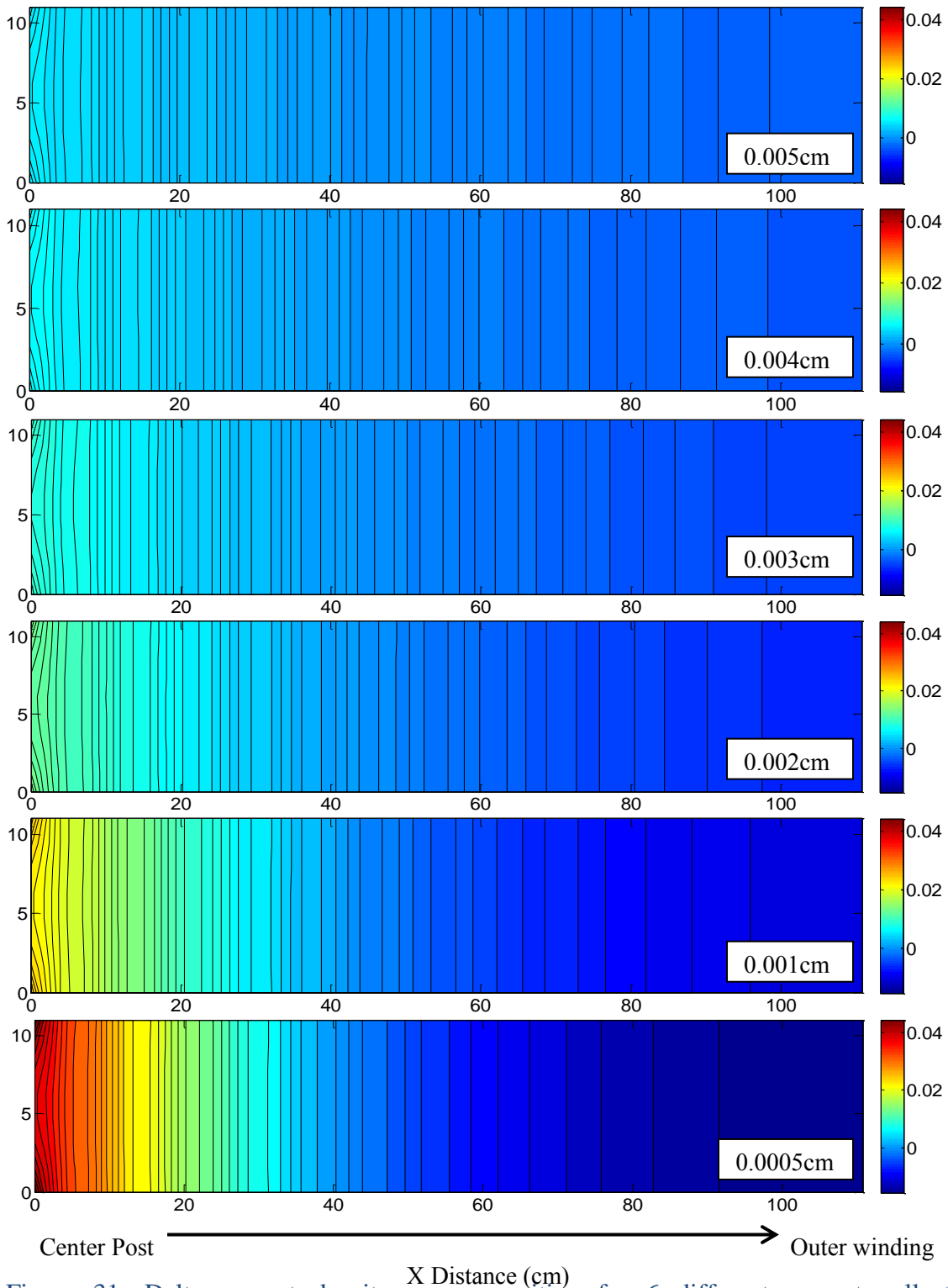


Figure 31: Delta current density versus position for 6 different current collector thicknesses at a discharge rate of 5C. Delta current density = current density – average current density.

3.1.4 LITHIUM PLATING

Lithium plating is a major concern when utilizing a lithium ion battery for safety and durability reasons. Early secondary lithium batteries that used lithium metal as the negative electrode material were quite unstable. Upon charging, dendrites would form on the negative electrode and pierce the separator, effectively causing a short circuit and thermal runaway. With graphite as the negative electrode, lithium can safely be inserted into the material at low enough currents. There is still potential for lithium to plate out onto the graphite when the local potential of the electrolyte is greater than the adjacent electrode ($\phi_{\text{electrode}} - \phi_{\text{electrolyte}} = \text{negative}$). If this occurs, dendrites can form and also that pathway for lithium insertion will be blocked thus causing increased resistance (and temperature) within the cell.

In portable applications such as a laptop or cell phone, this is not so much of a concern at this point as the charging system is regulated by a low current. In hybrid or electric vehicle operations, this cannot be regulated as easily since the battery is frequently being charged and discharged. During regenerative braking a high amount of power is generated and sent to the battery for charging. If the current sent to the battery is not regulated then lithium plating is highly likely. Therefore to maximize the amount of recovered energy safely, it is necessary to find the maximum charging rate that can be used without risk of lithium plating.

3.1.4.1 Spiral Configuration – Li Plating

In this section, various C-rates are explored to find what rates are possible and for how much time can pass before lithium plating occurs. As demonstrated by Gerver [22], a discharging event prior to charging can affect the likelihood of lithium plating and it is explored as well. First the number and size of tabs will be explored to see if they affect lithium plating. All five cases of tab location are explored. See section 3.1.1.1 for exact layouts of each case.

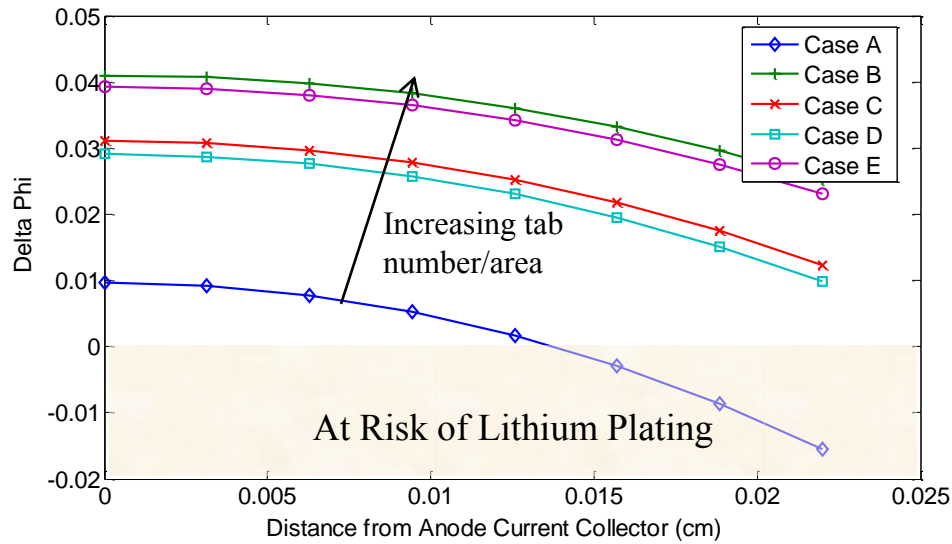


Figure 32: Tab location and size plays a role in lithium plating.

For this test, the base case spiral battery was explored at a charging rate of 1C. The potential difference between electrolyte and negative electrode was taken after 1 second in the corner of the battery that is adjacent to the center post where there is a tab for all five cases. As can be seen in Figure 32, tab location and size does factor into whether lithium will plate out on the negative electrode during charging. As expected the battery with only one small tab per electrode (Case A) is showing signs of plating already and the battery with tabs running the entire length of each electrode (Case B) is the least likely to have lithium plate out. This difference is due to the high current needing to flow through one small tab in Case A, creating a large potential difference at that location. For Case B and the other cases, there are multiple locations where current can enter the cell reducing the potential difference at those locations.

Since the configuration with the small tabs located nearest the center post on both electrodes (Case A) proves to be the most likely to plate-out lithium, this configuration will be explored more closely as a “worst case” scenario. Then the results can be used as minimum standards when optimizing the battery design to avoid lithium plating.

Next various C-rates are explored to find which rate is close to but has not reached yet lithium plating after 1 second of charging. The purpose of this exploration is to find a C-rate that is right at the cusp of plating lithium and exploring how a lengthy

charging event can lead to plating at that particular C-rate. Seven C-rates are graphed in Figure 33 after 1 second of operation – C/5, C/4, C/3, C/2, C/1.5, C/1.25, and 1C. As expected, the lower the C-rate the less likely lithium plating will occur. The rate of C/1.25 will be used for the following lithium plating simulations as it is close to plating. Next, this C-rate will be run for a longer test to find at what point it will plate out lithium.

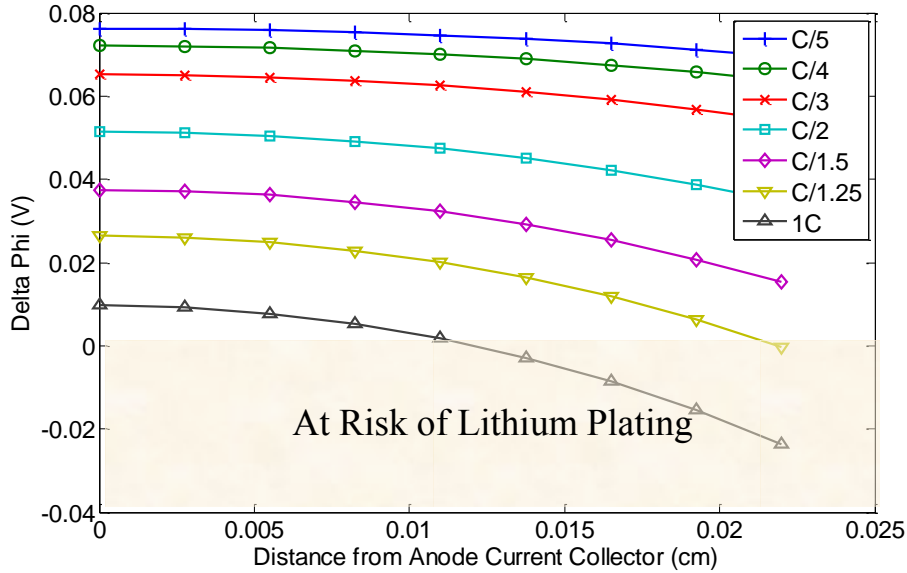


Figure 33: The faster the C-rate, the closer to lithium plating the cell becomes (delta phi less than zero). This data is taken after 1 second at the node closest to the tab.

The inner electrode pair which has both electrode tabs adjacent to the center post is explored over various times at a C-rate of C/1.25. Figure 34 shows electrode-separator interface for the same cell after 5, 15, and 30 seconds of charging at this C-rate. In the figure, regions that have the darkest color purple are areas in which lithium plating is likely ($\varphi_{\text{electrolyte}} - \varphi_{\text{electrode}} = \text{negative value}$). As can be seen, lithium plating becomes more likely as time progresses. It is most likely to originate at the tabs where all of the current is being driven into the cell.

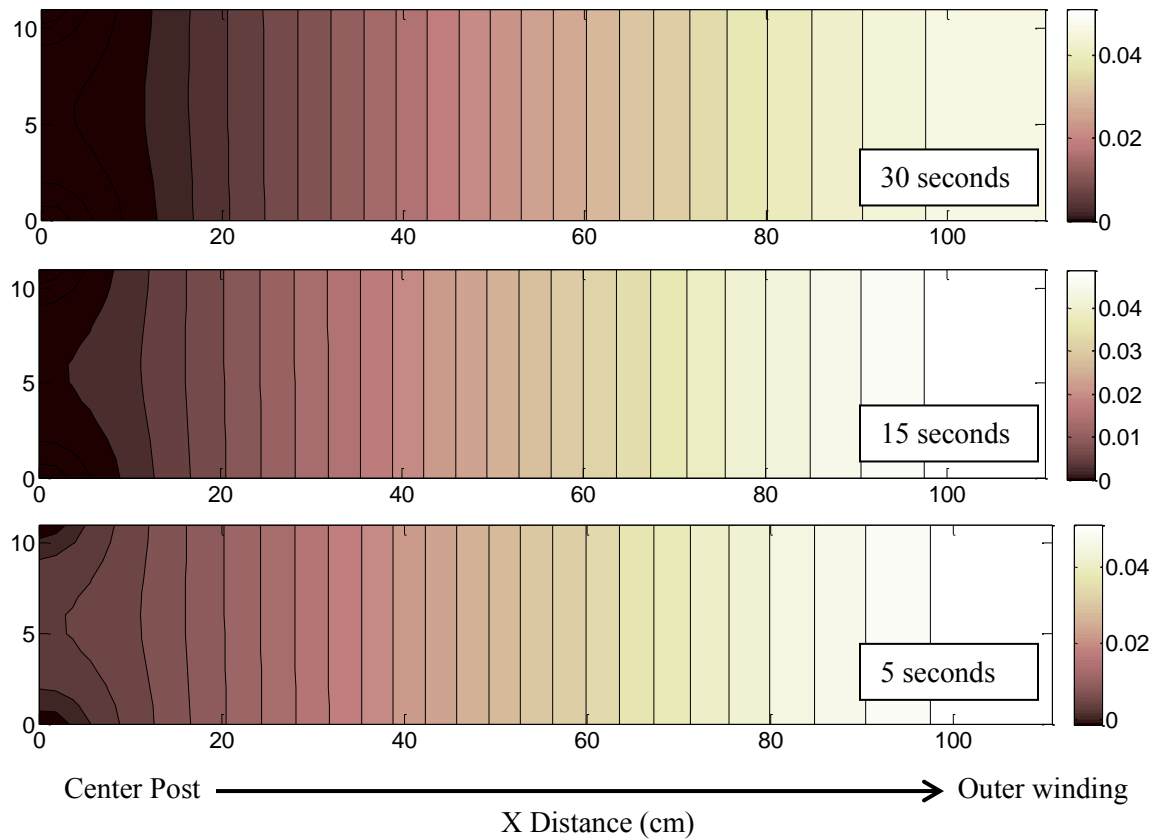


Figure 34: Plots of the inner electrode pair after 5, 15, and 30 seconds at a charging rate of $C/1.25$. Areas that are dark purple are at risk of lithium plating and also happen to be where the tabs are located.

To explore if discharging the battery just before a charging event has an effect on plating, another simulation is run where the battery is discharged at a $5C$ rate for 30 seconds followed by charging at a C -rate of $C/1.25$. This is useful because in a hybrid vehicle application, the battery will continually be discharged and charged in succession, for example when one has to brake after a period of acceleration. It is expected that a charging event preceded by a high rate discharge event will make lithium plating less likely. This occurs because during the discharge, the reaction on the negative electrode occurs at the electrode-separator interface causing the lithium concentration to be lowest at that point. Therefore the electrode potential will be greater than the electrolyte potential close to this interface as can be seen in Figure 35.

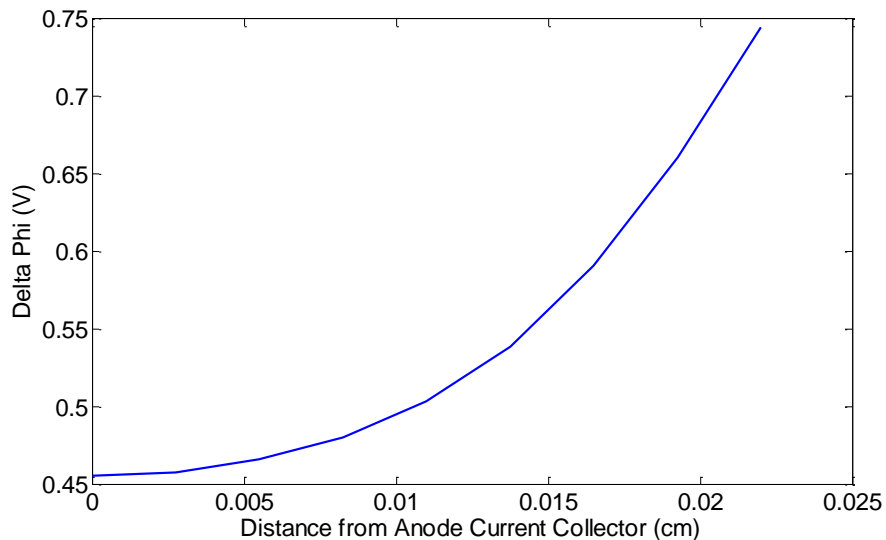


Figure 35: Inner electrode pair after 30 seconds of discharge of 5C. The negative electrode – separator interface (farthest point to the right on the line) is the region farthest from lithium plating risk. This graph is meant to show how it is impossible for lithium to plate onto the negative electrode during discharge, especially at the electrode – separator interface.

Since there is little lithium at this interface, upon charging lithium plating is much less likely than the previous case because there are plenty of lithium ions within the electrode. Figure 36 shows the inner electrode pair after 30 seconds of discharge and Figure 37 shows that same region after 5 second, 15 seconds and 30 seconds of charging at the rates described above.

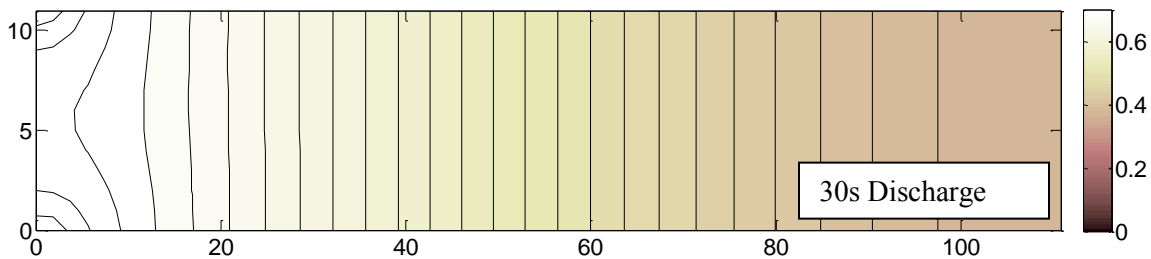


Figure 36: Plot of the inner electrode pair after 30 seconds at a discharging rate of 5C. No areas are at risk of lithium plating (since no dark purple regions exist).

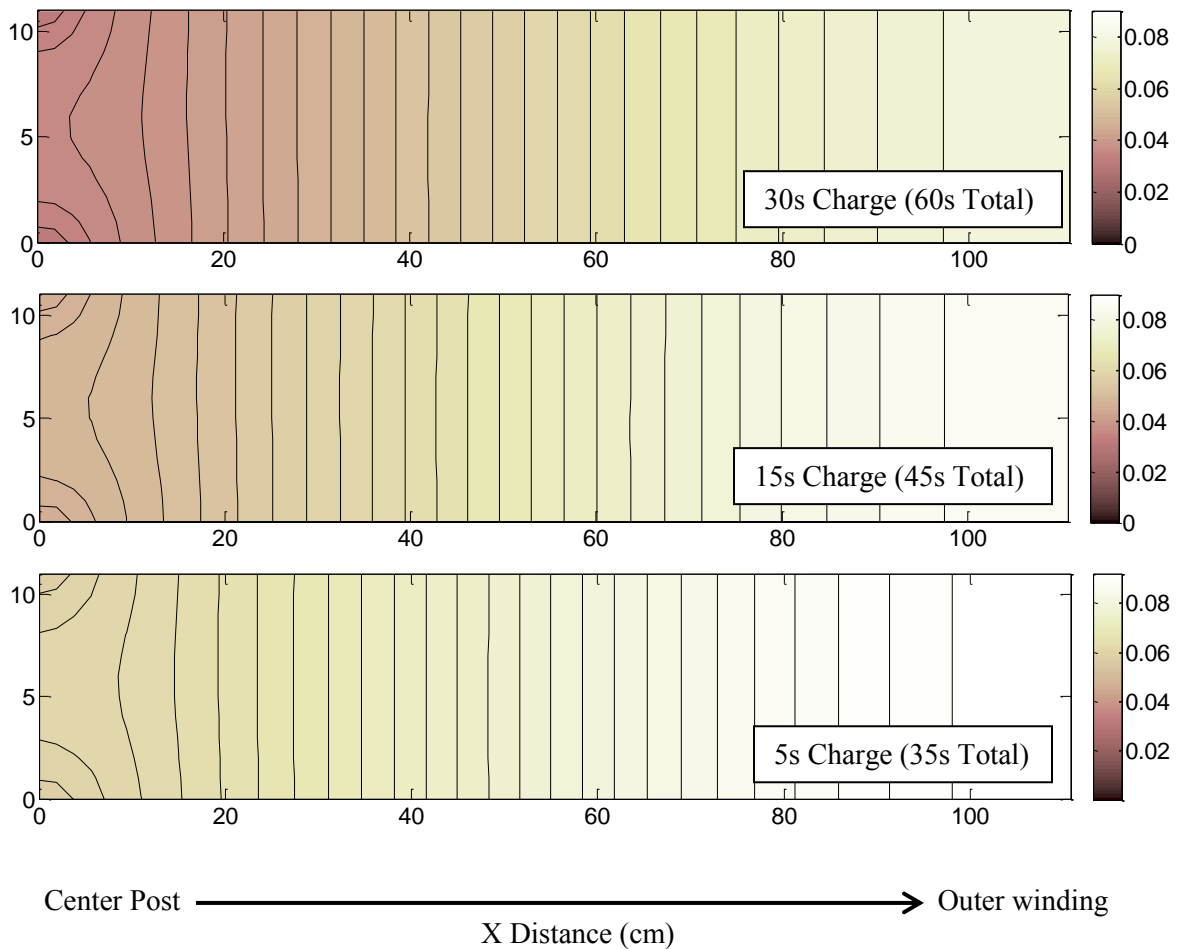


Figure 37: Plot of the inner electrode pairs at various times following the 30 seconds 5C discharge. Unlike Figure 34, there are no areas at risk of lithium plating (since no dark purple regions exist) after 30 seconds of C/1.25 charging.

Long periods of charging at a high rate will provide an increased risk of lithium plating around the tabs of the negative electrode, primarily at the electrode-separator interface. A preceding discharge event will decrease risk of lithium plating on the negative electrode as there is already a depletion of lithium. Therefore the charging rate and the state of the battery at the beginning of a charging event are important in predicting whether lithium will plate onto the negative electrode, consequently making the battery unsafe.

3.1.4.2 Spirally Wound Configuration – Li Plating

Similar to section 3.1.4.1, lithium plating will be explored in this section. When the local potential of the electrolyte is greater than the adjacent electrode ($\varphi_{\text{electrolyte}} - \varphi_{\text{electrode}} = \text{negative}$), there is potential for lithium to plate out onto the graphite.

First the number and size of tabs will be explored to see if they affect lithium plating. All six cases from section 3.1.1.2 of tab location are explored.

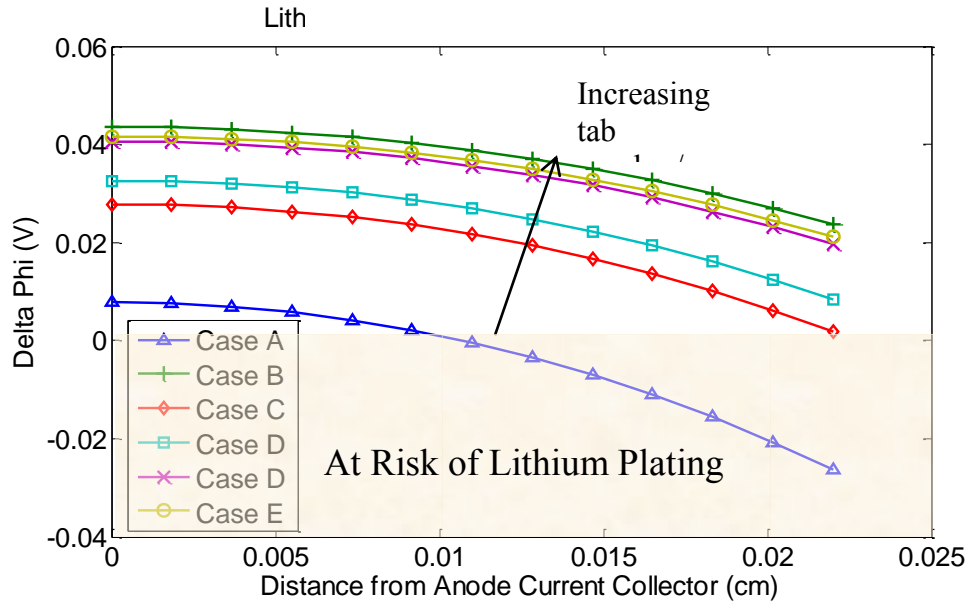


Figure 38: Tab location and size plays a role in lithium plating.

For this test, the base case prismatically wound battery was explored at a charging rate of 1C. The potential difference between electrolyte and negative electrode was taken after 1 second in the corner of the battery that is adjacent to the center post where there is a tab for all six cases. As can be seen in Figure 38, tab location and size does factor into whether lithium will plate out on the negative electrode during charging. As expected the battery where each electrode's single tab is along the first winding (Case A) is showing signs of plating immediately and the battery with tabs running the entire length of each electrode (Case B) is the least likely to have lithium plate out. It is interesting to see how much less likely of a risk of lithium there is for Case C, a case in which there is still just one tab per electrode, but they happen to be at opposite ends of their respective

electrodes. Not surprisingly, Cases D and E have a very similar likelihood (or lack thereof) of plating lithium onto the negative electrode.

Since Case A shows signs of plating lithium, this tab configuration will be explored more closely as a “worst case” scenario. The results can then be used as minimum standards when optimizing the battery design to avoid lithium plating.

Next, as was done in section 3.1.4.1, various C-rates are explored to find which rate is close to but has not reached yet lithium plating after 1 second of charging. Five C-rates are graphed in Figure 39 after 1 second of operation – C/5, C/3, C/1.5, C/1.25, and 1C. As expected, the lower the C-rate the less likely lithium plating will occur. The rate of C/1.25 will be used for the following lithium plating simulations as it is at risk of plating after only 1 second of charging. Next, this C-rate will be run for a longer test to find at what point it will plate out lithium.

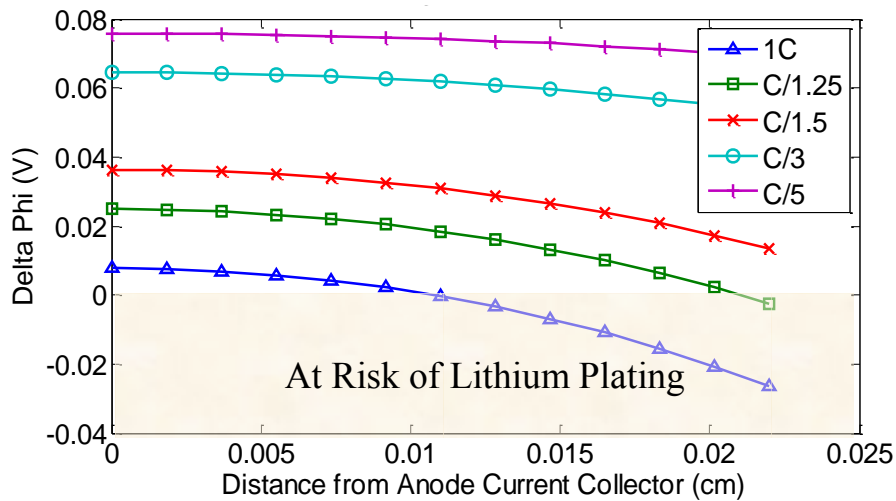


Figure 39: The faster the C-rate, the closer to lithium plating the cell becomes (delta phi less than zero). This data is taken after 1 second at the node closest to the tab.

The inner electrode pair is explored over various times at a C-rate of C/1.25. Figure 40 shows the same cell after 5, 15, and 30 seconds of charging at this C-rate. In the figure, regions that have the darkest color purple are areas in which lithium plating is likely ($\varphi_{\text{electrolyte}} - \varphi_{\text{electrode}} = \text{negative value}$). As can be seen, lithium plating becomes more likely as time progresses. It is most likely to originate at the tabs where all of the current is being driven into the cell.

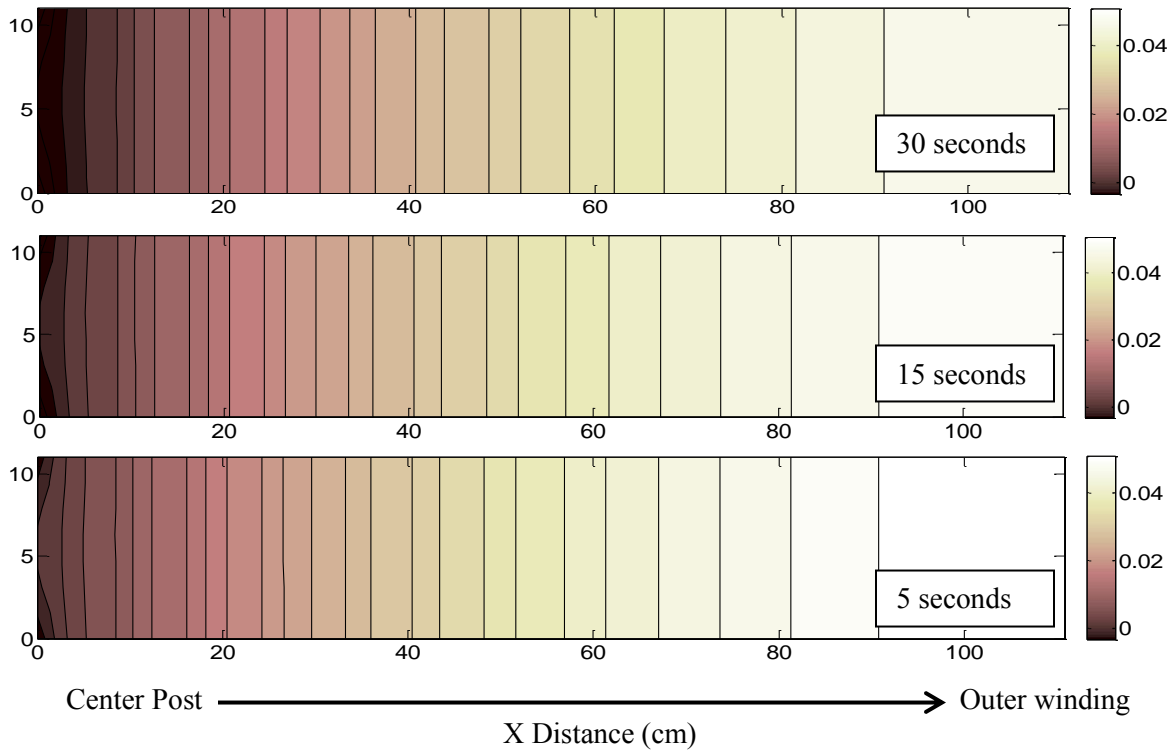


Figure 40: Plots of the inner electrode pair after 5, 15, and 30 seconds at a charging rate of $C/1.25$. Dark purple areas are at risk of Li plating and are where the tabs are located.

Following methodology of the spirally wound simulations, another simulation is run where the battery is discharged at a $5C$ rate for 30 seconds followed by charging at a C -rate of $C/1.25$. Like the spiral battery, it is expected that a charging event preceded by a high rate discharge event will make lithium plating less likely. Figure 41 shows the inner electrode pair at the electrode-separator interface after 30 seconds of discharge and Figure 42 shows that same region after 5 second, 15 seconds and 30 seconds of charging at the rates described above.

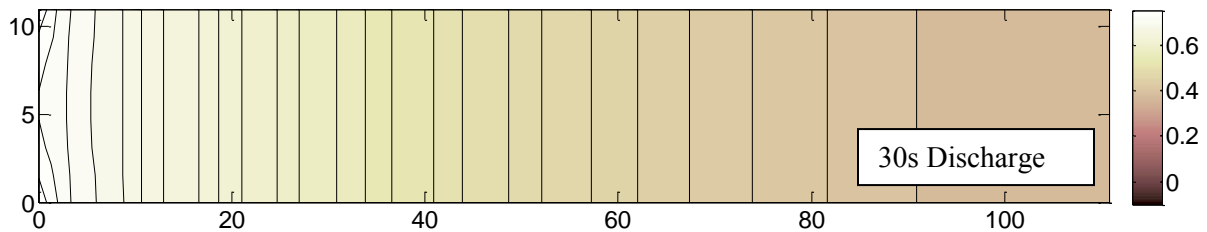


Figure 41: Plot of the inner electrode pair after 30 seconds at a discharging rate of $5C$. No areas are at risk of lithium plating (since no dark purple regions exist).

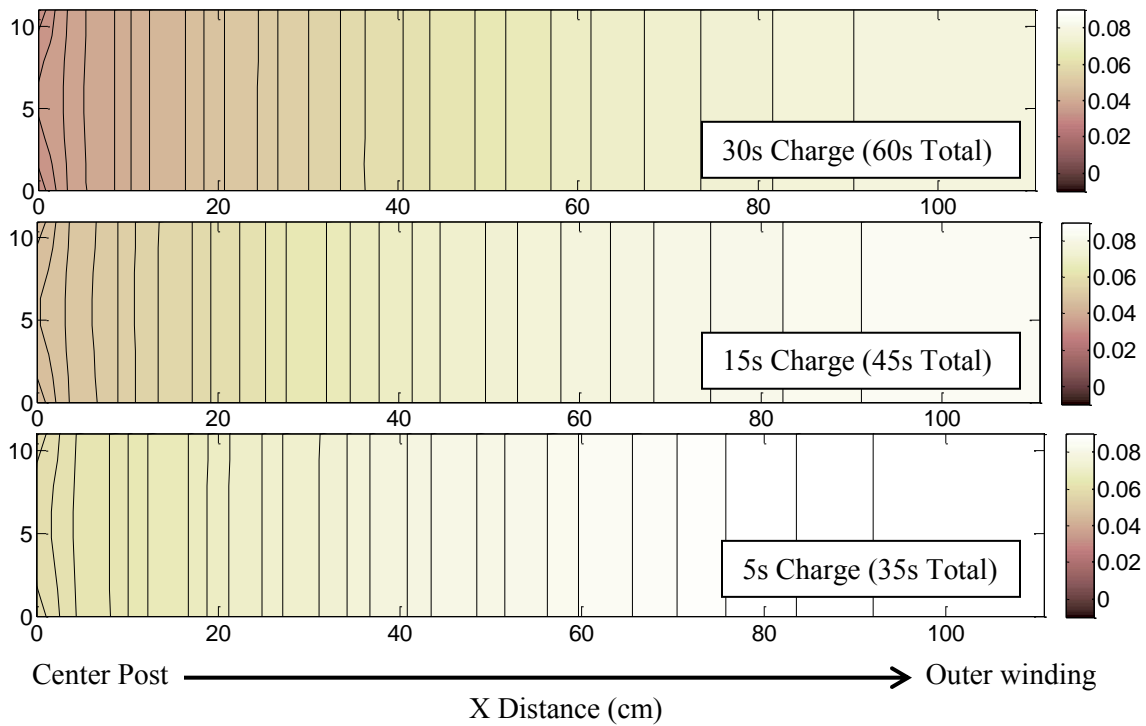


Figure 42: Plot of the inner electrode pairs at various times following the 30 seconds 5C discharge. Unlike Figure 40, there are no areas at risk of lithium plating (since no dark purple regions exist) after 30 seconds of C/1.25 charging.

Similar to the spirally wound configuration, for the prismatically wound configuration longer durations of charging at a high C-rate will make lithium plating more likely, especially around the tabs of the negative electrode within the electrode-separator interface. A discharge event that precedes the charging event will decrease risk of lithium plating on the negative electrode as there is already a depletion of lithium at that location. Therefore the charging rate and the state of the battery at the beginning of a charging event are critical to in predicting whether lithium will plate onto the negative electrode.

3.2 Configuration Comparison

In the following section each configuration – spiral and prismatically wound – will be compared. Specifically, configurations of similar sized batteries are compared for voltage versus capacity, energy density, temperature distribution, and current density distribution.

3.2.1 Voltage versus Capacity Comparison

For all of the results generated in the previous sections, the two battery configurations have the same cathode current collector areas, 1218.8 cm^2 , but different anode current collector areas. The spirally wound configuration has an anode area of 1280.3 cm^2 and the prismatically wound configuration has an anode area of 1393.1 cm^2 . The added anode area is due to the geometry of the prismatically wound battery. The outer winding of the battery is an anode-current collector-anode layer, and since there is added surface area due to the planar sections of the prismatically wound battery, there is extra material. Since the cathode area is the same for both configurations, the active area where electrochemical reactions can occur is the same for both configurations.

Though the active area is the same for both battery geometries, their voltage versus capacity discharge curves at various C-rates differs, especially at faster C-rates (Figure 43). The two configurations are “base case” with the only exception being that both have tabs running the entire length of each current collector. This was done to maximize current density uniformity and to eliminate any disparities due to tab size and location inherent to each configuration.

At fast C-rates, the spirally wound battery has a lower output voltage than the prismatically wound configuration. As the discharge current decreases, the two curves converge to toward the same value. These results may be a result of the differing number of layers between the two configurations and therefore the heat management. To have the same cathode active area, the spiral wound battery requires 20 layers whereas the prismatic wound battery only requires 8 layers. Therefore at high C-rates where heat is

generated quickly, the prismatic battery has the ability of transferring heat to the surroundings easier.

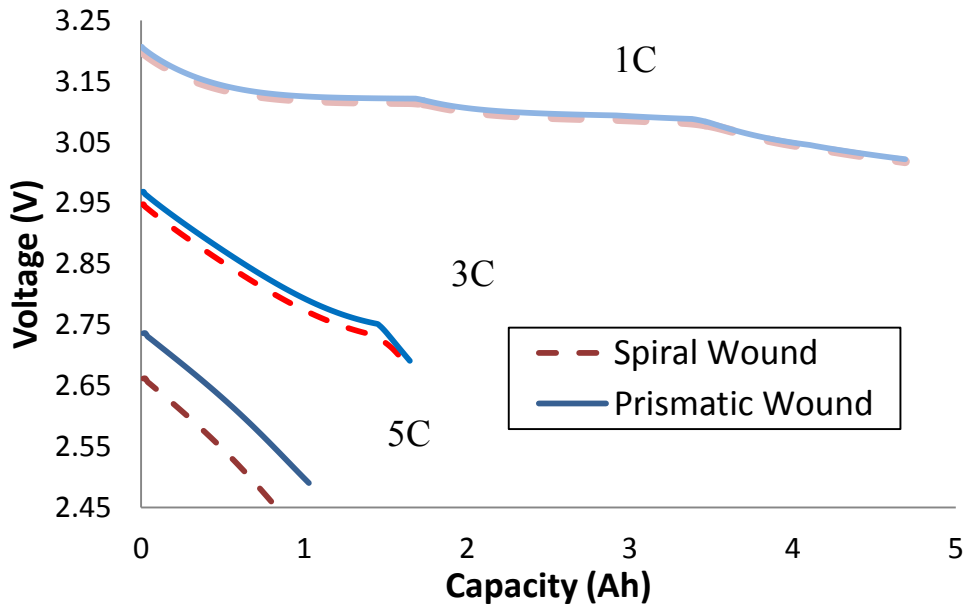


Figure 43: Comparison of discharge results for spirally wound (dashed lines) and prismatically wound (solid lines) at various C-rates.

3.2.2 Energy Density Comparison

For a proper energy density comparison, batteries that occupy the same *volume* will be compared. In this comparison two spirally wound batteries connected in parallel will be compared to a single prismatically wound battery. Both configuration comparisons will fit into the same rectangular volume. The advantage of the prismatically wound battery comes from its better use of space. When packing more than one spirally wound battery into a confined space, there will be unused space between each cylinder (Figure 44). If designed so that one battery is wide enough to fit the entire space, the prismatically wound battery uses some space that would otherwise be unused (Figure 45). For example, let's look at a prismatically wound battery that takes up the same space as two spirally wound batteries.

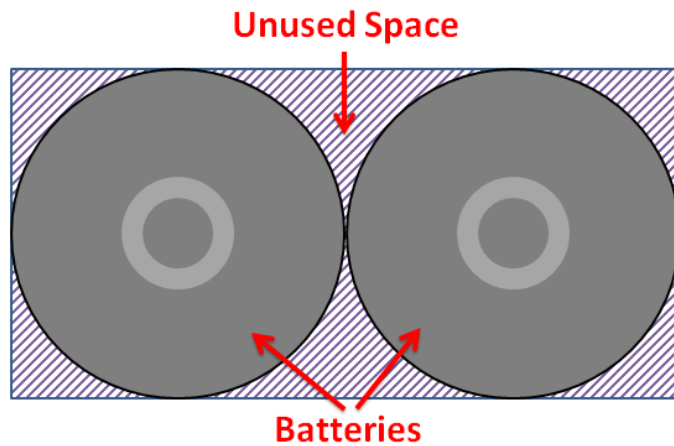


Figure 44: Multiple spirally wound batteries packed into a confined space

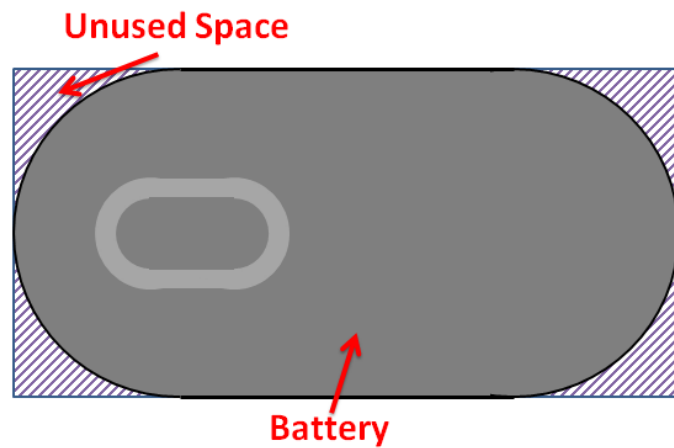


Figure 45: A single prismatically wound battery taking up the same volume as two spirally wound batteries

For the comparison, the base case batteries are not used. Instead, to save on computation time the spiral batteries are 5cm tall, have a center post radius of 0.25cm, and eight cathode windings (aka layers). The prismatic wound battery is 5cm tall, has a center post radius of 0.25cm, center post length of 1.5cm, and eight cathode windings as well; all other inputs are base case. The two spiral batteries take up the exact same volume as one prismatically wound battery in this study. The two spiral wound batteries each operate at 1.02A for a C-rate of 1C and the prismatically wound battery operates at 1.89A for a C-rate of 1C.

Since the prismatic wound battery has more active area than a single spirally wound battery, it operates at a higher current but has a lower overall power. The prismatically wound battery has a power of 6.06W at the start of the simulation. The two spiral batteries' each operate at 1.02A for a total current of 2.04A and total power output of 6.54W at the start of the simulation. Also, the prismatically wound battery also has a lower capacity than the two spirally wound batteries together.

Figure 44 shows a comparison of specific energy density (Wh/kg) versus capacity for the two configurations. Figure 46 shows a comparison of volumetric energy density (Wh/cm³) for the two configurations. Lastly, Figure 47 shows a comparison of specific energy density versus volumetric energy density for the two configurations.

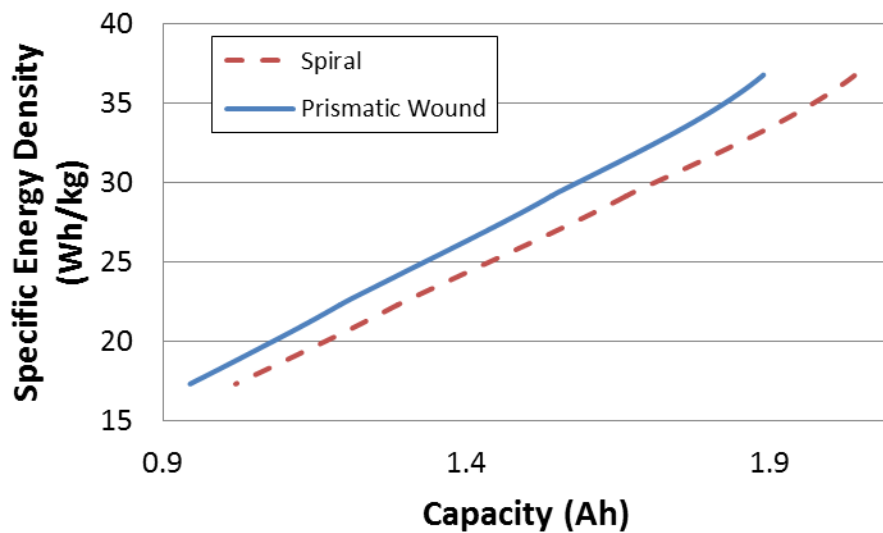


Figure 44: Specific energy densities of a spirally wound (dashed line) and prismatically wound battery (solid line).

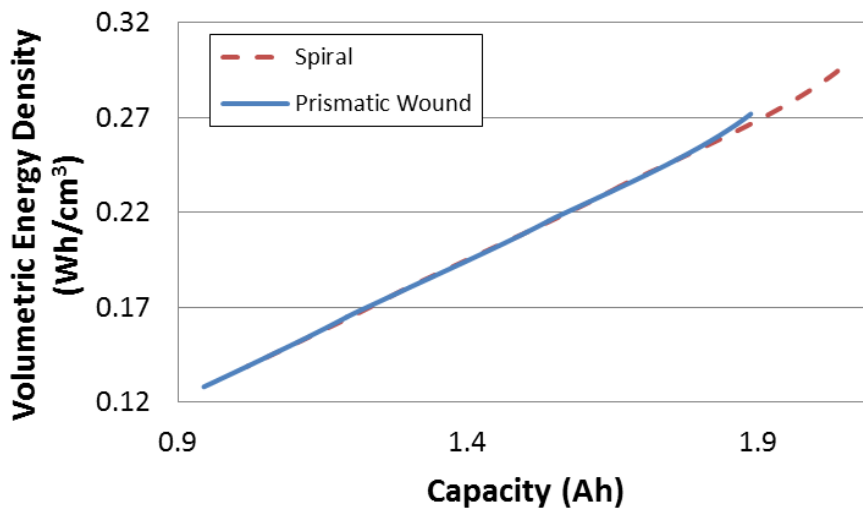


Figure 46: Volumetric energy densities of a spirally wound (dashed line) and prismatically wound battery (solid line).

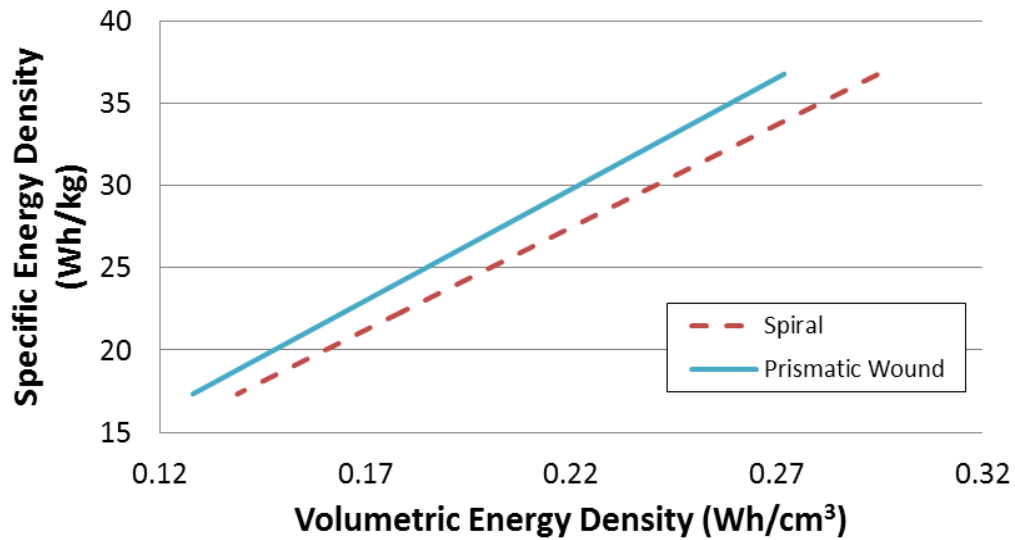


Figure 47: Specific energy density versus volumetric energy density of a spirally wound (dashed line) and prismatically wound battery (solid line).

The prismatically wound battery offers better specific energy density than the spirally wound batteries and about the same volumetric energy density. Though it has a lower capacitance than the two spiral batteries, the prismatic wound geometry has less material and therefore less weight. When considering both specific and volumetric energy densities (Figure 47), the prismatically wound battery offers a slight advantage.

3.2.3: Temperature and Current Density Distribution Comparison

For the two configurations explored, the cathode active area is the same for both spirally and prismatically wound batteries. Though the active area is the same, the geometry of the cell is not and therefore can potentially lead to a difference in current density uniformity and temperature distribution. A side by side comparison of both configurations with exactly the same materials, material thicknesses, thermal environment and discharge rates is shown as follows. Three discharge C-rates were drawn from each battery for 30 seconds – 5C, 1C and C/5 and the results compared.

Temperature range results can be found in Table 13. As would be expected, the absolute temperatures increase for both configurations as the C – rate is increased, but the spirally wound cell is both hotter and less uniform.

Configuration	C – Rate	Temperature Range (K)
Prismatic Wound	5C	302.1567 - 304.2460
Spiral Wound	5C	301.0912 - 307.1659
Prismatic Wound	1C	298.2083 - 298.3000
Spiral Wound	1C	298.1618 - 298.4250
Prismatic Wound	C/5	298.0162 - 298.0215
Spiral Wound	C/5	298.0134 - 298.0287

Table 13: Temperature range for both configurations at 3 different C-Rates.

A graphical display of the data above is shown in Figure 48. The configurations are compared at all three C-rates. The spirally wound cell is clearly hottest at the center post and the temperature gradient declines on each successive layer. The prismatically wound configuration is not the same; it is evident that there is a great deal of heat flow radially. The region with the tabs against the center post is the hottest but one can see that with each passing layer, the temperature rises for the regions adjacent to the tabs. The discrepancy may be because for the spirally wound battery, the tabs span roughly 60% of

the initial winding, so radial heat flux flows nearly uniformly outward. For the prismatically wound battery, the tabs are only along one segment of one side of the flat part of the battery and so there are regions of the battery that are far enough away that the radial heat flux from the tabs would not affect it greatly.

From these temperature study results, current density may be affected by battery geometry as well. Both battery configurations are simulated at the same three discharge C-rates. The inner electrode pair delta current densities are generated where delta current density equals local nodal current density minus average current density throughout the cell. Results are displayed in Table 14 and Figure 49.

While the temperature distributions were relatively different between each configuration, the current density uniformity happens to be fairly similar. The range of delta current densities is displayed in Table 14. A visual inspection of Figure 49 reveals that, as expected both battery configurations are more uniform with smaller C-rates. Upon closer examination, the prismatically wound battery is slightly more uniform. This can be attributed to the more uniform temperatures distribution in the prismatic wound configuration.

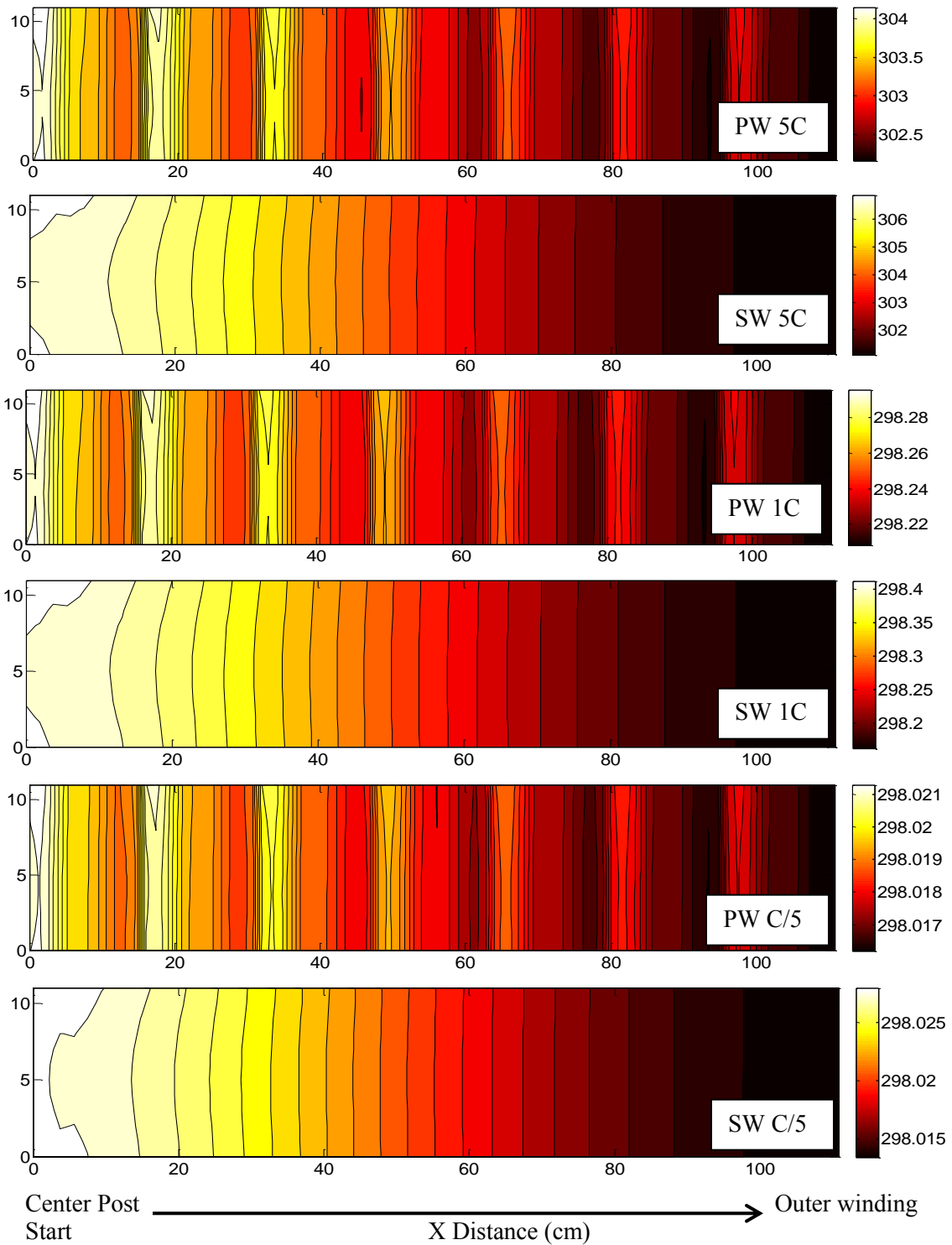


Figure 48: Temp comparison of spiral and prismatic wound configurations at different C-rates.

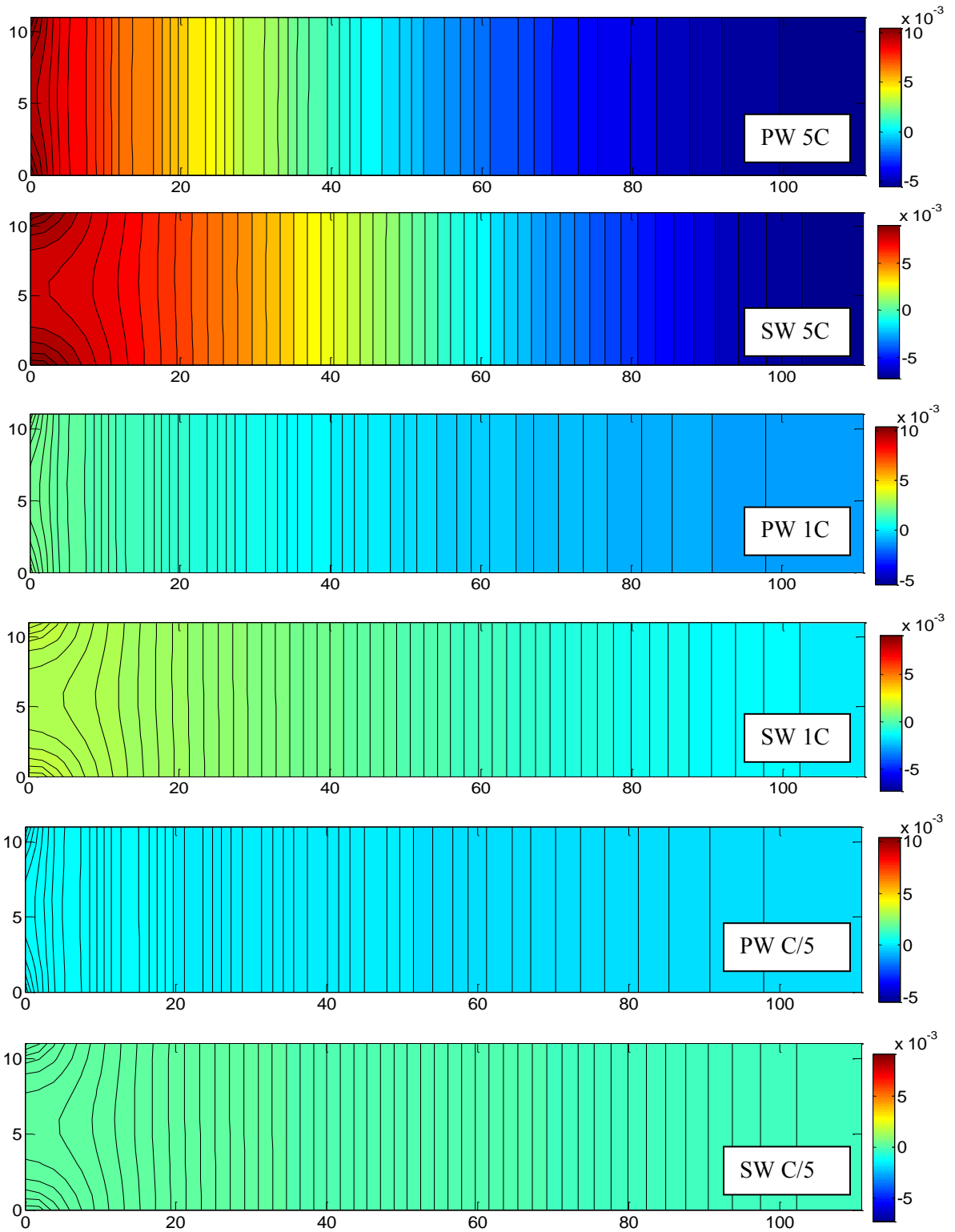


Figure 49: Current density comparison of spiral and prismatic wound configurations at different C-rates.

Configuration	C – Rate	Delta Current Density Range (A/cm²)
Prismatic Wound	5C	-0.0055 - 0.0108
Spiral Wound	5C	-0.0073 - 0.0094
Prismatic Wound	1C	-0.0011 - 0.0024
Spiral Wound	1C	-0.0014 - 0.0020
Prismatic Wound	C/5	-2.2502e-04 - 4.7872e-04
Spiral Wound	C/5	-2.8845e-04 - 3.9527e-04

Table 14: Current density range for both configurations at 3 different C-Rates.

3.3 Model Limitations

While this model has a wide breadth of uses and applications, it still has some limitations. The center post and can that contains the battery are largely neglected for weight, volume and thermal conduction. Also the electrochemical model treats each individual anode – cathode pairing as having the same cross-sectional area, when in reality whichever electrode is farther radially from the center post will have a slightly larger area than the interior electrode. Lastly, the software itself used has limitations for number of time steps, overall time, number of mesh points, and number of nodes. If these factors are too numerous the software will crash, even on a high performance computer network. That is why a discretization error check was conducted and can be found in Appendix C.

Appendix A: Model Input Data

Below are tables and sections that show where all user inputs are generated from. In most cases the values are drawn from literature on lithium iron phosphate batteries, but some data is taken directly from A123 datasheets or chosen by the user.

Unless otherwise specified, the inputs from below are used to construct “base case” configurations for both spirally and prismatically wound batteries.

A.1 User Inputs:

Property	Value	Reference
Total Time (<i>s</i>)	Varies	User input
Number of Time Steps per Second	1	Discretization Error Check
Number of Anode Mesh Spaces in Z Direction	8	Discretization Error Check
Number of Cathode Mesh Spaces in Z Direction	8	Discretization Error Check
Number of Separator Mesh Spaces in Z Direction	4	Discretization Error Check
Nodes per Winding (<i>spirally wound</i>)	40	Calculated from [29]
Nodes per Winding (<i>prismatically wound</i>)	84	Deduced from [29]
Control Method	Voltage or Current	User input
C-Rate	See Eqn. [A.1]	[22]
Initial Temperature Battery (<i>Kelvin</i>)	298	Design parameter
Ambient Temperature (<i>Kelvin</i>) (constant throughout simulation)	298	Design parameter

C-Rate Calculation:

$$\text{Volume Active Material} = \frac{\text{Electrode Volume}}{\text{Volume}} * \text{Number of Cells} * (1 - \text{Porosity}) * \text{Fraction of Active Electrode}$$

$$\text{Moles of Lithium in Electrode} = \frac{\text{Volume Active Material}}{\text{Material}} * \text{Lithium Concentration per Volume}$$

$$\text{Total Discharge Time} = \frac{\text{Moles of Lithium in Electrode}}{\text{Current} / 96487}$$

$$C - Rate = \frac{3600}{Total\ Discharge\ Time}$$

Equations from [22]

[A.1]

A.2 Battery Dimensions:

Property	Value	Reference
Anode Thickness (<i>cm</i>)	0.01	[22]
Cathode Thickness (<i>cm</i>)	0.015	[22]
Separator Thickness (<i>cm</i>)	0.003	[22]
Anode Current Collector Thickness (<i>cm</i>)	0.00124	Deduced from [29]
Cathode Current Collector Thickness (<i>cm</i>)	0.002	Deduced from [22]
Battery Height in Y direction (<i>cm</i>)	11	Deduced from [29]
Center Post Radius (<i>cm</i>) (<i>spiral and prismatic wound</i>)	0.25	Deduced from [29]
Center Post Length (<i>cm</i>) (<i>prismatic wound</i>)	6.447	Deduced from [29]
Spiral Wound Battery Outer Radius (<i>cm</i>)	1.6	Deduced from [29]
Number of Cells	2	Design parameter
Inner-Most Current Collector Plate	Anode or Cathode	Design parameter

A.3 Electrochemical Equations:

Property	Value	Reference
Initial Solution Concentration (<i>moles/cm³</i>)	0.001	[22]
Separator Porosity (<i>0->1, fraction electrolyte</i>)	0.6	[22]
For Butler-Volmer: α_a and α_c	0.5	[33]
Exchange Current Density: δ	0.5	[22]
Exchange Current Density: γ	0.5	[22]
Exchange Current Density: c_{ref} (<i>moles/cm³</i>)	0.001	[22]
Exchange Current Density: cs_{ref} (<i>specified as fraction of cs_{max}</i>)	0.5	[22]
$(1 - d\ln c/d\ln c) f(c, temp)$	1	[22]
$(1 + d\ln f/d\ln c) f(c, temp)$	See Eqn. [A.6]	[37]
Electrolyte Conductivity (<i>S/cm</i>) $f(c, temp, Porosity)$	See Eqn. [A.7]	[37]

Electrolyte Diffusion (cm^2/s) $f(c, temp, Porosity)$	See Eqn. [A.8]	[37]
Transference Number Cation $f(c, temp)$	0.4	[37]
Density of Separator (g/cm^3)	0.9	[30]
Density of Electrolyte (g/cm^3)	1.2	[30]
For LiC₆ Electrode:		
Porosity ($0 < \rightarrow 1$, fraction electrolyte)	0.4	[29]
Density (g/cm^3)	2.27	[30]
Initial Electrode Lithium Concentration, fraction of maximum ($0 < \rightarrow 1$)	0.7	[29]
Fraction of Solid Material in Active Electrode ($0 < \rightarrow 1$)	0.88	Calculated from [30]
Max Lithium Concentration in Active Electrode ($moles/cm^3$)	0.0287	Calculated from [30]
Lithium Solid Diffusion Coefficient in electrode (cm^2/sec)	9.00E-10	[31]
Electrode Particle Radius (cm)	0.011	[3]
Active Electrode Interfacial Surface Area Per Unit Volume (cm^2/cm^3)	1.64E+04	Calculated from [A.1]
Copper Current Collector Conductivity (S/cm) $f(temp)$	See Eqn. [A.9]	[38]
Density of Copper (g/cm^3)	8.9	[30]
Electrode Reference Exchange Current Density (A/cm^2) $f(temp)$	See Eqn. [A.4]	[34]
Electrode Film Resistance (Ohm/cm^2) $f(temp)$	230	[30]
Electrode Open Circuit Voltage (V) $f(cs, csmax, temp)$	See Eqns. [A.10, A.11, A.12, A.13]	[22] and [38]
Electrode Solid Phase Conductivity (S/cm) $f(temp, Porosity)$	1	[41]
For LiFePO₄ Electrode		
Porosity ($0 < \rightarrow 1$, fraction electrolyte)	0.4	[22]
Density (g/cm^3)	3.6	[30]
Initial Electrode Lithium Concentration, fraction of maximum ($0 < \rightarrow 1$)	0.15	[22]

Fraction of Solid Material in Active Electrode ($0 < \rightarrow 1$)	0.7	Calculated from [30]
Max Lithium Concentration in Active Electrode ($moles/cm^3$)	0.0228	Calculated from [30]
Lithium Solid Diffusion Coefficient in electrode (cm^2/sec)	8.00E-14	[32]
Electrode Particle Radius (cm)	0.000052	[30]
Active Electrode Interfacial Surface Area Per Unit Volume (cm^2/cm^3)	3.46E+05	Calculated from [A.1]
Aluminum Current Collector Conductivity (S/cm) $f(temp)$	See Eqn. [A.10]	[38]
Density of Aluminum (g/cm^3)	2.7	[30]
Electrode Reference Exchange Current Density (A/cm^2) $f(temp)$	See Eqn. [A.5]	[35] and [36]
Electrode Film Resistance (Ohm/cm^2) $f(temp)$	0	[22]
Electrode Open Circuit Voltage (V) $f(cs, cs_{max}, temp)$	See Eqns. [A.14, A.15, A.16]	[22] and [40]
Electrode Solid Phase Conductivity (S/cm) $f(temp, Porosity)$	5.00E-03	[32]

Active Interfacial Surface Area per Unit Volume:

$$a = \frac{3\varepsilon}{r} \quad [A.2]$$

Equation from [22]

Exchange Current Density:

$$i_o = i_{o,ref} \left(\frac{c}{c_{ref}} \right)^{0.5} \left(\frac{cs}{cs_{ref}} \right)^{0.5} \quad [A.3]$$

Equation from [28].

LiC₆ Electrode:

$$i_{o,ref} = 20e^{\left(\frac{-30,000}{RT} \right)} \quad [A.4]$$

Equation derived from [34]

LiFePO₄ Electrode:

$$i_{o,ref} = (1.34 * 10^{-3}) e^{\left(\frac{-15,000}{RT} \right)} \quad [A.5]$$

Equation derived from [35] and [36]

Electrolyte Property Equations:

Thermodynamic Factor:

$$\left(1 + \frac{d \ln f}{d \ln c}\right) = \frac{0.601 - 0.24C^{0.5} + 0.982(1 - 0.0052(T - 298))C^{1.5}}{1 - t_+} \quad [\text{A.6}]$$

Equation from [37]

Electrolyte Conductivity:

$$\kappa = C(-10.5 + 0.074T - 6.96 * 10^{-5}T^2 + 0.668C - 0.0178C * T + 2.8 * 10^{-5}C * T + 0.494C^2 - 8.86 * 10^{-4}C * T^2)^2 \quad [\text{A.7}]$$

Equation from [37]

Li+ Diffusion Coefficient in Electrolyte:

$$D = 10^{-0.22C - 4.43 - \frac{54}{T - 229 + 5C}} \quad [\text{A.8}]$$

Equation from [37]

Current Collector Conductivities:

Copper Anode Current Collector Conductivity:

$$\sigma_{Cu} = -0.04889T^3 + 54.65T^2 - 21800T + 3.52 * 10^6 \quad [\text{A.9}]$$

Equation from [38]

Aluminum Cathode Current Collector Conductivity:

$$\sigma_{Al} = -0.0325T^3 + 37.07T^2 - 15000T + 2.408 * 10^6 \quad [\text{A.10}]$$

Equation from [38]

Open Circuit Voltage:

$$U = U_{ref} + (T - T_{ref}) * \frac{dU}{dT} \quad [\text{A.11}]$$

Li_xC₆ Electrode:

x is the fraction of lithium in electrode

For x > 0.95

$$U_{ref} = -162.54x^3 + 449.21x^2 - 413.89x + 127.22 \quad [A.12]$$

For 0.90 < x < 0.95

$$U_{ref} = (-1.6525x^4 - 158.8523x^3 + 446.4208x^2 - 413.1349x + 127.28)/2 \quad [A.13]$$

For 0.2032 < x < 0.90

$$U_{ref} = -1.6525x^4 + 3.6877x^3 - 2.7892x^2 + 0.7551x + 0.0629 \quad [A.14]$$

For x < 0.2032

$$U_{ref} = 1683.3x^4 - 1148.7x^3 + 286.93x^2 - 31.745x + 1.5005 \quad [A.15]$$

Equations derived from [22] and [38]

Li_xFePO₄ Electrode:

x is the fraction of lithium in electrode

For x > 0.892

$$U_{ref} = -5.76 * 10^3 x^4 + 2.07 * 10^4 x^3 - 2.79 * 10^4 x^2 + 1.67 * 10^4 x - 3.77 * 10^3 \quad [A.16]$$

For 0.048 < x < 0.892

$$U_{ref} = 3.42 \quad [A.17]$$

For x < 0.048

$$U_{ref} = 3.02 * 10^5 x^4 - 4.34 * 10^3 x^3 + 2.46 * 10^3 x^2 + 69.7x + 4.3 \quad [A.18]$$

Equation derived from [22] and [40]

A.4 Thermal Equations:

Property	Value	Reference
Volumetric Heat Capacity (J/cm³ K)		
Copper Current Collector <i>f(temp)</i>	3.44	[38]
LiC ₆ Electrode <i>f(temp)</i>	1.9	[42]
Separator <i>f(temp)</i>	2	[42]
LiFePO ₄ Electrode <i>f(temp)</i>	2	[22]

Aluminum Current Collector $f(temp)$	2.42	[38]
Thermal Conductivity (W/cm K)		
Copper Current Collector $f(temp)$	4.01	[38]
LiC ₆ Electrode $f(temp)$	0.01	[42]
Separator $f(temp)$	0.005	[42]
LiFePO ₄ Electrode $f(temp)$	0.01	[22]
Aluminum Current Collector $f(temp)$	2.37	[38]
Other		
LiC ₆ Entropy $f(cs, csmax, temp)$	See Eqn. [A.19]	[43]
LiFePO ₄ Entropy $f(cs, csmax, temp)$	See Eqn. [A.20]	[44]
Convection ($W/cm^2 K$)	0.1	[22]

Electrode Entropy:

Li_xC₆ Electrode:

x is fraction of lithium in electrode

$$\frac{dU}{dT} = 344.1347148 * \frac{\exp(-32.9633287x + 8.316711484)}{1 + 749.0756003 * \exp(-34.7909964 + 8.887143624)} - 0.8520278805x + 0.36229929x^2 + 0.269800169$$

Equation from [43]

[A.19]

Li_xFePO₄ Electrode:

x is fraction of lithium in electrode

$$\frac{dU}{dT} = -0.35376x^8 + 1.3902x^7 - 2.2585x^6 + 1.9635x^5 - 0.98716x^4 + 0.28857x^3 - 0.046272x^2 + 0.0032158x - 1.9186 * 10^{-5}$$

Equation from [44]

[A.20]

A.5 List of Symbols:

Symbol	Meaning
a	Active Interfacial Surface Area per Unit Volume
ε	Porosity
α_a	Anodic charge transfer coefficient
α_c	Cathodic charge transfer coefficient
R	Gas Constant, 8.314
T	Temperature (Kelvin unless noted otherwise)
C	Lithium ion concentration in Molarity
t_+	Li+ transference number
i_o	Exchange current density
σ	Conductivity
U	Open circuit potential

APPENDIX B: ELECTROCHEMICAL AND THERMAL MODEL THEORY

B.1 Electrochemical Model

The electrochemical model employed in this thesis is based upon the lithium ion porous electrode theory dualfoil model developed by Thomas, Newman, and Darling. The article, specifically named “Mathematical Modeling of Lithium Batteries”, describes that each porous electrode is treated as a collection of spherical particles. The position and shape of the pores are not specified; instead these properties are averaged over a volume that is small enough with respect to the overall dimensions of the electrode but large enough with respect to the size of the pores. The electrode and electrolyte phases are coupled via mass transfer and reaction rate identities. Lastly, all phases are considered electrically neutral [28].

B.1.1 Potential in Solution

The equation related to gradient of potential in the solution (electrolyte), ϕ_2 , is as follows:

$$\nabla\phi_2 = \frac{-i_2}{K} + \frac{2RT}{F} * (1 - t_+^0) * \left(1 + \frac{d\ln f_{\pm}}{d\ln c}\right) * \nabla\ln c \quad [\text{B.1}]$$

Since only potential differences are measurable within a cell, ϕ_2 has an arbitrary datum. For this model the datum used at the positive electrode – current collector interface is $\phi_2 = 0$.

B.1.2 Potential in Solid

The equation used for potential in the solid (electrode), ϕ_1 , can be derived from Ohm’s law:

$$-\sigma\nabla\phi_2 = I - i_2 \quad [\text{B.2}]$$

Here, the term on the right side of equation B.2 represents current in the electrode phase, where I is the total current entering the 1D electrochemical model. Also σ is the solid phase conductivity. Boundary conditions for this equation are the $i_2 = I$ at the negative

electrode – separator interface and $i_2 = 0$ at the positive electrode – current collector interface.

B.1.3 Transport in Solution – Concentrated Solution Theory

This model follows concentrated solution theory, which includes interactions among all species present in solution (whereas dilute solution theory assumes ions in solution only interact with the solvent and not each other). Since only Li^+ reacts in lithium ion batteries, the mass transport equations are simplified by focusing only on mass balance for the *anion*. By electroneutrality, mass balance for the anion will be the same as that of the cation. During operation, Li^+ ions will enter the electrolyte from one electrode and diffuse across the cell to the other electrode; this creates a concentration gradient across the cell. The equation related to mass transport and concentration of Li^+ in solution, c , is as follows:

$$\varepsilon \frac{\partial c}{\partial t} = \nabla \cdot \varepsilon * D \left(1 - \frac{d \ln c_0}{d \ln c} \right) * \nabla C + \frac{t_-^0 \nabla \cdot i_2 + i_2 \cdot \nabla t_-^0}{z_+ v_+ F} - \nabla \cdot c v_0 + a j_- \quad [\text{B.3}]$$

Since convection in the electrolyte is negligible, $\nabla \cdot c v_0 = 0$, and also $j_- = 0$ in the absence of side reactions, so the overall equation can be simplified. The lone boundary condition is that $\frac{\partial c}{\partial x} = 0$ at $x = 0$. It should be noted that averaging introduces some degree of error in calculating the potential and Li^+ concentration at the pore wall. To compensate for this, mass transfer coefficients have been introduced.

B.1.4 Transport in Solid / Duhamel's Superposition Integral

In most lithium ion batteries, the active material consists of mobile Li^+ cations, mobile electrons and an immobile host matrix. The general equation related to Li^+ concentration within the solid, c_s , is as follows:

$$\frac{\partial c_s}{\partial t} = \nabla \cdot D_s \left(1 - \frac{d \ln c_0}{d \ln c_s} \right) * \nabla C_s + \frac{i_1 \cdot \nabla t_-^0}{z_+ v_+ F} - \nabla \cdot c_s v_0 \quad [\text{B.4}]$$

Since it is an ionic insertion battery, there are no phase changes or new compounds generated so it is simple to model. Also the active material is a good conductor, and if the

volume change in the solid is treated as negligible, then equation B.4 can be reduced using Duhamel's Superposition Integral to:

$$\frac{\partial c_s}{\partial t} = \frac{1}{r^2} \frac{\partial}{\partial r} (D_s r^2 \frac{\partial c_s}{\partial r}) \quad [\text{B.5}]$$

Boundary conditions are that at $r = 0$ $\frac{\partial c_s}{\partial r} = 0$, and at $r = R$ $-D_s \frac{\partial c_s}{\partial r} = j_{Li+,f}$. Here, j is the flux of lithium out of the electrode due to the electrochemical reaction and D_s is the diffusion coefficient of the ion.

B.1.5 Reaction Rate

The equation used for reaction rate, i_n , is the Butler-Volmer equation. It calculates the rate of reaction per interfacial area based on potentials in the solid and solution and open circuit potential.

$$i_n = i_0 \left[\exp \left(\frac{\alpha_a F (\phi_1 - \phi_2 - U)}{RT} \right) - \exp \left(\frac{\alpha_c F (\phi_1 - \phi_2 - U)}{RT} \right) \right] \quad [\text{B.6}]$$

Here, U is the open circuit potential of the solid material evaluated at the surface of the solid with respect to a hypothetical Li reference electrode in solution just outside of the diffuse part of the double layer. Here, α_a and α_c are the fractions of the applied potential which favor respectively the anodic and cathodic directions of the overall reaction. Though reaction mechanisms at electrode-electrolyte interfaces are not completely understood, the rapid kinetics in lithium ion batteries reduces the importance of the exact reaction mechanism when modeling. Therefore both α_a and α_c are assumed to equal 0.5. The exchange current density, i_0 , is the reference current for the cell based on reaction kinetics.

During operation of a lithium ion battery, a passivated layer, called the solid-electrolyte interphase (SEI), forms on the surface of the negative electrode due to reaction with the electrolyte. It adds kinetic resistance to the cell and alters equation B.6 to look like:

$$i_n = i_0 \left[\exp \left(\frac{\alpha_a F (\phi_1 - \phi_2 - U - j_n F R_{film})}{RT} \right) - \exp \left(\frac{\alpha_c F (\phi_1 - \phi_2 - U - j_n F R_{film})}{RT} \right) \right] \quad [\text{B.7}]$$

B.1.6 Current Balance

By electroneutrality, a current balance relates the divergence of the current to the net pore-wall ion flux due to the reaction. The equation relating reaction rate to current in solution, i_2 , is as follows:

$$ai_n = \nabla \cdot i_2 \quad [\text{B.8}]$$

B.1.7 Other Considerations

Double layer adsorption is negligible in most cases due to the small magnitude of Li^+ concentration change. If the magnitude reaches a critical size, then slight changes need to be made to the mass balance equation for the electrolyte.

Various side reactions can occur in a lithium ion battery including electrolyte reduction/oxidation, lithium deposition, redox shuttles for overcharge protection, corrosion of current collectors, self-discharge, conversion of active material to inactive phases, and other degradation mechanisms. Side reactions can introduce error is not taken into account properly. In this thesis, lithium deposition (aka plating) is explored in depth, where the major downside to this side reaction is that it reduces the amount of cyclable lithium and it also clogs pores.

B.1.8 List of Symbols

a	active interfacial area per unit volume
α	transfer coefficients
c	salt concentration in electrolyte
c_s	concentration of lithium in the solid
D	diffusion coefficient in solution
D_s	diffusion coefficient in solid
ε	porosity (volume fraction of electrolyte)
F	Faraday's constant
f_{\pm}	mean molar activity coefficient of the electrolyte

h	mesh space distance
i_2	current in solution
i_n	current per unit interfacial area
i_o	exchange current density
j	total flux due to electrochemical reaction
K	solution phase conductivity
N	flux of lithium ions
Φ_1	solid phase potential
Φ_2	solution phase potential
T	temperature
t_+	cation transference number
U	open circuit potential
v_0	electrolyte velocity

B.2 Thermal Model

The thermal model uses heat generation data to determine temperature distributions throughout the cell. The calculated temperatures are used as inputs to the electrochemical model on the next time step. The thermal model accounts for heat capacity and heat transfer within the battery and to the surroundings. Temperature is considered constant within the five layers of the battery (anode current collector, anode, separator, cathode, cathode current collector), but it varies within the current collectors and between the cells of the battery.

B.2.1 Heat Generation

Heat is generated within the cell from the electrochemical reaction and due to resistance. Electrochemical heat generation can be calculated from:

$$\dot{Q} = I(U - V - T \frac{\partial U}{\partial T}) \quad [\text{B.9}]$$

Here, \dot{Q} is the heat generation rate, I is the total current, U is the open circuit potential, V is total voltage across the cell, and T is temperature. This equation accounts for

irreversible heat generation due to cell resistance and reversible heat generation due to entropy of the electrochemical reaction. Heat of mixing is neglected because of simplifications used in section B.1.4.

The equation for resistive heating in the current collectors is:

$$\dot{Q} = 0.5 \left[\frac{(V_{x,y} - V_{x-1,y})^2}{R} + \frac{(V_{x,y} - V_{x+1,y})^2}{R} + \frac{(V_{x,y} - V_{x,y-1})^2}{R} + \frac{(V_{x,y} - V_{x,y+1})^2}{R} \right] \quad [\text{B.10}]$$

B.2.2 Heat Transfer

Heat transfer between nodes in the battery is governed by:

$$\rho C_p \frac{\partial T}{\partial t} = k_x \frac{\partial T^2}{\partial x^2} + k_y \frac{\partial T^2}{\partial y^2} + k_z \frac{\partial T^2}{\partial z^2} \quad [\text{B.11}]$$

In the plane of the current collector $k_x = k_y = \Sigma k_i f_i$ where k_i is the conductivity of each layer and f_i is the volume fraction of each layer. Between the anode and cathode $1/k_z = \Sigma f_i/k_i$.

Heat transfer to the surroundings occurs in three ways – through convection, radiation, and conduction. The three equations are as follows:

$$\dot{q}_{convection} = h(T_{node} - T_{amb}) \quad [\text{B.12}]$$

where h is user defined

$$\dot{q}_{radiation} = \sigma \varepsilon (T_{node}^4 - T_{amb}^4) \quad [\text{B.13}]$$

where ε is user defined and σ is constant.

For the purposes of this model $\dot{q}_{conduction}$ is not utilized and is a future consideration.

APPENDIX C: DISCRETIZATION ERROR CHECK

In order to maximize model accuracy while minimizing unnecessary computing time, a discretization error check is conducted to determine values for four input variables: the number of mesh spaces across a single electrochemical cell, the number of nodes in the X-direction, the number of nodes in the Y-direction (and therefore the number of total nodes across each current collector), and the number of time steps per second.

For the spiral and prismatic wound configurations, current is drawn at a rate of 5C for a duration of 20 seconds while the variable in question is varied for each iteration. Error is calculated using:

$$\% \text{ Error} = \frac{X_n - X_m}{X_m} * 100$$

Here, X_n represents an output value for a particular iteration and X_m represents that output's value for the most accurate iteration – aka the iteration with the largest number of nodes, spaces, or time steps. The particular outputs that are compared are the maximum nodal voltage, average nodal voltage and maximum nodal temperature at the end of each 20 second iteration.

An acceptable error limit of 0.2% is chosen since it provides results accurate to a millivolt, which is sufficient enough for a real-world application of batteries of these types.

The range of values used for number of nodes in the X-direction is 20, 40, 60, 80, 100, and 120 for the spirally wound configuration and 48, 64, 96, 112, and 144 for the prismatically wound configuration. The results can be found in Figure C.1 for each configuration. For the spirally wound case, 40 nodes provides sufficient accuracy, and the prismatically wound configuration requires 84 nodes.

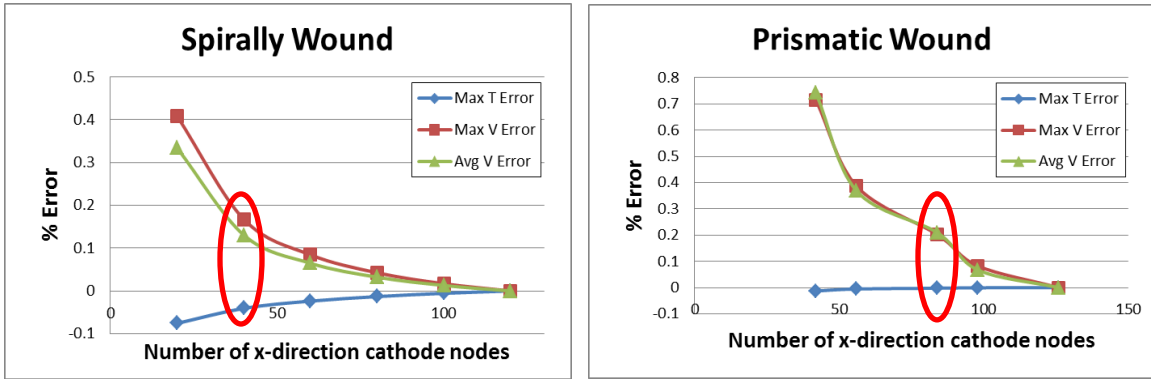


Figure C.1: Error percentage for number of nodes in x-direction for each configuration. Spirally wound configuration is on the left and prismatic wound on the right.

The range of values used for number of nodes in the Y-direction is 6, 8, 10, 12, and 15 for spirally wound and 8, 10, 12, 15 for prismatically wound. The results can be found in Figure C.2 for each configuration. For the spirally wound case, 12 nodes provides sufficient accuracy while 8 nodes are accurate for the prismatically wound configuration.

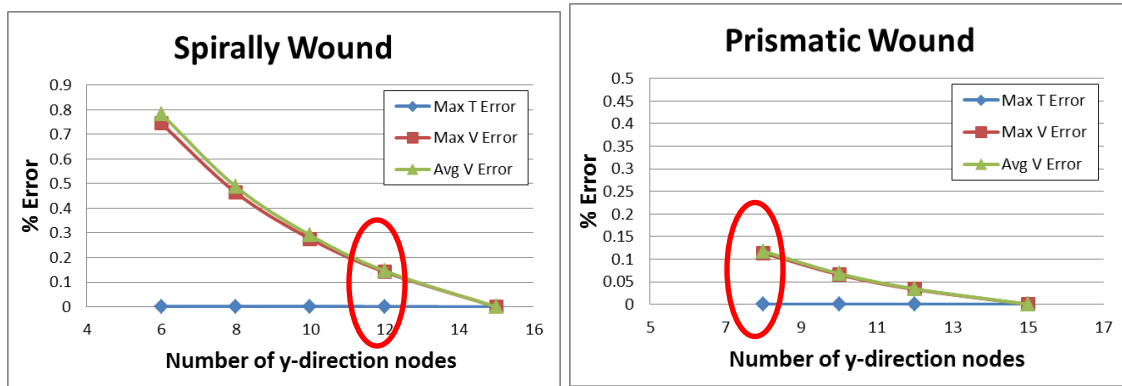


Figure C.2: Error percentage for number of nodes in y-direction for each configuration. Spirally wound configuration is on the left and prismatic wound on the right.

Since the number of nodes in the X and Y-directions are linked, a range of values is tested to ensure the best configuration: 40 X 10, 60 X 10, 60 X 12, and 80 X 12 for spirally wound and 56 X 10, 84 X 8 and 84 X 10 for prismatically wound. The results for each configuration can be found in Figure C.3. As expected, the 60 X 12 value is

provides sufficient accuracy for the spirally wound configuration and 84 X 8 for the prismatically wound configuration.

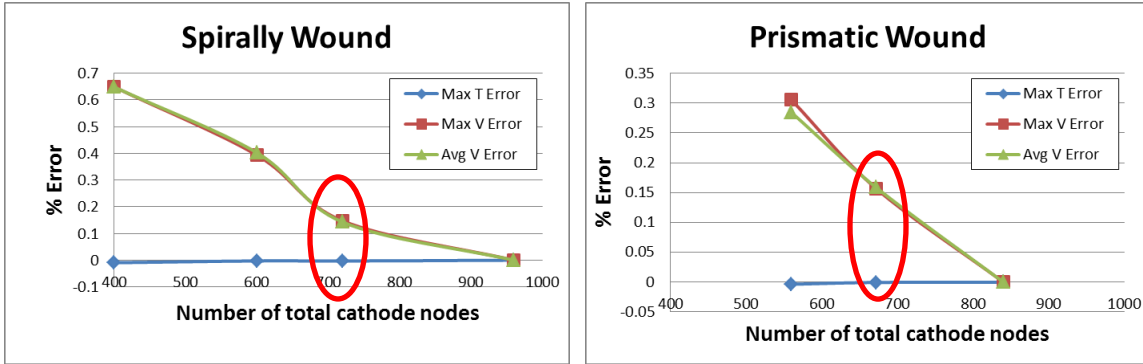


Figure C.3: Error percentage for number of nodes in both directions in the current collector for each configuration. Spiral wound configuration is on the left and prismatic wound on the right.

The range of values tested for number of time steps over a 20 second interval is 10, 20, 50, 100, and 200 for spirally wound and 10, 20, 50 and 100 for prismatically wound. The results can be found in Figure C.4 for both configurations. For both configurations, 20 time steps per 20 second interval provide more than sufficient accuracy, but they are chosen to avoid depletion of lithium at the surface of the electrode because of too large a time step. If fewer time steps are used, an error message that is built into the model will stop and exit the simulation.

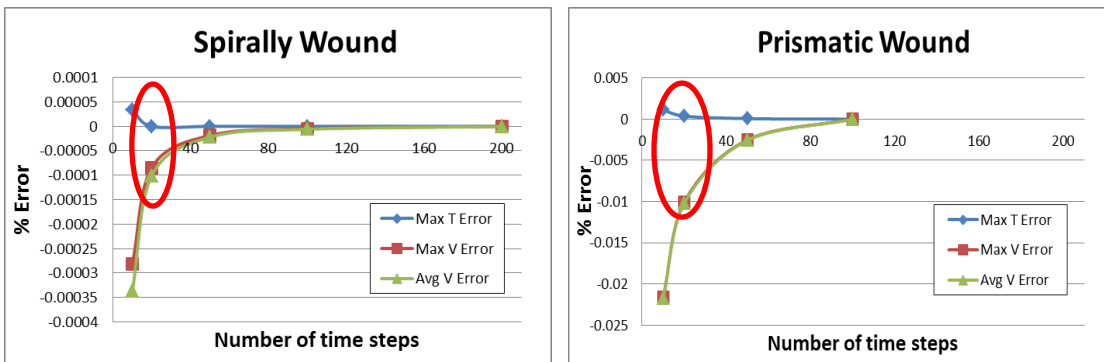


Figure C.4: Error percentage for number time steps over a 20 second interval for each configuration. Spiral wound configuration is on the left and prismatic wound on the right.

The range of values tested for number of mesh spaces in a single electrochemical cell is 10, 20, 30, 40 and 50 for spirally wound and 20, 30, 40, and 50 for prismatically wound. The results can be found in Figure C.5 for both configurations. For the spirally wound configuration, 10 mesh spaces is sufficient for accurate results, while 40 mesh spaces are needed for the spirally wound case.

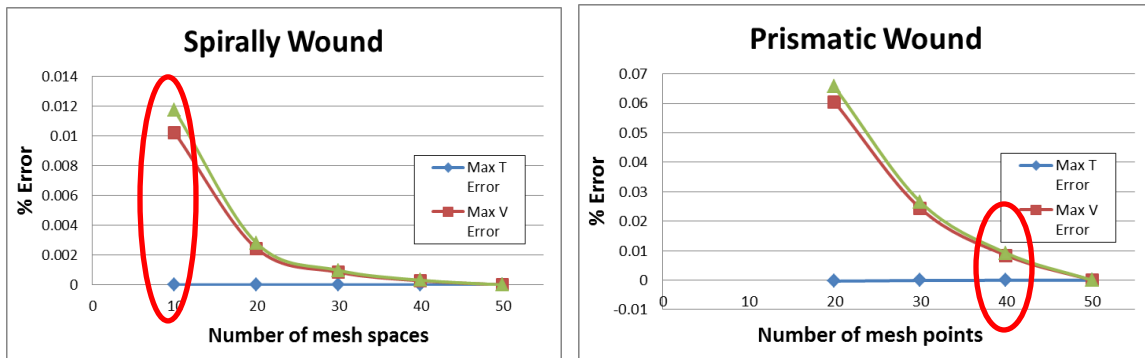


Figure C.5: Error percentage for number mesh spaces in a single electrochemical cell for each configuration. Spiral wound configuration is on the left and prismatic wound on the right.

References

- [1] X. Zhang, "Thermal Analysis of a Cylindrical Lithium-ion Battery," *Electrochimica Acta*, vol. 56, 2011, pp. 1246-1255.
- [2] M. Doyle, T.F. Fuller, J. Newman, "Modeling of Galvanostatic Charge and Discharge of the Lithium/Polymer/Insertion Cell," *Journal of The Electrochemical Society*, vol. 140, 1993, pp. 1526-1533.
- [3] T.F. Fuller, M. Doyle, J. Newman, "Simulation and Optimization of Dual Lithium Ion Insertion Cell," *Journal of The Electrochemical Society*, vol. 141, 1994, pp. 1-10.
- [4] M. Doyle, J. Newman, "Comparison of Modeling Predictions with Experimental Data from Plastic Lithium Ion Cells," *Journal of The Electrochemical Society*, vol. 143, 1996, pp. 1890-1903.
- [5] D.M. Bernardi, H. Gu, and A.Y. Schoene, "Two-Dimensional Mathematical Model of a Lead-Acid Cell," *Journal of The Electrochemical Society*, vol. 140, 1993, pp. 2250-2258.
- [6] T.I. Evans and R.E. White, "A Thermal Analysis of a Spirally Wound Battery Using a Simple Mathematical Model," *Journal of The Electrochemical Society*, vol. 136, 1989, pp. 2145-2152.
- [7] J. Lee, K.W. Choi, N.P. Yao, and C.C. Christianson, "Three-Dimensional Thermal Modeling of Electric Vehicle Batteries," *Journal of The Electrochemical Society*, vol. 133, Jul. 1986, pp. 1286-1291.
- [8] M.W. Verbrugge, "Three-dimensional temperature and current distribution in a battery module," *AIChE Journal*, vol. 41, 1995, pp. 1550-1562.
- [9] D.R. Baker and M.W. Verbrugge, "Temperature and Current Distribution in Thin-Film Batteries," *Journal of The Electrochemical Society*, vol. 146, Jul. 1999, pp. 2413-2424.
- [10] D. Bharathan, A. Pesaran, A. Vlahinos, and G. Kim, "Improving battery design with electro-thermal modeling," *Vehicle Power and Propulsion, 2005 IEEE Conference*, 2005, p. 8 pp.
- [11] Y. Inui, Y. Kobayashi, Y. Watanabe, Y. Watase, and Y. Kitamura, "Simulation of temperature distribution in cylindrical and prismatic lithium ion secondary batteries," *Energy Conversion and Management*, vol. 48, Jul. 2007, pp. 2103-2109.
- [12] J.N. Reimers, "Predicting current flow in spiral wound cell geometries," *Journal of Power Sources*, vol. 158, Jul. 2006, pp. 663-672.
- [13] J.N. Harb and R.M. LaFollette, "Mathematical Model of the Discharge Behavior of a Spirally Wound Lead-Acid Cell," *Journal of The Electrochemical Society*, vol. 146, Mar. 1999, pp. 809-818.
- [14] Harb, John N, "The Influence of Current Distribution on Battery Design and Performance," May. 2009.
- [15] Gi-Heon Kim, Smith, Kandler, and Ahmad, Pesaran, "Three-Dimensional Electrochemical Thermal Coupled Model of Large Format Cylindrical Lithium Ion Cells," Oct. 2007.

- [16] D.H. Jeon, S.M. Baek, "Thermal Modeling of Cylindrical Lithium Ion Battery During Discharge Cycle," *Energy Conservation and Management*, vol. 52, August 2011, pp. 2973-2981.
- [17] X. Zhang, "Thermal Analysis of a Cylindrical Lithium-ion Battery," *Electrochimica Acta*, vol. 56, Jan. 2011, pp. 1246-1255.
- [18] Y.S. Chen, C.C.Hu, Y.Y. Li, "The Importance of Heat Evolution During the Overcharge Process and the Protection Mechanism of Electrolyte Additives for Prismatic Lithium Ion Batteries," *Journal of Power Sources*, vol. 181, June 2008, pp. 69-73.
- [19] J.F. Cousseau, C. Siret, P. Biensan, M. Broussely, "Recent Developments in Li-ion Prismatic Cells," *Journal of Power Sources*, vol. 162, Nov. 2006, pp. 790-796.
- [20] K. Kumaresan, G. Sikha, and R.E. White, "Thermal Model for a Li-Ion Cell," *Journal of The Electrochemical Society*, vol. 155, Feb. 2008, pp. A164-A171.
- [21] C.R. Pals and J. Newman, "Thermal Modeling of the Lithium/Polymer Battery," *Journal of The Electrochemical Society*, vol. 142, Oct. 1995, pp. 3274-3281.
- [22] R. Gerver and J. Meyers, "Three-Dimensional Modeling of Electrochemical Performance and Heat Generation of Lithium-Ion Batteries in Tabbed Planar Configurations," Master's Thesis, The University of Texas at Austin, 2009.
- [23] H.S. Hsu, L.T. Yang, J. Ma, C. Zhu, *Ubiquitous Intelligence and Computing*, Springer, 2011.
- [24] Weisstein, Eric W. "Archimedes' Spiral." From MathWorld--A Wolfram Web Resource. <http://mathworld.wolfram.com/ArchimedesSpiral.html>
- [25] T.L. Heath, *The Works of Archimedes*, Dover Publications, 1897.
- [26] J. S. Newman and K.E. Thomas-Alyea, *Electrochemical Systems*, Wiley-IEEE, 2004.
- [27] C.M. Doyle, *Design and simulation of lithium rechargeable batteries*, 1995.
- [28] K. Thomas, J. Newman, and R. Darling, "Mathematical Modeling of Lithium Batteries," *Advances in Lithium-Ion Batteries*, 2002, pp. 345-392.
- [29] *Nanophosphate High Power Lithium Ion Cell*, 2011, A123 Systems, 15 June 2011.
- [30] V. Srinivasan and J. Newman, "Design and Optimization of a Natural Graphite/Iron Phosphate Lithium-Ion Cell," *Journal of The Electrochemical Society*, vol. 151, Oct. 2004, pp. A1530-A1538.
- [31] S.G. Stewart, V. Srinivasan, and J. Newman, "Modeling the Performance of Lithium-Ion Batteries and Capacitors during Hybrid-Electric-Vehicle Operation," *Journal of The Electrochemical Society*, vol. 155, 2008, pp. A664-A671.
- [32] V. Srinivasan and J. Newman, "Discharge Model for the Lithium Iron-Phosphate Electrode," *Journal of The Electrochemical Society*, vol. 151, Oct. 2004, pp. A1517-A1529.
- [33] J.S. Newman and K.E. Thomas-Alyea, *Electrochemical systems*, Wiley-IEEE, 2004.
- [34] S. Surampudi, E.S. Meeting, E.S.B. Division, and E.S.E.T. Division, *Lithium Batteries*, The Electrochemical Society, 2000.
- [35] U.S. Kasavajjula, C. Wang, and P.E. Arce, "Discharge Model for LiFePO₄ Accounting for the Solid Solution Range," *Journal of The Electrochemical Society*, vol. 155, Nov. 2008, pp. A866-A874.

- [36] M. Takahashi, S. Tobishima, K. Takei, and Y. Sakurai, "Reaction behavior of LiFePO₄ as a cathode material for rechargeable lithium batteries," *Solid State Ionics*, vol. 148, Jun. 2002, pp. 283-289.
- [37] L.O. Valoen and J.N. Reimers, "Transport Properties of LiPF₆-Based Li-Ion Battery Electrolytes," *Journal of The Electrochemical Society*, vol. 152, May. 2005, pp. A882-A891.
- [38] *CRC Handbook of Chemistry and Physics*, Cleveland, Ohio: CRC Press, 1977.
- [39] M.W. Verbrugge and B.J. Koch, "Electrochemical Analysis of Lithiated Graphite Anodes," *Journal of The Electrochemical Society*, vol. 150, Mar. 2003, pp. A374-A384.
- [40] A. Yamada, H. Koizumi, S. Nishimura, N. Sonoyama, R. Kanno, M. Yonemura, T. Nakamura, and Y. Kobayashi, "Room-temperature miscibility gap in Li_xFePO₄," *Nat Mater*, vol. 5, May. 2006, pp. 357-360.
- [41] M. Doyle and Y. Fuentes, "Computer Simulations of a Lithium-Ion Polymer Battery and Implications for Higher Capacity Next-Generation Battery Designs," *Journal of The Electrochemical Society*, vol. 150, Jun. 2003, pp. A706-A713.
- [42] S. Chen, C. Wan, and Y. Wang, "Thermal analysis of lithium-ion batteries," *Journal of Power Sources*, vol. 140, Jan. 2005, pp. 111-124.
- [43] V. Srinivasan and C.Y. Wang, "Analysis of Electrochemical and Thermal Behavior of Li-Ion Cells," *Journal of The Electrochemical Society*, vol. 150, Jan. 2003, pp. A98-A106.
- [44] J.L. Dodd, "Phase composition and dynamical studies of lithium iron phosphate," May. 2007.
- [45] K.J. Lee, G.H. Kim, K. Smith, "3D Thermal and Electrochemical Model for Spirally Wound Large Format Lithium-ion Batteries," Oct. 2010.

Vita

David Andrew Holmes McCleary was born in Hartford, CT. He spent his first 18 years living in Ellington, CT before going to college at Tufts University in Medford, MA. There, he earned a Bachelor of Science in Mechanical Engineering in May 2007. At Tufts he produced an undergraduate thesis on micro thermophotovoltaic cells. After college he worked for two and a half years at Nuvera Fuel Cells, a PEM fuel cell company in Billerica, MA. It was there that he developed his passion for electrochemistry while he prototyped a newly designed fuel cell. At the University of Texas at Austin he worked in the Meyers Research Group conducting computational modeling on lithium ion batteries. After graduation David will return to Nuvera Fuel cells where he will work with the fuel cell that was a prototype when he left and is now the only fuel cell technology used by the company.

Permanent address: 4 Field Drive
Ellington, CT 06029

This thesis was typed by the author.